

MULTI-LUMINOPHORE COATINGS FOR PRESSURE SENSITIVE PAINT  
APPLICATIONS

By

MUHAMMET ERKAN KOSE

A DISSERTATION PRESENTED TO THE GRADUATE SCHOOL  
OF THE UNIVERSITY OF FLORIDA IN PARTIAL FULFILLMENT  
OF THE REQUIREMENTS FOR THE DEGREE OF  
DOCTOR OF PHILOSOPHY

UNIVERSITY OF FLORIDA

2005

Copyright 2005

by

Muhammet Erkan Kose

For my lovely daughter Meryem Nur

## ACKNOWLEDGMENTS

I thank my advisor, Prof. Kirk S. Schanze, and my committee members, Dr. Bruce F. Carroll, Prof. Yngve Ohrn, Prof. Martin Vala, and Dr. Jeffrey Krause.

I thank all those that directly collaborated with me on my thesis projects. I thank all of the former and present group members of Schanze research team. They have been great friends and coworkers for the last 4 years. I thank my parents, my wife, and my daughter who brought joy and colors to my life.

## TABLE OF CONTENTS

	<u>page</u>
ACKNOWLEDGMENTS .....	iv
LIST OF TABLES .....	viii
LIST OF FIGURES .....	ix
ABSTRACT .....	xiii
CHAPTER	
1 INTRODUCTION .....	1
Background.....	1
Pressure Sensitive Paint.....	1
Problems of PSP .....	3
Temperature Effect.....	3
Image Registration and Reference Paint .....	3
Photodeterioration .....	4
Response Time and Induction Effect .....	4
Other Factors .....	5
History of PSP .....	5
Photophysics.....	6
Oxygen Quenching.....	9
Pressure and Temperature Dependence.....	10
PSP Equations .....	12
Physical Properties of PSP.....	14
Primer .....	14
Luminophores.....	16
Binder .....	19
Paint Preparation .....	24
Photostability.....	26
Temporal Stability .....	27
Typical Pressure Sensitive Paints .....	27
One-Component Pressure Sensitive Paints .....	27
Dual-Luminophore Pressure/Temperature Sensitive Paints.....	28
Self-Referencing and Binary PSPs.....	29
Three-Component PSPs.....	30
PSP Measurement Setup.....	31

Intensity-Based Imaging.....	31
Lifetime Imaging.....	33
Image and Data Analysis.....	35
Image Registration.....	35
Calibration-PSP Working Equations.....	36
In-situ Calibration.....	36
A-priori Calibration.....	37
k-Fit Method.....	38
Uncertainties of PSP.....	38
Calibration Error.....	38
Errors Due to the Measurement System.....	39
Errors due to Signal Analysis.....	40
Applications of PSP.....	40
Aerodynamic Models: Car Models, Delta Wing and Aircraft Models.....	40
Turbine Blades.....	42
Icing of Aircraft Parts.....	43
Detection of Sound Waves.....	43
Motivation and Summary of This Work.....	44
<b>2 PREPARATION AND SPECTROSCOPIC PROPERTIES OF MULTI-LUMINOPHORE PRESSURE SENSITIVE PAINTS.....</b>	<b>46</b>
Introduction.....	46
Photophysics of PtTFPP, Ruphen, and Rh110.....	49
Results and Discussion.....	51
Binder.....	51
Ruphen Incorporated Nanospheres.....	53
One-Component PSP: PtTFPP / Poly-t-BS-co-TFEM.....	56
Dual-Luminophore PSP: PtTFPP-Ruphen/PAN / Poly-t-BS-co-TFEM.....	60
Self-Referencing PSP: PtTFPP-Rh110/PAN / Poly-t-BS-co-TFEM.....	64
Three-Component PSP: PtTFPP-Ruphen/PAN-Rh110/PAN / Poly-t-BS-co-TFEM.....	68
Conclusions.....	73
Experimental.....	74
Chemicals.....	74
Synthesis of Poly-t-BS-co-TFEM.....	75
Synthesis of Dye Encapsulated Nanospheres.....	75
Preparation of Coatings.....	77
Spectroscopic Measurements and Imaging.....	78
<b>3 APPLICATIONS OF MULTI-LUMINOPHORE COATINGS TO THE IMAGING.....</b>	<b>80</b>
Introduction.....	80
Data Analysis Methods.....	82
Calibration Using Intensity-Ratios.....	82
Calibration Using Principal Component Analysis.....	83

Target Transformation.....	85
Factor Analyzability .....	86
Results and Discussion .....	89
Calibration Results for Dual-Luminophore PSP .....	89
PCA Calibration for Spectroscopic Data Set.....	89
PCA Results for CCD Camera Data Set.....	97
Intensity-Ratio Method Results for CCD Camera Data Set.....	104
Calibration Results for Three-Component PSP.....	106
Image Registration.....	106
PCA Calibration for Spectroscopic Data Set.....	112
PCA Calibration Results for CCD Camera Set Data.....	118
Intensity-Ratio Method Results for CCD Camera Set Data.....	119
Conclusions.....	120
Experimental.....	121
Preparation of Basecoat and PSP .....	121
Fluorimeter Measurements and CCD Imaging.....	122
 4 SUMMARY AND CONCLUSIONS .....	 125
Future Directions .....	128
PtTFPL / Poly-t-BS-co-TFEM .....	128
PtTFPP - DAP3 / Poly-t-BS-co-TFEM .....	131
PtTFPP-Pyrene / Poly-IBM-co-TFEM.....	133
Temperature Independent PSP .....	136
 APPENDIX	
A MATLAB MACROS.....	141
B APPLICATION OF PCA TO A SAMPLE DATA SET .....	155
LIST OF REFERENCES.....	161
BIOGRAPHICAL SKETCH .....	173

## LIST OF TABLES

<u>Table</u>	<u>page</u>
1-1: Photophysical properties of pressure sensitive luminophores. Shaded luminophores are also used for temperature sensing. ....	18
1-2: Photophysical properties of TSLs and of thermographic phosphors.....	19
2-1: The B values and temperature dependencies of homopolymers and copolymer. ....	53
3-1: Conditions and their corresponding C matrix elements. ....	91
3-2: Accuracies of average pressure estimates for intensity-ratio method and PCA method for dual-luminophore PSP imaging data. ....	101
3-3: Accuracies of average pressure estimates for intensity-ratio method and PCA method for three-component PSP imaging data.....	120

## LIST OF FIGURES

<u>Figure</u>	<u>page</u>
1-1: Intensity based PSP imaging setup.....	2
1-2: Jabłoński diagram. All transitions, which require either absorption or emission of a photon, are illustrated with solid lines. <sup>13</sup> .....	8
1-3: Anatomy of a PSP. ....	14
1-4: Ruthenium(II) $\alpha$ -diimine based probe molecules for oxygen sensing. ....	16
1-5: Structures of porphyrin based luminophores used in oxygen sensing. Note that Pt can be also replaced by Pd. ....	17
1-6: Repeat units of polymer binders used in PSP research. TFEM: 2,2,2-trifluoroethyl methacrylate; IBM: isobutylmethacrylate. ....	21
1-7: Measuring lifetime from two time-resolved images in pulse imaging method. <sup>3</sup> .....	34
1-8: Measurement scheme for phase-shift imaging method. ....	35
1-9: Imaging results .....	41
1-10: Surface pressure distribution. ....	42
1-11: PSP results on a fan blade. <sup>3</sup> .....	43
2-1: Chemical structure of Rhodamine 110. ....	51
2-2: Chemical structure of poly-t-BS-co-TFEM.....	52
2-3: Secondary electron microscopy images of Ruphen/PAN nanospheres in acetone solution for samples. ....	54
2-4: Images for Ruphen doped nanosphere emission.. ....	57
2-5: Variation of PtTFPP emission with pressure in poly-t-BS-co-TFEM binder at 312 K. The sample was excited at 465 nm.....	58
2-6: Stern-Volmer plot for PtTFPP in poly-t-BS-co-TFEM at 312 K. PtTFPP emission is integrated over an area of 635-670 nm.....	58

2-7: Variation of PtTFPP emission with temperature in poly-t-BS-co-TFEM binder at 14.77 psi. The sample was excited at 465 nm. ....	59
2-8: Temperature response of PtTFPP / poly-t-BS-co-TFEM coating at 14.77 psi.....	60
2-9: Pressure response of dual-luminophore PtTFPP-Ruphen/PAN in poly-t-BS-co-TFEM binder at 292.9 K. Excited at 465 nm. ....	61
2-10: Temperature response of dual-luminophore PtTFPP-Ruphen/PAN in poly-t-BS-co-TFEM binder at 14.68 psi. Excited at 465 nm. ....	61
2-11: Stern-Volmer plots for dual-luminophore PtTFPP-Ruphen/PAN nanospheres in poly-t-BS-co-TFEM coating at various temperatures.....	63
2-12: Temperature response of Ruphen/PAN and PtTFPP emissions at 14.68 psi. ....	64
2-13: Pressure response of Rh110/PAN and PtTFPP emissions at 315.8 K.....	65
2-14: SV plots for pressure response of Rh110/PAN and PtTFPP emissions at 315.8 K. ....	66
2-15: Pressure dependence of ratio $I(525\text{ nm}) / I(650\text{ nm})$ in PtTFPP-Rh110/PAN / poly-t-BS-co-TFEM coating at 315.8 K. ....	67
2-16: Temperature dependence of ratio $I(525\text{ nm}) / I(650\text{ nm})$ in PtTFPP-Rh110/PAN / poly-t-BS-co-TFEM coating at 14.7 psi.....	68
2-17: Elements of three-component PSP. ....	69
2-18: Pressure response of Rh110/PAN, Ruphen/PAN and PtTFPP emissions at 315.1 K. ....	70
2-19: Temperature response of PtTFPP-Ruphen/PAN-Rh110/PAN / poly-t-BS-co-TFEM coating at 14.81 psi.....	71
2-20: Pressure dependence of ratio $I(525\text{ nm}) / I(650\text{ nm})$ in PtTFPP-Ruphen/PAN-Rh110/PAN / poly-t-BS-co-TFEM coating at various temperatures. ....	71
2-21: Temperature dependence of ratio $I(525\text{ nm}) / I(570\text{ nm})$ in PtTFPP-Ruphen/PAN-Rh110/PAN / poly-t-BS-co-TFEM coating at various temperatures.....	72
2-22: Temperature variation of $I(570\text{ nm}) / I(525\text{ nm})$ and $I(650\text{ nm}) / I(525\text{ nm})$ at 14.81 psi. ....	73
2-23: Synthesis scheme of dye incorporated nanospheres.....	77
3-1: Emission intensity spectra of dual-luminophore PSP at various pressure-temperature combinations listed in Table 3-1. Excitation wavelength: 465 nm. ....	90
3-2: Fundamental spectra (row matrices, <b>R</b> ) for two largest eigenvalues. ....	93

3-3: Fundamental and reconstructed spectra.....	95
3-4: Comparison of intensity-ratios with their corresponding eigenvector elements.....	96
3-5: Experimental setup for CCD image data collection. Thermocouple locations are shown as 'X' marks.....	97
3-6: First and second rows: Images were obtained from ratio images of 550/40 nm and 650/10 nm filters at 6, 9, 12, and 14 psi, respectively.....	102
3-7: The predicted temperature gradient from top to the bottom of the coupon as indicated by lines for 6 different pressures. ....	104
3-8: Calibration surfaces.....	105
3-9: Ratio images.....	108
3-10: Comparison of noise levels of the images shown in Figure 3-9.....	110
3-11: Reference images.....	111
3-12: Emission intensity spectra of three-component PSP at various pressure-temperature combinations. Excitation wavelength: 470 nm. ....	113
3-13: Reconstructed spectra, D" for three-component PSP obtained with two largest factors.....	113
3-14: Reconstructed spectra, D" for three-component PSP obtained with three factors. ....	114
3-15: Fundamental spectra for abstract factors.....	115
3-16: Fundamental spectra of three factors after target transformation.....	116
3-17: Variation of eigenvector elements with pressure and temperature. ....	117
4-1: Pressure response of PtTFPL / poly-t-BS-co-TFEM coating at 294.5 K.....	129
4-2: Stern-Volmer plots obtained at various temperatures. PtTFPL emission is integrated over an area of 720 nm and 760 nm.....	130
4-3: Excimer emission and chemical structure of DAP3. Inset – The temperature response of DAP3 / poly-t-BS-co-TFEM coating at 14.7 psi.....	131
4-4: The pressure response of PtTFPP-DAP3 / poly-t-BS-co-TFEM coating at constant T.....	132
4-5: Stern-Volmer plots for PtTFPP and DAP3 emissions.....	133
4-6: Temperature response of PtTFPP-pyrene / poly-IBM-co-TFEM coating at 14.7 psi.....	134

4-7: Intensity variation plots of PtTFPP and pyrene emissions with temperature at 14.7 psi. ....	134
4-8: Pressure response of PtTFPP-pyrene / poly-IBM-co-TFEM coating at 291.9 K.....	135
4-9: Stern-Volmer plots for PtTFPP emission in PtTFPP-pyrene / poly-IBM-co-TFEM coating at various temperatures.....	136
4-10: Chemical structure of PTMSP.....	137
4-11: The temperature response of PtTFPP in PTMSP binder at 14.7 psi. ....	137
4-12: PtTFPP emission intensity variation with temperature at constant pressure for PtTFPP / PTMSP - poly-t-BS-co-TFEM coating.....	138
4-13: Stern-Volmer plot for PtTFPP emission for PtTFPP / PTMSP - poly-t-BS-co-TFEM coating at 307.2 K.....	139

Abstract of Dissertation Presented to the Graduate School  
of the University of Florida in Partial Fulfillment of the  
Requirements for the Degree of Doctor of Philosophy

MULTI-LUMINOPHORE COATINGS FOR PRESSURE SENSITIVE PAINT  
APPLICATIONS

By

Muhammet Erkan Kose

May 2005

Chair: Kirk S. Schanze  
Major Department: Chemistry

The conventional method for determining the surface air pressure distribution on an aerodynamic model relies on pressure taps installed at specific points on the model. However, this type of measurement gives data only at a limited number of discrete points, and also it is very difficult to install pressure taps at or near the edge of a model, and these regions are generally the areas of most interest. Luminescence imaging with pressure sensitive paint (PSP) is an optical technique that allows determination of full-field surface pressure distributions on wind tunnel models. Because of its inherent advantages, the PSP method has seen widespread use in wind tunnel testing. Nonetheless, PSP results are affected by the temperature fluctuations in the coating which leads to erroneous pressure predictions. Furthermore, the model movements in the wind tunnel studies require image registration of wind-on and wind-off images, which is difficult to achieve in some PSP experiments.

The research presented in this dissertation focuses on the development of multi-luminophore PSPs, which can solve temperature interference and image registration problems. The dual-luminophore and three-component coatings developed in our laboratory measure simultaneously both pressure and temperature distribution of the model surface. The temperature correction capability of both coatings is investigated. A novel data calibration method is developed based on principal component analysis (PCA) and the method has been employed for macroscopic dual-luminophore PSP data. The PCA technique led to higher accuracies in pressure estimations than the conventional intensity-ratio calibration method did. Eliminating the requirement for image registration is also discussed based on the data analysis results obtained from three-component PSP.

In summary, the PSP properties of the dual-luminophore and three-component paints proved that they can be successfully used in wind tunnel studies. It has also been discussed that the PCA calibration technique could be exploited for those coatings, in which the emissions of luminophores overlap which in turn decreases the sensitivity of pressure measurements for multi-luminophore PSPs. Apart from previous reports, this work shows the application of PCA to PSP imaging data for the first time.

## CHAPTER 1 INTRODUCTION

### **Background**

Surface pressure measurements are of great importance for basic fluid dynamics experiments, studying specific flow phenomena, and validating computational fluid dynamics codes.<sup>1-5</sup> The traditional method for measuring surface pressure distribution is loads analyses, which contains hundreds or thousands of pressure taps drilled into the aerodynamic surface and connected via tubing to multiplexed electronic pressure transducers.<sup>6</sup> The pressure taps data are used to map the lift needed to properly engineer support structure and other features of the model. However, loads analyses are both expensive and time consuming. Furthermore, measurements are made at discrete locations and it is generally impossible to install pressure taps at thin edges and sharp corners of the models where these areas are the areas of most interest. Until the 1980s, there was no alternative for loads method. Peterson and Fitzgerald proposed a new technique of surface flow visualization based on oxygen quenching of fluorescence.<sup>7</sup> This method is commonly referred to as the Pressure Sensitive Paint (PSP) technique and has increasingly become popular in the aerodynamic community.<sup>3</sup>

### **Pressure Sensitive Paint**

Pressure sensitive paint (PSP) technique is an optical method used for surface pattern flow visualization based on the principle of oxygen quenching of dye luminescence.<sup>3,6</sup> This technique utilizes a luminescent coating which is painted on a model surface (Figure 1-1). The coating consists of a long-lived luminophore and a

binder which is permeable to oxygen. The paint is excited with an appropriate excitation source and emission is imaged with digital cameras. The luminescence intensity emanating from the paint is inversely proportional to the oxygen concentration (hence surface pressure) over the coating. PSPs eliminate the constraints of pressure taps in many ways. First of all, PSPs provide surface pressure distribution with very high spatial resolution (constrained by lenses and CCD camera resolution). Second, one can observe flow features such as shock locations, boundary layer separation, and reattachment.<sup>3</sup> Third, the PSP technique is much less time demanding and is cost effective.<sup>3,8</sup>

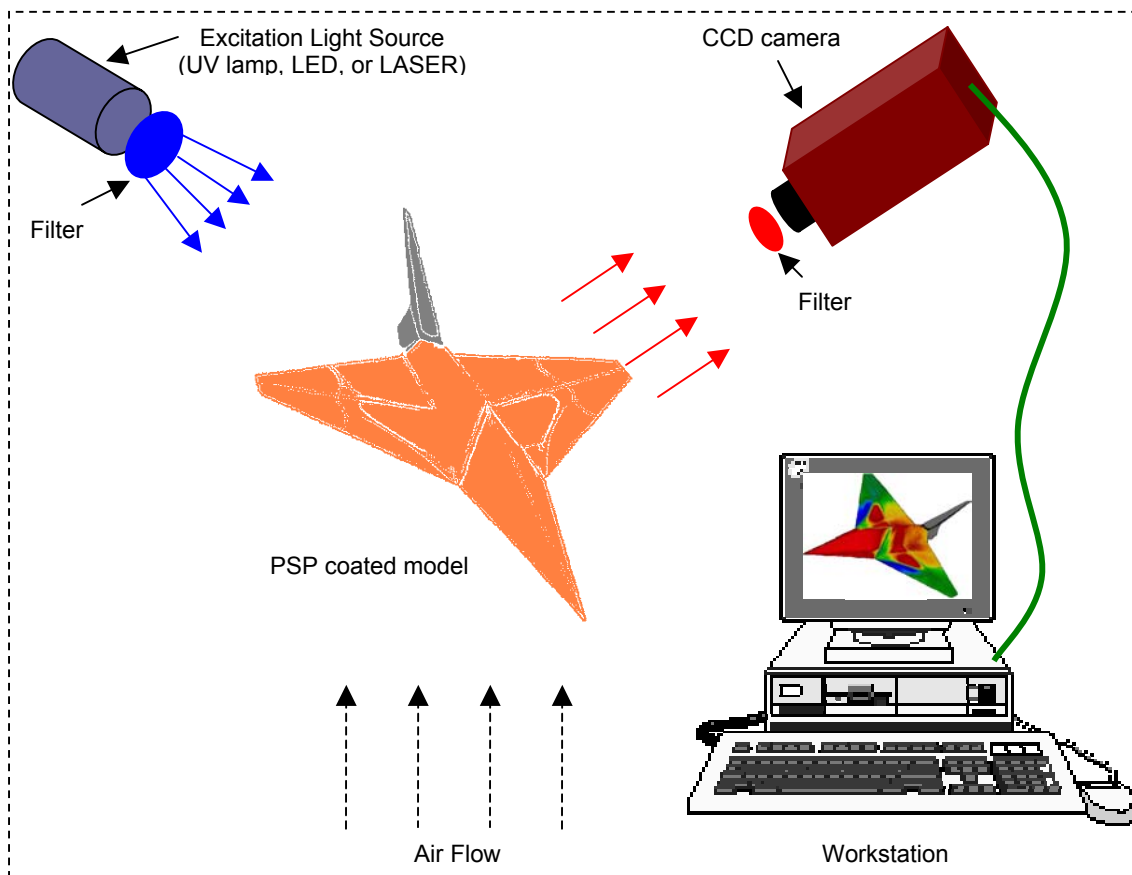


Figure 1-1: Intensity based PSP imaging setup.

## **Problems of PSP**

The most important aspect of the PSP technique is the enormous spatial resolution of measurements that can be obtained by affordable scientific grade CCDs. However, the PSP technique is not mature yet. There are several drawbacks of this technology which are listed below in the order of decreasing significance.

### **Temperature Effect**

The most serious problem encountered in PSP studies is the temperature dependence of PSP coating.<sup>9</sup> During wind tunnel measurements, the temperature over the model can drift from 10 °C to 50 °C, and if the response is not corrected, temperature variations can cause serious errors in pressure measurements. PtOEP (platinum(II) octaethylporphine) dye in Genesee-197 commercial silicone binder (one of the first PSPs used in wind tunnels) had a temperature coefficient of about 2.5%·°C<sup>-1</sup>. The temperature problem is less severe at very high pressures in comparison to low pressures, because large temperature fluctuations usually occur at high speed flows. Nonetheless, the temperature problem might also yield serious errors at low speed flows.<sup>10</sup>

The main reason for temperature dependency of PSP is the temperature dependence of oxygen diffusion through the polymer.<sup>11</sup> The diffusion of gases in polymers is an activated process and can be described by an activation energy and an attenuation coefficient in an Arrhenius equation. Temperature dependencies of radiationless decay rate and of triplet yield are other factors that contribute to the temperature sensitivity of PSP.<sup>11</sup> This topic will be discussed in detail later in this chapter.

### **Image Registration and Reference Paint**

In wind tunnel measurements, raw images are registered to a reference image with a known pressure distribution in order to eliminate the erroneous paint response due to

excitation field variation and paint thickness. The reference condition is usually taken when the wind tunnel is not running. However, there is, generally, significant model movement between wind-on and wind-off images.<sup>9</sup> One approach to eliminating this problem is to use reference points on the model with a use of computer algorithm. Nevertheless, initial observations indicated that wind-off and wind-on points on the model were not exactly the same points. And also, the excitation light intensities at wind-on and wind-off points were not the same.

Another method is applied by Gouterman to solve this problem.<sup>6</sup> He added inorganic phosphors to the PSP formulation, which are neither temperature nor pressure dependent. Then, he used the inorganic phosphor luminescence as a reference. Although temperature effect is the most serious problem for PSP applications, reference image registration also remains unsolved yet.<sup>3</sup>

### **Photodeterioration**

Singlet oxygen is produced when the excited luminophore is quenched by ground state oxygen. Singlet oxygen is a very reactive species. It can easily react with molecules around it, including the luminophore, forming new compounds. These new molecules might be non-luminescent and/or singlet oxygen based reactions might lead cross-linking in polymer matrix and hence cause intensity losses during measurements.<sup>9</sup> An hour illumination of PtOEP in Genesee-197 yielded 20-50% intensity losses. Since new polymers and luminophores are less prone to photodegradation, photodeterioration is no longer a big problem.

### **Response Time and Induction Effect**

The response time depends on the diffusion rate of oxygen in and out of the binder film. PtOEP in Genesee-197 required roughly 10 s for the luminescence intensity to

respond to pressure changes over the model surface. Fast response times (less than 1 s) are desired in wind tunnel studies.<sup>12</sup> Long response times might also cause induction effect, which is defined as an increase in the emitted intensity during the first few minutes of illumination. This is because of a photo-stationary state established in which oxygen is continually removed by a process, but is partly replaced by oxygen diffusing in from the air over surface.<sup>6</sup> Recently developed PSPs do not show induction effect due to fast response times of the paints.

### **Other Factors**

There are some engineering issues that also affect the accuracy of PSP measurements such as photodetector noise, model deformation, temporal variations in luminescence and illumination field, and spectral leakage.<sup>3</sup> They will be discussed later in this chapter.

### **History of PSP**

Peterson and Fitzgerald introduced the idea of oxygen quenching of fluorescent dyes for flow visualization in a wind tunnel.<sup>7</sup> They used Fluorescent Yellow dye adsorbed on silica particles. The coating displayed roughness and they also observed adherence problem for the coating. In the late 1980s, Gouterman and coworkers applied the idea of using oxygen quenching for pressure measurements on aerodynamic models and a qualitative experiment was performed at University of Washington. The first quantitative experiments on PSP were performed at the National Aeronautics and Space Administration (NASA) Ames Research Center.<sup>1</sup>

Initial studies on PSP started far earlier in former Soviet Union in the late 1970s at the Central Aero-Hydrodynamic Institute (TsAGI). Pervushin and Nevsky developed the first pressure sensitive coating in 1981. They conducted intensity and lifetime based

experiments and improved the PSP systems they were working on in the following years. Their research and efforts were published in 1990 which were aimed for commercialization as an ‘Optical Pressure and Temperature Measurement System’ through a distributor located in Italy.<sup>3</sup>

Research for PSP development and improvement spread among aerodynamic communities all over the world in the last 15 years. Among the major US institutions are NASA Ames, NASA Langley, NASA Glenn, Boeing, Arnold Engineering Development Center, and US Air Force Wright-Patterson Laboratory. Throughout the world, there are British Aerospace, British Defence Evaluation and Research Agency in United Kingdom; Deutsche Forschungsanstalt für Luft- und Raumfahrt in Germany; Office National d’Etudes et de Recherches Aérospatiales in France; National Aerospace Laboratory in Japan; and TsAGI in Russia. Also the University of Florida, Purdue University, and the University of Washington are main US universities that actively pursue PSP research.<sup>3</sup>

Research in all those centers and universities is not only concentrated on paint development, but also improving data acquisition, reduction procedure, illumination and imaging methods. Solving problems mentioned in the previous section associated with PSP technique is the major theme of current research in our group at the University of Florida.

### **Photophysics**

To understand how a PSP works, it is useful to discuss the processes that occur in a PSP binder when an excited luminophore returns to its ground state. First, a general overview of luminescence processes will be given for a typical luminophore, and then the photophysics of oxygen quenching will be discussed in PSP context.

Luminescence is a term used for both fluorescence and phosphorescence.<sup>13</sup> The physical processes in luminescence can be best described with the aid of a Jabłoński energy level diagram (Figure 1-2). This diagram shows the various excited states along with ground state of a luminophore ( $S_0$ ). The diagram is divided into two portions, singlet states and triplet states. The luminophore lies in its ground state from which it can be excited to higher singlet states.

The absorption and emission generally occur from a state of equilibrium to various vibrational levels of a new electronic state. Thus, luminescence will be shifted to longer wavelengths relative to absorption. This phenomenon is called the Stokes shift.<sup>13</sup> Each of the processes shown in the Jabłoński diagram has first-order kinetics, except  $k_q$  which follows a bimolecular mechanism. The rate constant for a single luminophore corresponds to a process's probability per unit time. Excitation occurs from the ground state instantaneously in  $10^{-15}$  s. Depending on the amount of excitation energy, the luminophore might be excited to  $S_1$  or  $S_2$  or to higher states. If a luminophore is excited to  $S_2$  state, it will rapidly undergo internal conversion ( $k_{IC} \sim 10^5$ - $10^9$   $s^{-1}$ ) to a vibrational level of  $S_1$ . Relaxation to the lowest vibrational level of  $S_1$  is also an extremely fast process ( $k_{nr}$ ). From  $S_1$  level it might either fluoresce ( $k_f \sim 10^6 - 10^9$   $s^{-1}$ ) or undergo internal conversion to  $S_0$ . Intersystem crossing to  $T_1$  is the third pathway ( $k_{ISC} \sim 10^1$ -  $10^9$   $s^{-1}$ ) that might occur from the  $S_1$  state. However, singlet to triplet transition is forbidden because of requirement of spin change according to quantum mechanics. Nonetheless, spin-orbit coupling makes such transitions possible. The probability of these transitions depends on the structure and atomic number of the atoms involved. Once the luminophore is in the  $T_1$  state, it might phosphoresce ( $k_p \sim 10^{-2} - 10^6$   $s^{-1}$ ) by a radiative

transition to  $S_0$  which is a forbidden transition and can be much longer than fluorescence. Non-radiative decay ( $k_{nr}$ ) is also another pathway for  $T_1$ - $S_0$  transitions. Since the triplet is always lower in energy than the singlet state, the phosphorescence emission wavelength is longer than that of fluorescence for a given luminophore. Note that intersystem crossing from the triplet to the singlet is still another possible pathway. Since phosphorescence takes place at relatively long times, the triplet excited state might return to  $S_0$  transferring its energy by collision with an oxygen molecule. This is known as phosphorescence quenching, and its rate is dependent on the concentration of oxygen ( $k_q[O_2] \sim 0 - 10^8 \text{ s}^{-1}$ ). The quenching of phosphorescence is a bimolecular reaction.<sup>6</sup>

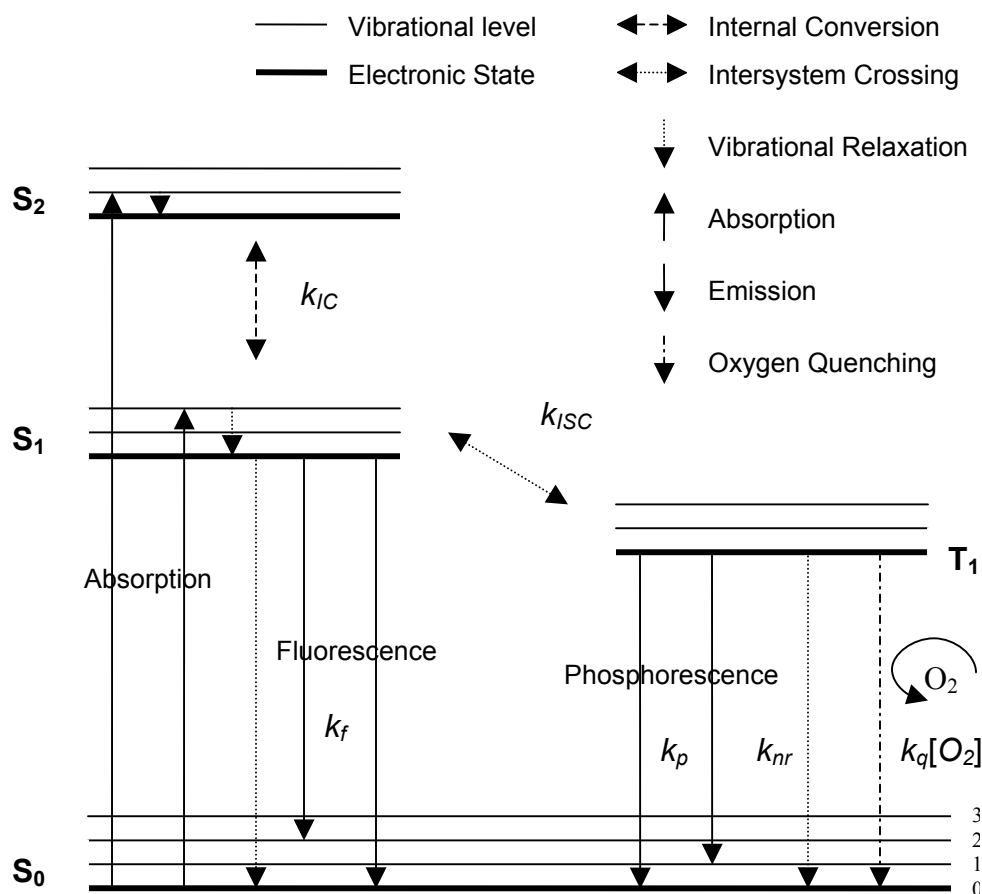


Figure 1-2: Jablonski diagram. All transitions, which require either absorption or emission of a photon, are illustrated with solid lines.<sup>13</sup>

## Oxygen Quenching

Oxygen molecule is triplet in its ground state. It has two singlet excited states where one of them is only 1.0 eV above the ground state.<sup>6</sup> This property of ground state oxygen makes it a very effective quencher. Collision of ground state oxygen with an excited luminophore leads to energy transfer to the ground state oxygen which usually promotes it to lowest energy singlet state. Then singlet oxygen can either luminesce at 1270 nm, or dissipate its energy by intersystem crossing to a vibrationally excited ground state, followed by vibrational relaxation.

After summarizing all the major steps involved in the photophysics of photoexcited state of a luminophore, we can build up our equations within the PSP perspective. Although oxygen quenching might also occur for the singlet excited state of a luminophore, usually the lifetime of fluorescence is too short to allow any significant quenching of singlet state. Hence, we concentrate on oxygen quenching of phosphorescence rather than fluorescence. Since there will not be any oxygen quenching at vacuum conditions, then we can write:<sup>14</sup>

$$\frac{1}{\tau_{vac}} = k_{nr} + k_p \quad (1-1)$$

In the presence of oxygen:

$$\frac{1}{\tau} = k_{nr} + k_p + k_q [O_2] \quad (1-2)$$

Divide equation (1-2) with equation (1-1), then we get:

$$\frac{\tau_{vac}}{\tau} = 1 + \frac{k_q}{k_{nr} + k_p} [O_2] = 1 + \tau_{vac} k_q [O_2] \quad (1-3)$$

Lifetime ratios are also proportional with both fluorescence intensity ratios and quantum yield ratios.

$$\frac{\tau_{vac}}{\tau} = \frac{\Phi_{vac}}{\Phi} = \frac{I_{vac}}{I} = 1 + K_{SV}[O_2] \quad (1-4)$$

Equation (1-4) is also known as Stern-Volmer equation, and  $K_{SV} = \tau_{vac}k_q$  is the Stern-Volmer constant.<sup>6</sup>

### Pressure and Temperature Dependence

The equilibrium concentration of oxygen in a polymer binder is proportional to the partial pressure of oxygen above the binder. This phenomenon is known as Henry's Law. By using Henry's Law, quenching rate with oxygen can be expressed as a function of pressure:

$$k_q[O_2] = k_q S \chi p \quad (1-5)$$

where S is solubility of oxygen in the binder,  $\chi$  is the mole fraction of oxygen in the gas (0.21 for air), and p is the gas pressure. If we rewrite the Stern-Volmer equation, we get:

$$\frac{I_{vac}}{I} = \frac{\tau_{vac}}{\tau} = 1 + k_q \tau_{vac} S \chi p \quad (1-6)$$

Thus, variation in pressure can be estimated from the equation above which also explains the basis of oxygen quenching for pressure measurements in PSP technology.<sup>6</sup>

Temperature sensitivity of PSP response is primarily because of two factors: temperature dependence of oxygen diffusion through the binder and temperature dependence of non-radiative decay.<sup>11</sup> From equation (1-4),  $K_{SV}(T) = k_q(T)/(k_p(T)+k_{nr}(T))$ , all these three terms in this equation are temperature dependent. Nevertheless, temperature dependence of  $k_p(T)$  is extremely weak and is due to the temperature dependence of the refractive index of the luminophore environment, and it can be

neglected. The decay rate  $k_{nr}(T)$  varies with temperature according to Arrhenius relationship:<sup>15</sup>

$$k_{nr}(T) = A_{nr} \exp\left(-\frac{\Delta E_{nr}}{RT}\right) \cong k_{nr}(T_{ref}) \left(1 + \frac{\Delta E_{nr}}{R} \frac{\Delta T}{T_{ref}}\right) \quad (1-7)$$

where  $\Delta E_{nr}$  is the activation energy associated with the process,  $A_{nr}$  is the attenuation coefficient,  $T_{ref}$  is an arbitrary reference temperature, and  $\Delta T$  is small relatively. The activation energy,  $\Delta E_{nr}$ , depends primarily on the luminophore and to a small extent on its environment.

In contrary to  $k_{nr}$ ,  $k_q$  depends mainly on the type of binder. The temperature dependence of  $k_q$  might be revealed by using Smoluchowski equation:<sup>14,16</sup>

$$k_q = 4\pi N\alpha r D \quad (1-8)$$

where  $D$  is the diffusion coefficient for oxygen,<sup>17,18</sup>  $r$  is the interaction radius between luminophore and oxygen (typically 1 nm, yet luminophore dependent),  $\alpha$  is the quenching probability after interaction ( $\sim 1$  for luminophores used in PSPs),  $N$  is Avogadro's number ( $6.023 \times 10^{23} \text{ mol}^{-1}$ ). Multiplying  $k_q$  with  $[O_2]$ , we get:

$$k_q[O_2] = k_q S \chi p = 4\pi N\alpha r D S \chi p = 4\pi N\alpha r P \chi p \quad (1-9)$$

where  $P = DS$  is permeability and varies with temperature again according to the Arrhenius relationship.<sup>19</sup> Therefore, the variation of  $k_q[O_2]$  with temperature can be described as in the following equation:<sup>11</sup>

$$k_q[O_2] = A_q \exp\left(-\frac{\Delta E_q}{RT}\right) \chi p \cong k_q(p_{ref}, T_{ref}) \left(1 + \frac{\Delta E_q}{R} \frac{\Delta T}{T_{ref}}\right) \frac{p}{p_{ref}} \quad (1-10)$$

where  $A_q$  incorporates the factor  $4\pi N\alpha r$ ,  $\Delta E_q$  is the activation energy for oxygen permeability through the binder, and  $p_{ref}$  is an arbitrary reference pressure.

In summary, temperature dependency of PSP response originates from  $k_{nr}$  and especially from  $k_q[O_2]$  terms which are used to define the Stern-Volmer constant. Although temperature variation in these terms can be modelled by Arrhenius type equations, PSP researchers tend to use polynomial equations to carry out calibration for data reduction due to ease in computations.

### PSP Equations

In the previous section, vacuum condition has been chosen as a reference condition in the equations. However, it is usually not possible (or impossible for wind tunnel experiments) to use vacuum as reference; as a result another condition (usually ambient) was chosen as reference. Then, Stern-Volmer equation takes the following form:

$$\frac{I_{ref}}{I} = \frac{\tau_{ref}}{\tau} = A + B \frac{p}{p_{ref}} \quad (1-11)$$

where  $A = (k_p + k_{nr}) / (k_p + k_{nr} + k_q[O_2]_{ref})$ ,  $B = k_q[O_2]_{ref} / (k_p + k_{nr} + k_q[O_2]_{ref})$ ,  $K_{SV} = B / (A[O_2]_{ref})$ , and  $A + B = 1$  for constant temperature measurements.<sup>1</sup> This relationship will be used throughout the text. It is important to note that this equation is valid for only limited pressure ranges. Most PSPs display a response to pressure that is nonlinear over large pressure ranges. This is generally due to microheterogeneity of the luminophore environment and/or due to nonlinear solubility of oxygen in the binder.<sup>20,21</sup> In most instances, using a two site model for heterogeneous response is adequate to describe the pressure response of coating.<sup>22</sup>

$$\frac{I_{vac}}{I} = \left( \frac{1}{\frac{f}{1 + K_{SV}^{(1)}[O_2]} + \frac{1-f}{1 + K_{SV}^{(2)}[O_2]}} \right) \quad (1-12)$$

In equation (1-12),  $f$  is the fractional contribution to the unquenched steady state emission, and  $K_{SV}^{(1)}$  and  $K_{SV}^{(2)}$  are effective quenching constants based on external oxygen concentrations.<sup>22,23</sup> Since there may even be more distributions for  $K_{SV}$ , as a consequence it appears unwise to place any physical significance on the value of  $K_{SV}^{(1)}$ ,  $K_{SV}^{(2)}$ , and  $f$ .<sup>24-26</sup> Ruyten showed that there is no fixed partitioning of luminophores in different molecular environments in polymer matrix (in Pt tetra(pentafluorophenyl) porphine / Fluoro-Isopropyl-Butyl polymer (PtTFPP/FIB) coating), because the  $f$  value changes with pressure.<sup>27</sup> Others obtained different results with different luminophore/polymer combinations.<sup>16,28</sup> Consequently, there is still a debate going on in this field.

Some scientists utilized a non-linear solubility model (equation (1-13)) for their PSP data, due to easier use of the equation in computations.<sup>29,30</sup> Nonlinear solubility is attributed to a Langmuir adsorption of oxygen in microvoids in addition to Henry's law of solubility. Equation (1-13) generally applies to glassy polymers where the microvoids are trapped by polymer rigidity.<sup>30</sup>

$$\frac{I_{vac}}{I} = 1 + A'[O_2] + \frac{B'[O_2]}{1 + b[O_2]} \quad (1-13)$$

By using Fick's law for diffusion along with equation (1-12) or equation (1-13), one can derive the mathematical expressions describing the time dependence of luminescence generated by in- and out-diffusion of oxygen in a polymer film doped with an oxygen sensitive dye. It is then possible to predict both diffusion coefficients and response times of polymer films used for optical oxygen sensing.<sup>18,31,32</sup>

## Physical Properties of PSP

Components of a typical pressure sensitive coating are displayed in Figure 1-3. Initially, a primer layer is applied on top of a pre-cleaned substrate surface. After curing of the primer, the active layer is applied. The details of each component used in the coating are given in sections below.

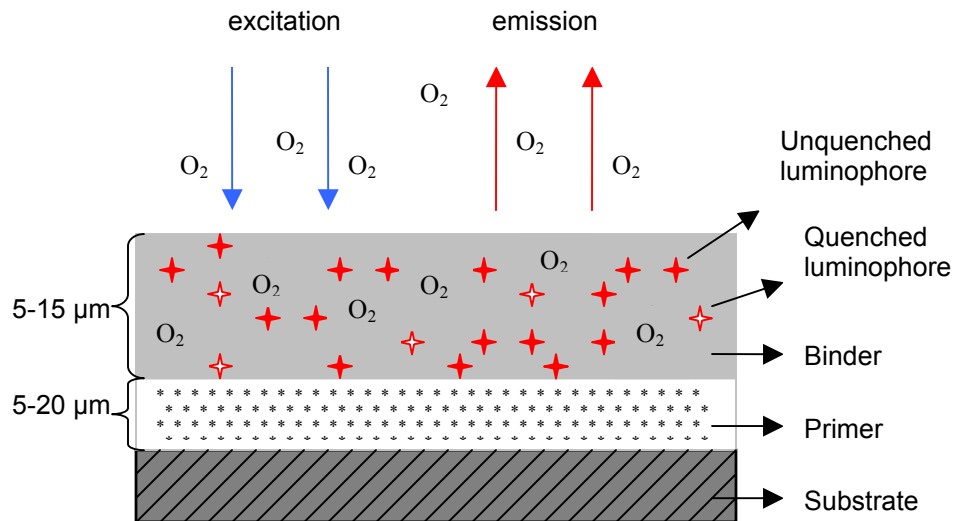


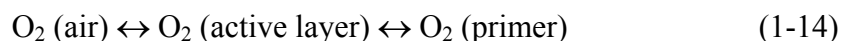
Figure 1-3: Anatomy of a PSP.

### Primer

An optically uniform model surface is crucial for accuracy of PSP imaging results. The intensity of emitted light in the direction of detecting hardware is related to the type of model substrate and its reflectivity. Materials such as Bondo (trademark for automotive, household, and marine paint products), wax, plaster, etc. were used in wind tunnels as a base coat initially, however different reflectivity of substrates induced substantial errors which led to the idea of using a uniform base coat to minimize the substrate related errors.<sup>19</sup> This has been achieved by utilizing inorganic pigments in binders used for PSP research. TiO<sub>2</sub> and Al<sub>2</sub>O<sub>3</sub> are such pigments in the form of very fine

white particles with high refractive index providing high reflectivity and high hiding power. They can be dispersed along with a polymer matrix on a substrate to give uniform highly reflective surfaces.<sup>19</sup>

Unfortunately, some primers used for PSP has been shown to modify the response time of the paint to a pressure change.<sup>12</sup> Furthermore, primers can also have significant effect on the temperature dependence of PSP.<sup>19</sup> This is because oxygen concentration in the sensing layer is in equilibrium with both the oxygen concentration in air and in base coat.



In order to have a minimum effect of base coat on PSP response, either there should be very little concentration of  $\text{O}_2$  in the primer layer (impermeable layer to oxygen such as polyacrylonitrile (PAN) layer) or the oxygen concentration in both sensing layer and primer layer should be approximately the same.<sup>19</sup> The best approach for determining the polymer matrix for base coat to be used in PSP would be then choosing a polymer which will also be used for active layer. However, since white pigments need to be added to the primer layer which is known to affect the oxygen diffusion through the polymer,<sup>33</sup> the response time and temperature dependence of PSP will still be affected. For instance, response times of a PtTFPP/FIB coating without and with base coat ( $\text{TiO}_2 + \text{FIB}$  polymer) are 0.6 s and 0.8 s, respectively. The temperature dependency of the same PSP changes from  $-0.53\%$  to  $-0.60\%$  without and with a base coat, respectively. It is also important to note that  $\text{TiO}_2$  is photoactive (it is a wide bandgap semiconductor) and can cause photooxidation of organic compounds when excited with wavelengths shorter than 390 nm.<sup>19</sup>

## Luminophores

The luminophores used in pressure sensitive coatings should possess high luminescence quantum yield, long emission lifetime, large Stokes shift, and excellent photostability.<sup>34</sup> It is also desired that their excitation and emission fall into visible region of the spectrum. Platinum porphyrins and ruthenium(II)  $\alpha$ -diimine complexes are very good candidates in this context. Structures of some of these complexes are shown in Figures 1-4 and 1-5. We will refer those luminophores as pressure sensitive luminophores (PSLs) throughout the text.

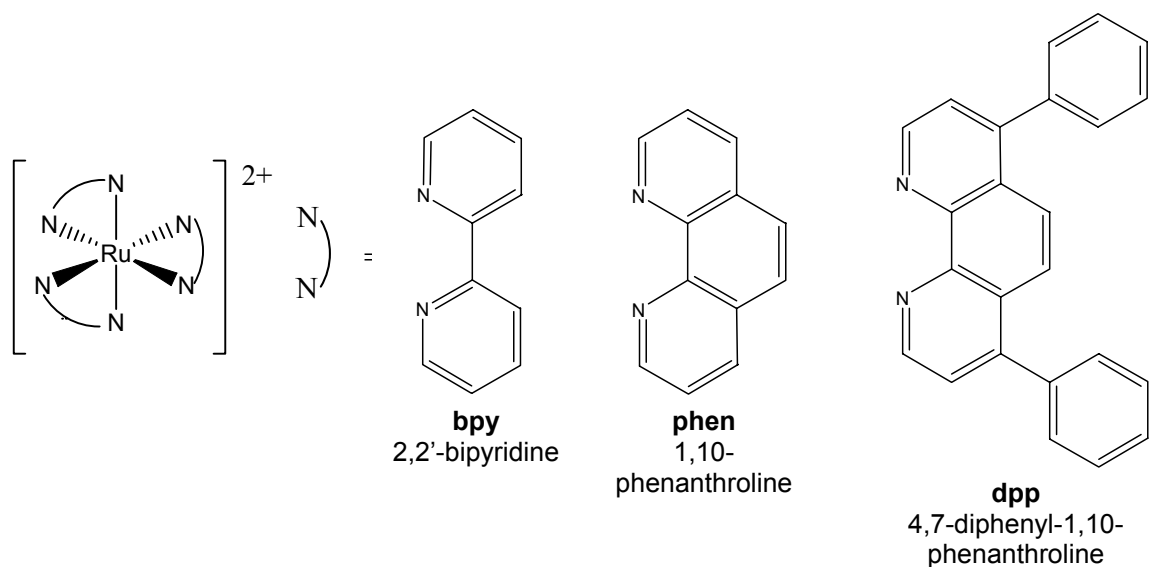


Figure 1-4: Ruthenium(II)  $\alpha$ -diimine based probe molecules for oxygen sensing.

Ruthenium complexes have proved to be very successful for oxygen quenching of luminescence (Figure 1-4). There are three types of excited states for them: metal centered d-d states, ligand-based  $\pi$ - $\pi^*$  states, and charge-transfer states. The complexes shown in Figure 1-4 display metal-to-ligand charge transfer (MLCT) transitions.<sup>35</sup> The major emission comes from the lowest triplet state, which can be quenched by oxygen.<sup>33</sup>

Strong spin-orbit coupling occurs in platinum and palladium porphyrins due to significant interaction between metal d-orbitals and antibonding  $\pi^*$  orbitals of porphyrin ring, which induces intersystem crossing to the triplet state ( $S_1 \rightarrow T_1$ ).<sup>36</sup> As a result of strong spin-orbit coupling, the quantum yield of singlet  $\rightarrow$  triplet intersystem crossing is close %100. Consequently, almost no fluorescence is observed for those complexes. High oxygen sensitivity of Pt(II) or Pd (II) metalated porphyrin macrocycles comes from long lifetimes of those complexes which are effectively quenched by oxygen.<sup>6</sup>

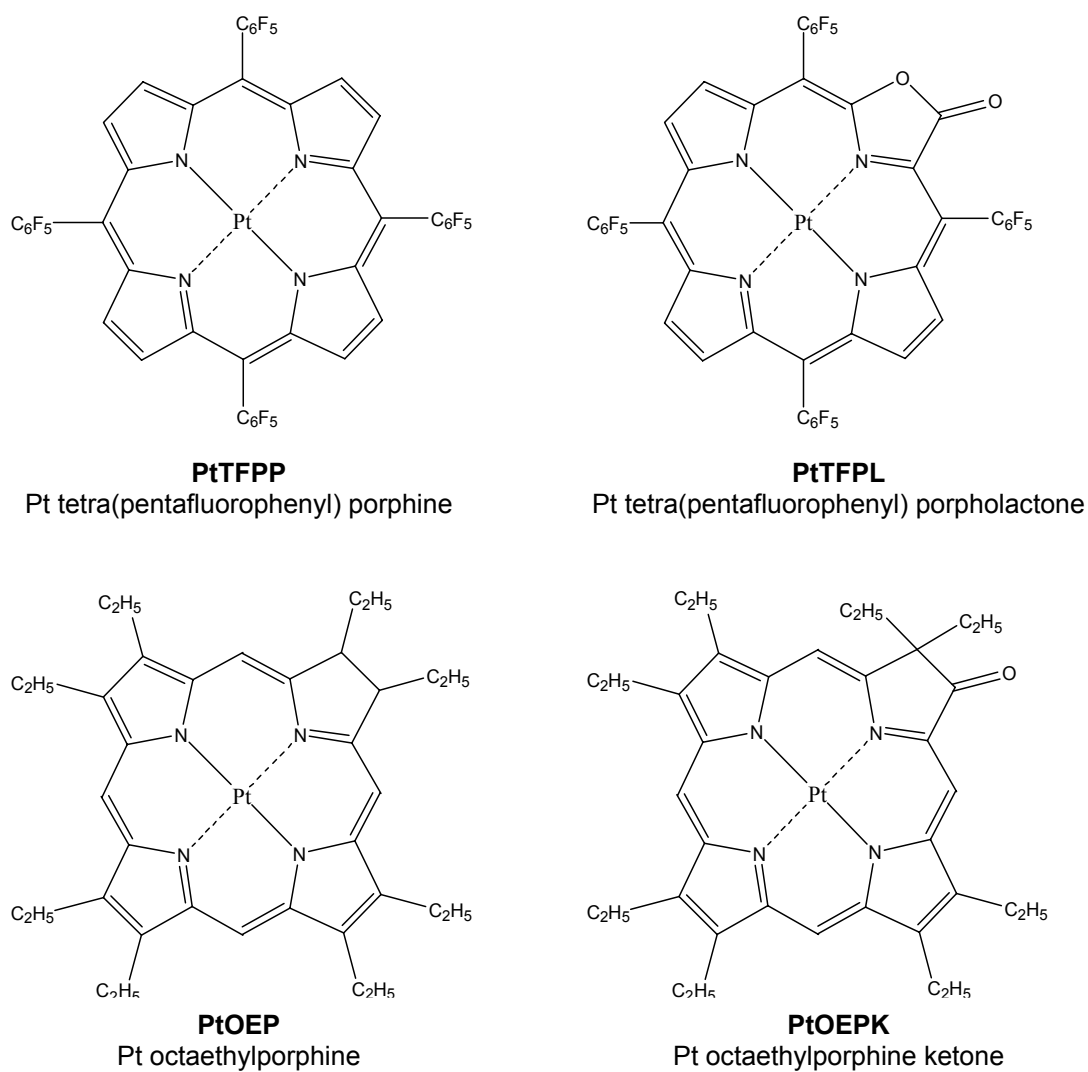


Figure 1-5: Structures of porphyrin based luminophores used in oxygen sensing. Note that Pt can be also replaced by Pd.

Table 1-1 gives a list of most widely used PSLs along with emission maxima, lifetimes, and quantum yields. It is important to note that lifetime values of different luminophores should not be compared to each other as they are sometimes sensitive to the medium where the measurements are taken. Rather, comparisons should be made in a general sense. There are a variety of pressure sensors in the visible region of spectra that are currently used in pressure sensitive coatings.<sup>37</sup>

Table 1-1: Photophysical properties of pressure sensitive luminophores. Shaded luminophores are also used for temperature sensing.

Luminophore	$\tau$ ( $\mu$ s) decay time	$\lambda_{\max}$ (nm) emission	Medium <sup>Ref</sup>	$\Phi$ (emission) quantum yield
PtTFPP	120	650	3-methylpentane <sup>38</sup>	0.90 <sup>a</sup>
PtTFPL	72	733	3-methylpentane <sup>38</sup>	0.58 <sup>a</sup>
PtOEP	91	644	Polystyrene <sup>39</sup>	0.50
PdOEP	990	670	Polystyrene <sup>39</sup>	0.20
PtOEPK	58	760	Polystyrene <sup>39</sup>	0.10
PdOEPK	460	790	Polystyrene <sup>39</sup>	0.01
Pyrene	0.45	393, 477	Cyclohexane <sup>40</sup>	0.60
Ru-pyrene	57	640	CH <sub>3</sub> CN <sup>41</sup>	0.10
Erythrosin B	~280	570, 691	Sol-gel <sup>42</sup>	0.02
Irppy	2	512	Toluene <sup>43</sup>	~0.50
Rubpy	0.60	613	Water <sup>44</sup>	0.04
Rudpp	5.34	613	Water/ethanol <sup>44</sup>	0.30
Ruphen	0.92	605	2-butanone <sup>44</sup>	0.08

<sup>a</sup> Phosphorescence quantum yield. PtTFPP quantum yield is 0.09 in CH<sub>2</sub>Cl<sub>2</sub>.<sup>45</sup>  
Ru-pyrene: covalently linked Rubpy and pyrene; Irppy: tris(2-phenylpyridine) iridium(III)

We described in previous sections the necessity of temperature correction to the pressure estimation. This is generally achieved by using a temperature sensitive luminophore (TSL) along with a pressure sensitive luminophore. If only TSL is immobilized in a support matrix, then such coatings are called temperature sensitive paints (TSPs).<sup>46</sup> TSPs are similar to PSPs in that, when illuminated with a proper light source, both show luminescence and both enable measurements by means of luminescent

intensity. The luminescence of TSLs is quenched through vibrational relaxation pathways that are temperature dependent. Especially ruthenium complexes<sup>47</sup> (Table 1-1, shaded luminophores) and Rhodamine B<sup>46</sup> show significant intensity variation upon temperature change. Inorganic phosphors have also been used for temperature measurements. These phosphors are also named as thermographic phosphors.<sup>48</sup> Table 1-2 gives well-known TSLs and thermographic phosphors which are used in both PSP and TSP research.

Table 1-2: Photophysical properties of TSLs and of thermographic phosphors.

Sensor	$\tau$ ( $\mu$ s) decay time	$\lambda_{\max}$ (nm) emission	Medium <sup>Ref</sup>	$\Phi$ (emission) quantum yield
La <sub>2</sub> O <sub>2</sub> S:Eu <sup>3+</sup>	~10	514	FIB <sup>49</sup>	-
MFG	~3000	655	Sol-gel <sup>50</sup>	-
Rhodamine B	0.004	580	Ethanol <sup>51</sup>	0.65
Perylene	0.005	452, 476 <sup>52</sup>	Cyclohexane <sup>53</sup>	0.94
Eu(TTA) <sub>3</sub> Phen	335	613	pDDA <sup>54</sup>	-
EuD2	~ 185	615	NA <sup>38</sup>	-
DOCI	0.0003	503	Ethanol <sup>55</sup>	0.12
MgTFPP	0.008	596, 650	FIB <sup>56</sup>	0.08

MFG: 3.5MgO-0.5MgF<sub>2</sub>-GeO<sub>2</sub>:Mn; Eu(TTA)<sub>3</sub>Phen: tris(4,4,4-trifluoro-1-(2-thienyl)-1,3-butanediono)-1,10-phenanthroline europium(III); EuD2: 1,10-phenanthroline-tris(3-(3-phenanthryl)-1-(9-phenanthryl)propane-1,3-dione europium; DOCI: 3,3'-diethyloxacarbocyanine iodide; MgTFPP: Mg tetra(pentafluorophenyl) porphine; pDDA: poly-(N-dodecylacrylamide); NA: Not Available.

The typical concentrations of PSLs and/or TSLs in binders are in the range 10<sup>-3</sup> - 10<sup>-2</sup> M. Using high concentrations of luminophores result in self-quenching of luminescence.<sup>57</sup> Self-quenching is generally observed for luminophore concentrations larger than 10<sup>-3</sup> M, where the average distance between molecules is ~10 nm at this concentration.<sup>3</sup>

### Binder

Binders with high permeability to oxygen are used in PSP technology. Both sol-gel based coatings and polymers have been utilized for this purpose. Silicone is one the most

widely used matrix in PSP research due to its high oxygen permeability. Initial PSPs also employed commonly known polymers such as polystyrene, polymethylmethacrylate, and cellulose acetate.<sup>58</sup> These polymers exhibit less oxygen permeability than silicone; however addition of plasticizer and/or additives<sup>14</sup> can increase the oxygen permeability of parent polymer and even improve the mechanical properties of the coating.

As PSP technology has matured, new polymers have been synthesized for specific applications. The Gouterman group developed (fluoro/isopropyl/butyl)acrylic (FIB) polymer.<sup>12</sup> This coating displayed high sensitivity to oxygen concentration with a low temperature dependence because of low activation energy of FIB's oxygen diffusion. PtTFPP/FIB coating showed a pressure-independent temperature dependence.<sup>12</sup> Such coatings were named 'ideal' PSPs, because they ease the data reduction for wind tunnel experiments.

Fluorinated methacrylate polymers give much greater quenching response than their nonfluorinated analogues when doped with Rudpp.<sup>59</sup> This is because fluorine derivatives are known to have excellent oxygen transport properties. Furthermore, since electron-withdrawing character of fluorine is large, fluoropolymers are stable toward photooxidation.<sup>60</sup> However, fluorinated polymers have poor solubility and optical clarity, and the monomer units are more expensive than non-fluorinated analogues.<sup>59</sup>

Amao et al. synthesized several copolymers (poly(styrene-co-TFEM), poly(IBM-co-TFEM), poly(styrene-co-pentafluorostyrene)) which might be used in PSP research.<sup>61-</sup>  
<sup>63</sup> Pol[*(n*-butylamino)thionyl]phosphazene] (C<sub>4</sub>PATP) is a low-T<sub>g</sub> polymer which displays similar oxygen quenching properties to PDMS.<sup>16</sup> DiMarco and Lanza pointed out that by changing the viscosity of the medium for luminescent oxygen sensors makes

it possible to improve the performance of oxygen sensor.<sup>64</sup> Structures of common polymer binders used in PSPs are illustrated in Figure 1-6.

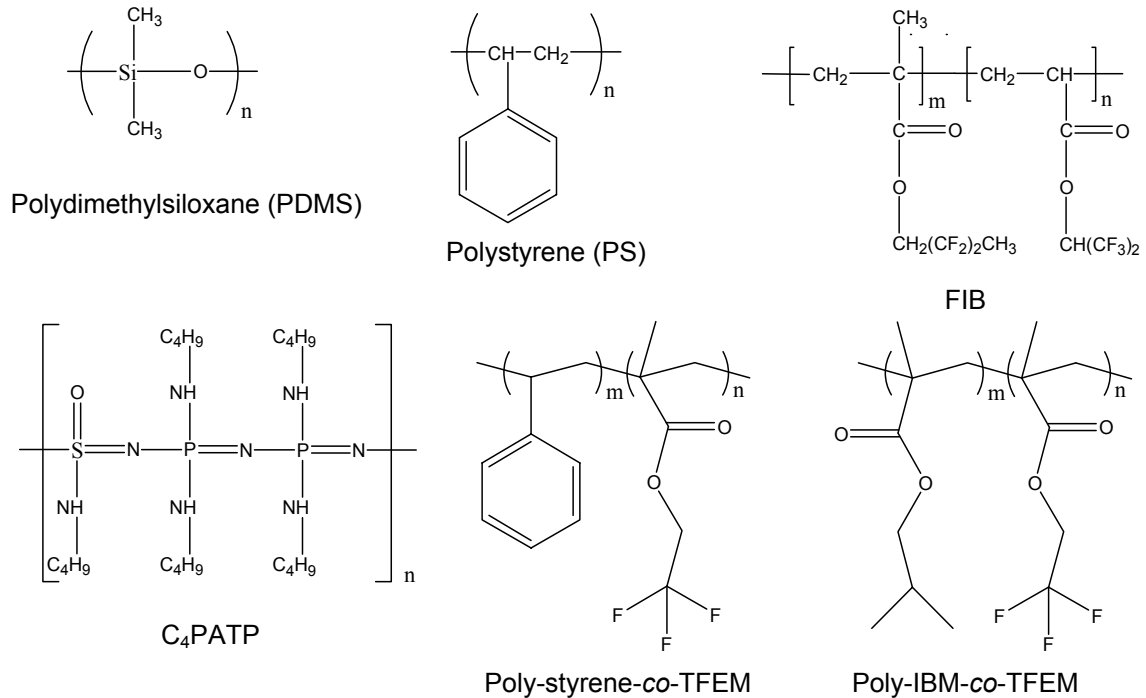


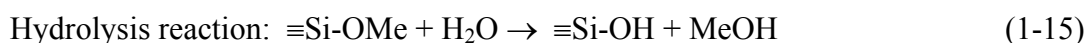
Figure 1-6: Repeat units of polymer binders used in PSP research. TFEM: 2,2,2-trifluoroethyl methacrylate; IBM: isobutylmethacrylate.

We can make a rough comparison of pressure sensitivity of these polymer binders when PtTFPP is dispersed in them; C<sub>4</sub>PATP (0.96),<sup>16</sup> PDMS (0.94),<sup>34</sup> FIB (~0.90),<sup>12</sup> poly-IBM-co-TEM (~0.75), poly-sytrene-co-TFEM (~0.65), and PS (~0.44).<sup>23</sup> The numbers given in the parentheses are B values from equation (1-11). Note that the pressure responses of some of these polymers exhibit significant non-linearity which makes the comparison of B values cumbersome. Moreover, dispersion of different dyes in those matrices might yield different B values and ordering might also change.

Copolymers have received significant attention for possible candidates for PSP binders. This is because it is possible to tailor the properties of sensor support by

choosing proper monomer units.<sup>21</sup> Proper comonomer units can be used to increase the solubility of polar molecules in nonpolar polymers and even they might be used for increasing polymer rigidity without affecting much the sensor properties of the matrix.<sup>26,59</sup> Ruffolo and his colleagues showed that block copolymers poly(aminothionylphosphazene)-*b*-poly(tetrahydrofuran) with Rudpp have excellent properties for air pressure applications. Block copolymers exhibited linear Stern-Volmer plots, good quenching sensitivity, and better mechanical properties than homopolymers. They also compared oxygen sensing properties of block copolymers with the same composition polymer blends, and found that the former displays much better sensitivity to oxygen concentration.<sup>65</sup> Morin et al. reported new copolymers consisting of GP-163 (a PDMS with varying amounts of pendant acrylate groups) combined with number of alkyl methacrylates with long chain alkyl or fluorinated esters. They observed that increasing the chain length or the degree of fluorination on the hydrocarbon chains enhances performance of the sensor matrix.<sup>59</sup>

Apart from polymer binders, sol-gel based matrices have also been used in pressure sensitive coatings. A brief preparation of sample sol-gel coating is as follows: tetramethoxysilane, methanol, deionized water, and NaOH are mixed together at room temperature. The luminophore is added to the resulting mixture which is called 'sol'. The sol is cast on a surface and allowed to gel. The sol-gel coating is then dried and aged at room temperature. The following reactions occur during these processes.<sup>66</sup>



The siloxane bonds (Si-O-Si) form the gel network which is highly porous in structure and allows the diffusion of gases.<sup>50,67</sup> One can tune the pressure sensitivity of a sol-gel matrix by exploiting different synthetic procedures based on the reactions above.<sup>68</sup> Especially, ruthenium complexes have frequently been used in such matrices.<sup>69</sup> Sol-gel coatings can be heavily doped with luminophore to produce a bright signal. They also exhibit excellent sensitivity and reversibility.<sup>33</sup>

Addition of pigments or additives usually improves the luminescence behavior of pressure sensitive paint.<sup>21,34</sup> Gouin et al. showed that dispersing  $A_2O_3$  in a low cost commercial silicone binder increased the sensitivity of oxygen response, and lowered the activation energy for oxygen permeation. Moreover, they were able to idealize the silicone based PSP by varying the pigment concentration.<sup>14</sup> Ertekin et al. used oxygen carrier perfluorochemicals in a silicone matrix to improve the oxygen sensitivity of a novel ruthenium complex.<sup>70</sup> Winnik's group added silica to  $C_4PATP$  and PDMS polymer films to examine the influence of silica nanospheres on oxygen diffusion in these low- $T_g$  polymers. Addition of silica did slightly decrease the diffusion coefficients in polymer matrices. They showed that PtOEP adsorbs to the silica particles in PDMS, but it remains in the polymer matrix in  $C_4PATP$ .<sup>71</sup> Silica particles act not only as a reservoir for oxygen, but also improve the mechanical properties of the matrix.<sup>18</sup> In another work, addition of silica to silicone based polymers where Rudpp is immobilized in the polymer matrix has significantly improved oxygen sensitivity of sensor film and increased the linearity of Stern-Volmer plot.<sup>21,57</sup> Kneas et al. demonstrated that oxygen quenching in polymers can be a complex combination of sample preparation and the effects of additives. Additives

and/or fillers can affect quenching in non-obvious ways.<sup>18,39,72</sup> The factors that control the sensitivity of optical oxygen sensors are nicely discussed in a paper published by Mills.<sup>25</sup>

Crutchley and co-workers recently reported the synthesis of new binders to which they attached the luminophores by chemical bonds.<sup>73,74</sup> This procedure yielded a good dispersion of dye in the matrix; furthermore dye attachment significantly reduced spatial noise for luminescence images.<sup>75</sup>

For some PSP applications, very fast response times are required (less than 1 ms); such as measuring unsteady flow-fields in rotating machinery, flutter test, and short-duration wind tunnels.<sup>76,77</sup> Response time of a conventional PSP is proportional to  $l^2/D$ , where  $l$  is the thickness of supporting matrix and  $D$  is the mass diffusivity of oxygen in that matrix. One can either decrease the thickness of matrix or use a porous material to obtain very fast response times.<sup>78</sup> Since the response times of conventional PSPs (from milliseconds to a few seconds) are too long for these experiments, alternate binders have been used such as anodized aluminum, thin-layer chromatography, and polymer/ceramic particles coated with a polymer.<sup>2,79,80</sup> Sakaue et al. reported response times less than 100  $\mu$ s by using those matrices with Rudpp.<sup>78,81,82</sup> Pyrene butyric acid and pyrene sulfonic acid were adsorbed on porous anodized aluminum surface for unsteady pressure measurements.<sup>79</sup>

### **Paint Preparation**

The general method for PSP preparation is that PSP components (binder, dye(s), etc.) are dispersed in a volatile solvent (or a mixture of solvents) and then the solution is sprayed on the substrate. It is important to choose the best solvent for paint formulation. Because poorer solvents might increase the diffusion coefficients due to production of

films with greater void volume and less organization of polymer chains. Despite the increase in diffusion coefficients, oxygen sensitivity is usually poorer in such sensor films.<sup>18</sup> The paint is dried either at atmospheric pressure or by heating the paint for some time. If there are particles that will not dissolve in paint solvent, then it is often necessary to decrease the size of particles as much as possible in order to obtain a homogenous film and a uniform PSP response. TiO<sub>2</sub> particles and inorganic phosphors are usually ballmilled prior to use in PSP formulations.<sup>49</sup>

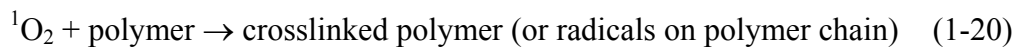
The substrate surface is cleaned before applying primer solution. After drying primer layer, PSP solution is sprayed on top of the primer layer. Some research groups also used a TSP layer under the active layer in order to measure the temperature variation of surface concurrently with pressure variation. However, it is desired to be able to immobilize both pressure and temperature sensors in the same layer.

It has been shown that annealing of the PSP at high temperature (above the polymer's glass transition temperature,  $T_g$ ) has significant effects on PSP properties.<sup>15</sup> Annealing has two possible effects on the paint layer: thermal effect and drying effect. Thermal effect is more important due to the fact that it increases ideality of PSP by relaxing and loosening the entanglements in the polymer network, yielding to a thermodynamically stable system. The relaxation of polymer network facilitates easier oxygen diffusion and leads to lower activation energy for penetrants.<sup>15</sup> PtTFPP/FIB coating is, generally, annealed at 100 °C for at least half an hour for this purpose.<sup>12</sup>

Pressure sensitive coatings should display desirable mechanical properties such as ease of application and removal, curing time, adhesion to the test surface, hardness and damage resistance, thickness, and surface finish.

## Photostability

Photostability of the paint is one of the main concerns in PSP research. As mentioned above, early paints like PtOEP/Genesee-197 lost 20-50% of their wind-off intensity in an hour of illumination.<sup>1</sup> Since paints are exposed to strong excitation intensities for many hours in wind tunnel experiments, it is important that little photodegradation of the dye and binder occurs throughout experiments for the accuracy of results. In general, 1-2% photobleaching of luminescence intensity per hour is acceptable for wind tunnel research. PtTFPP has proven to be very stable luminophore against illumination. That is why it is widely used in current PSPs.<sup>6</sup> Photobleaching occurs because of several reasons. Singlet oxygen is generated in the quenching process with ground state triplet oxygen. Singlet oxygen is very reactive, and is believed to be the source of most photobleaching reactions that occur in the polymer matrix.<sup>6</sup>



Here,  $L_a$  and  $L_b$  are non-emissive species. There are also some other pathways for the depletion of luminophore concentration in the polymer matrix such as:



$L_c$  is produced from photoexcited luminophore and does not emit light.<sup>6</sup> Careful choice of binder and luminophore combinations for PSP studies might minimize the photobleaching problem observed in wind tunnel experiments. Indeed, current PSPs suffer much less from intensity losses than at the beginning of this technology.

## **Temporal Stability**

Temporal stability is also very important for pressure sensitive coatings. Pyrene molecule is very stable in photochemical sense, however it sublimates especially at high temperatures, which limits its usage.<sup>83,84</sup> To overcome the sublimation problem in pyrene-based PSPs, several pyrene derivatives were tested to find out whether they could be employed as a substitute for pyrene in pressure sensitive paints.<sup>85,86</sup> Sol-gel based coatings might exhibit dye leaching from glass matrix.<sup>42</sup> Poly(1-trimethylsilyl-1-propyne) (PTMSP) based sensors suffered from aging of polymer matrix.<sup>87</sup> Temporal stability of new PSPs should be checked in the development stages of the coatings.

## **Typical Pressure Sensitive Paints**

PSPs can be categorized in four groups depending on the number and functions of luminophores used in paint formulation. In reality, 'pressure sensitive paint' phrase is used for all coatings that can measure air pressure. However, it is better to classify PSPs under several names to indicate the capability of the paint.

### **One-Component Pressure Sensitive Paints**

PtOEP/GP-197 is the first PSP developed at the University of Washington. The paint was excited by a UV light source and luminescence was collected at 650 nm. However, the paint suffered from rapid photobleaching ( $15\% \cdot \text{hr}^{-1}$ ), high temperature sensitivity ( $-2\% \cdot ^\circ\text{C}^{-1}$ ), and slow temporal response.<sup>1</sup> Russian scientists used especially pyrene in their PSP as a pressure sensitive dye. Although pyrene is a very photostable molecule, it tends to sublime rapidly which to some extent limits its application in wind tunnels. Recently developed one-component PSPs have improved in many ways. Puklin et al. reported a new PSP in which PtTFPP is dispersed in FIB.<sup>12</sup> This coating displayed very low photodegradation ( $1.5\% \cdot \text{hr}^{-1}$ ) and fast response time. The biggest improvement

is the low temperature sensitivity of the coating which is only  $-0.6\%-\text{°C}^{-1}$ . One-component PSPs do not provide any information for temperature variation in the coating, therefore their usage is limited for applications where little or no temperature gradients occur during the experiments.

### **Dual-Luminophore Pressure/Temperature Sensitive Paints**

Initial pressure sensitive paints used only one luminophore in the active layer to measure pressure distribution. However, it was later discovered that the luminescence of PSL is also temperature dependent, which necessitated the information about the temperature distribution of the paint surface. Since the temperature on the model surface in a wind tunnel experiment can vary between 10 °C and 50 °C, the pressure estimation might yield significant errors unless a correction to the pressure estimation is made for the temperature variation. Some researchers used infrared cameras to measure the temperature distribution on the model.<sup>88</sup> Others utilized a TSP for half of the symmetric model surface assuming that on each half of the model surface, the same temperatures would be generated throughout the experiment.

Although the previous approaches provided usable data, the most successful results in temperature correction of pressure data come from dual-luminophore pressure/temperature sensitive paints.<sup>50,89</sup> Nevertheless, finding a compatible PSL and TSL has made it difficult to formulate such coatings. Commonly used PSLs and TSLs emit generally in the same wavelength region. Moreover, they interact with each other when incorporated in a single film. Though, there are several successful dual-luminophore pressure/temperature sensitive paints reported in literature. Gouterman's group at University of Washington developed a dual-luminophore coating where EuD2

was used as temperature sensor and PtTFPL was used pressure sensor. EuD2 has a temperature sensitivity of  $-4.42\%-\text{°C}^{-1}$ , and PtTFPL has a B value of  $\sim 0.65$  in the polymer matrix they used.<sup>38</sup> Another dual PSP system has been reported by Mitsou et al. in which they utilized Rhodamine B as temperature sensor and PtTFPP as pressure sensor in poly-IBM-co-TFEM. Although Rhodamine B was not very temperature sensitive in that medium and overlap of Rhodamine B emission with PtTFPP emission decreased the sensitivity of pressure measurements, they were able to get good results for a verification test on a wing model in wind tunnel.<sup>90</sup> Hradil et al. dispersed MFG and Rudpp in a sol-gel matrix for which they were able to use a single gated camera for the acquisition of luminescence decays of both luminophores which have temporally separated lifetimes.<sup>50</sup> Coyle et al. proposed a lifetime based dual-luminophore PSP;  $\text{La}_2\text{O}_2\text{S}:\text{Eu}^{3+}$  thermographic phosphor along with PtTFPP dispersed in FIB. The temperature dependence of the lifetime of  $\text{La}_2\text{O}_2\text{S}:\text{Eu}^{3+}$  is  $-1.9\%-\text{°C}^{-1}$ , while PtTFPP has a B value of  $\sim 0.85$  with significant nonlinearity of Stern-Volmer plot in dual paint.<sup>49</sup>

### **Self-Referencing and Binary PSPs**

Self-referencing paints contain a second luminophore which is pressure and temperature insensitive (RL). In theory, the luminescence of the second luminophore is proportional to illumination and concentration of luminophore, which opens up the possibility of internal referencing thereby eliminating the need for a wind-off (reference) image.<sup>91</sup> However, it turned out that the ratios ( $I_{\text{PSL}}/I_{\text{RL}}$ ) obtained from internal referencing vary with the thickness of the film.<sup>92</sup> The theoretical basis of internal referencing assumes a linear response of emission to illumination, linear absorption, reflection, and scattering processes. Besides, self-excitation and energy transfer between

the PSL and RL can not occur.<sup>93</sup> Since those conditions are not met in wind tunnel studies, a ratio-of-ratios  $(I_{\text{ref}}/I)_{\text{PSL}}/(I_{\text{ref}}/I)_{\text{RL}}$  has been used instead for to compensate for spatial and temporal variations in incident light intensity and varying luminophore concentration in the binder. However, using a ratio-of-ratios increases the overall uncertainty of results, requires larger number of images, and lacks the advantages of an ideal self-referencing paint. Nonetheless, it successfully eliminates the image registration problem due to model movement which is not solved by simple ratioing  $I_{\text{ref}}/I$ .<sup>93</sup>

Binary paints are very similar to self-referencing paints; the only difference is that instead of using a pressure insensitive luminophore, a temperature sensitive luminophore is used as reference. Then, the ratio of two luminophore intensities partially or totally offsets the temperature dependency of PSP. Khalil et al. used MgTFPP as pressure independent but temperature dependent reference sensor along with PtTFPL as pressure sensor in FIB. MgTFPP displays  $\sim -0.2\% \cdot ^\circ\text{C}^{-1}$  temperature dependency while PtTFPL shows  $\sim -0.3\% \cdot ^\circ\text{C}^{-1}$  temperature dependency. Ratioing the MgTFPP emission to the PtTFPL emission reduces the temperature dependence to  $\sim -0.1\% \cdot ^\circ\text{C}^{-1}$ .<sup>56</sup> Nonetheless, when a painted binary coupon was tested by using two camera images which were obtained through filters that correspond to each dye's emission, the image ratio measured at constant pressure and temperature revealed spatial non-uniformity: a standard deviation of 1.17% which equates 0.29 psi pressure error. This noise was then eliminated by using ratio-of-ratios.<sup>56</sup>

### **Three-Component PSPs**

A three-component PSP includes three luminophores in the binder: a PSL, a TSL, and a reference luminophore. Such paint has been envisioned to eliminate both

temperature and image registration problems by using three filters corresponding to the emissions of the three sensors. Nonetheless, three-component PSP has not yet been realized. In the present work we developed a three-component PSP by dye co-precipitation with PAN nanospheres. More information will be given in Chapters 2 and 3 about the PSP properties of three-component PSP.

### **PSP Measurement Setup**

Intensity based measurements are used more frequently than lifetime based systems because of their relative ease of setup and use. Although lifetime imaging has some advantages over intensity imaging, it is difficult to simultaneously measure the intensity time profiles at all points on the model at the timescales of luminescence lifetimes. In the following section, a thorough discussion is given for both measurement techniques.

#### **Intensity-Based Imaging**

The PSP coated model is illuminated by a diffuse light source (either continuous or flash) and imaged by a CCD camera. The pressure at each point is determined from the ratio of wind-off to wind-on images. A and B constants of equation (1-22) should be known for calibration purposes before-hand:

$$\frac{I_{ref}(x, y)}{I(x, y)} = A + B \frac{P(x, y)}{P_{ref}(x, y)} \quad (1-22)$$

where x,y are spatial coordinates on model. Scientific grade CCD cameras made this method available for data acquisition. They are almost ideal light detectors with excellent quantum efficiency, high signal-to-noise ratio (SNR), linear response, and up to 16 bits of dynamic range. The major disadvantages are high cost and low imaging rate.<sup>3</sup>

Several types of illumination sources have been employed in wind-tunnel studies. Pulsed and continuous-wave lasers have been broadly used in PSP experiments. Pulsed

lasers were proven to be very helpful in unsteady measurements since pulse duration can be extremely short (5-10 ns). Maintaining a uniform illumination field with a laser source can be problematic. Therefore, UV lamps and arrays of blue LEDs are now the most frequently used excitation sources in experiments. Engineers try to avoid using UV lamps -if possible- for both safety reasons and lesser stability of output light compared the emission of blue LED arrays.<sup>94</sup> Flash illumination technique is exploited for the paints where photodegradation a concern or where high temporal resolution is needed. This technique has also been employed in unsteady applications and in the tests of rotation machinery, such as helicopter rotor blades and engine turbines.<sup>3</sup>

The filters should be installed in front of the lamps and cameras to avoid possible interference of light from illumination source. At ambient conditions, the luminescence emanating from the PSP is only a few percent of the excitation light intensity. Thus, special care must be taken when choosing and positioning the filters.

The PSP should possess the desired photophysical and mechanical properties. Apart from good pressure sensitivity of luminescence response, the paint should have high quantum efficiency, short time response, and good photostability. Pressure sensitivity is determined by Stern-Volmer coefficients of the paint response (A and B). One might want to use a PSP with highest B coefficient to increase the accuracy of measurement. However, high value of B means low signals at high air pressure and this leads to a decrease in SNR which affects accuracy of results.<sup>84</sup> For 0-1 atm pressure range, B values in the range 0.4-0.8 yield approximately the same accuracy. Accuracy decreases outside this range.<sup>3</sup>

Coatings can alter the aerodynamics of the model either by changing the shape of the model (for instance adding local thickness) or by increasing the roughness of surface.<sup>95</sup> The paint should be as thin as possible, and should be able to be polished if the roughness is a problem.

### **Lifetime Imaging**

Lifetime systems exploit the luminescence decay time by using time resolved measurements of luminescence.<sup>96,97</sup> The paint should either be excited by a flash light or by a modulated light source. Since lifetime measurements are an intrinsic property of the luminophore used in the binder, the results are not affected by the variation in illumination light intensity over paint or by varying luminophore concentration in the coating.<sup>49,50</sup> Hence, there is no need for a reference image in lifetime measurements. Nevertheless, instrumentation and setup for lifetime imaging is complex and expensive. Noise limitations sometimes prohibit the necessary level of accuracy required in pressure measurements.<sup>42,50,98</sup> So far, intensity based measurements are most common and mature systems in PSP technology.

There are two different lifetime methods; pulsed lifetime imaging and phase-shift imaging. In pulsed lifetime imaging,<sup>76</sup> the camera must be able to operate with an integration time which is at least a thousand times shorter than a conventional scientific CCD camera can achieve. This is because luminophores used in PSPs generally have luminescence decay profiles in the  $\mu\text{s}$  range. Thus, in lifetime based imaging, intensified CCDs are used. Here the intensifier acts as an ultrafast shutter or gate to control the exposure time on the CCD. After the flash excitation, the images are collected at two equal time intervals and the ratio of images acquired during two equal gates can be

related to the lifetime of the luminophore at that pressure and temperature. Figure 1-7 shows how to measure lifetime from two time resolved images. The related equations are provided on the graph. Nowadays, it is even possible to decrease the time intervals to ns range with intensified CCD cameras. However, those cameras suffer from low SNR which decreases the accuracy of results.

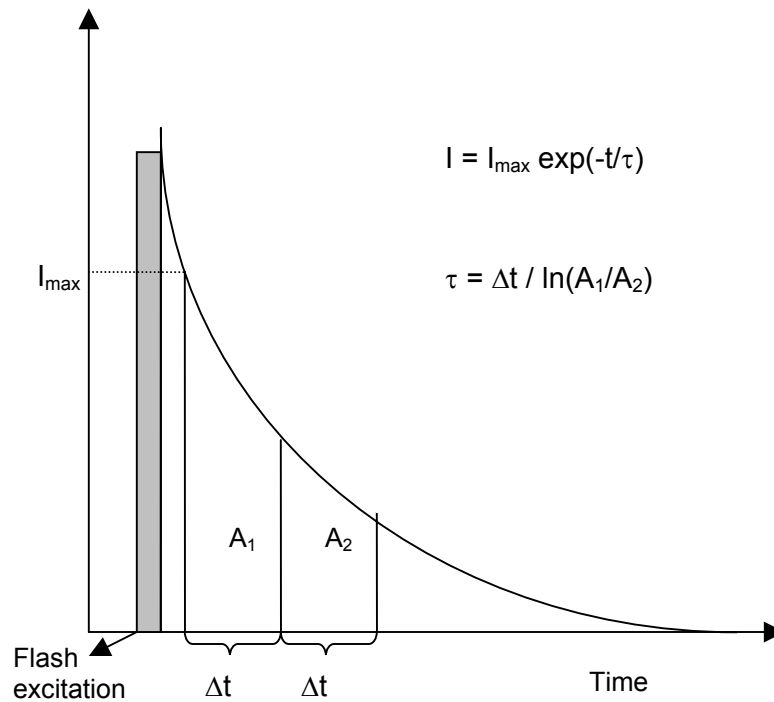


Figure 1-7: Measuring lifetime from two time-resolved images in pulse imaging method.<sup>3</sup>

In addition to pulse excitation, modulated excitation can also be used in lifetime imaging combined with phase sensitive detection.<sup>69,99-101</sup> The sinusoidal excitation is followed by a modulated emission which is delayed in phase ( $\phi$ ). The extent of phase delay can be related to oxygen concentration by using following equations:

$$\phi = \arctan(\omega\tau) \quad (1-23)$$

$$\omega = 2\pi f \quad (1-24)$$

The images are acquired with a phase-sensitive camera during two gated intervals. One gate is in phase with the excitation signal whereas the second is out of phase as shown in Figure 1-8.

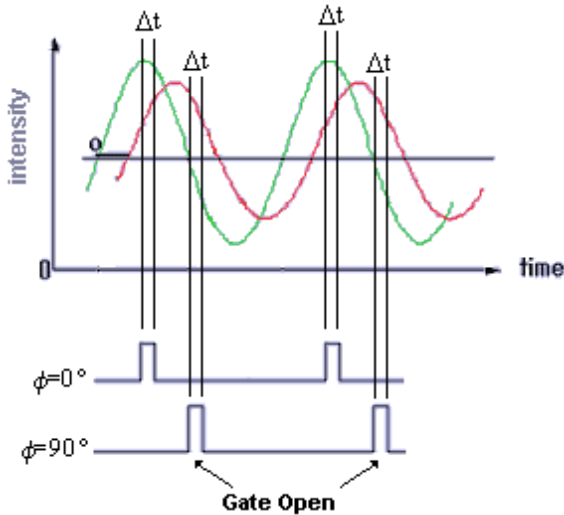


Figure 1-8: Measurement scheme for phase-shift imaging method.

### Image and Data Analysis

#### Image Registration

When the wind tunnel is running, a model sometimes deforms under air load or translates as a solid body. The intensity based setup requires that a wind-off image is ratioed to a wind-on image. Therefore, it is important that the wind-on intensity at each point be normalized by the wind-off intensity at the same point. Accordingly, the wind-on images should be spatially registered to wind-off images. This is done by a computer algorithm. There are many types of image registration methods. The simplest one is a projective transform which is used for solid-body movement of a two-dimensional object. If one wishes to register wind-on( $x,y$ ) coordinates to wind-off( $x',y'$ ) coordinates where ( $x,y$ ) and ( $x',y'$ ) are the corresponding physical points of the model which are in alignment, the following equations can be used effect the projective transformation.<sup>3</sup>

$$x = \frac{a_1x' + a_2y' + a_3}{c_1x' + c_2y' + 1} \quad (1-25)$$

$$y = \frac{b_1x' + b_2y' + b_3}{c_1x' + c_2y' + 1} \quad (1-26)$$

Since there are 8 unknowns in the above equations, at least four target points are needed to achieve a solution. These 4 target points should be easily identifiable on both wind-off and wind-on images. The projective transformation is the simplest image registration method, however, in most wind tunnel experiments a model might deform or movement might occur at some parts of the model like wings.<sup>102</sup> Then, more complicated image registration algorithms are needed for such cases. Many computer codes were developed for such situations.<sup>103</sup>

Fortunately, image registration error decreases with decreasing dynamic pressure. Because the registration accuracy depends on the magnitude of brightness of pressure gradients, such images are obtained at low pressures. Since model displacement is not much at high dynamic pressures, the image registration is less of a problem. However, the registration errors should be kept less than 0.5 pixel in most of the wind tunnel experiments for reliable results.<sup>3</sup>

### **Calibration-PSP Working Equations**

There are three main calibration methods for PSP data: in-situ, a priori, and k-fit method.

#### **In-situ Calibration**

In-situ calibration requires reliable pressure tap data.<sup>84,96,104</sup> Therefore, there needs to be enough pressure taps installed on the model for this type of calibration. The pressure tap data obtained throughout a wind tunnel experiment are used to correlate to

the PSP intensity ratio. Pressure is, generally, represented as a polynomial function of intensity ratio.<sup>89</sup>

$$p = c_0 + c_1 \frac{I_{ref}}{I} + c_2 \left( \frac{I_{ref}}{I} \right)^2 + \dots \quad (1-27)$$

A least squares fit of the data gives the calibration coefficients. In this method, the temperature dependence of data is absorbed in the coefficients. For most cases, above equation is a first order polynomial with  $A = -c_0/c_1$  and  $B = p_{ref}/c_1$  (Equation (1-11)).

In-situ calibration also requires finding the exact location of pressure taps on the model. Sometimes pressure taps are too small to be seen in the images. Photogrammetry is used to estimate the tap coordinates on the image provided that the spatial coordinates of the taps are known already. What this method basically does is that the image plane, which is 2-dimensional (x,y), is converted to 3-dimensional coordinate systems (X,Y,Z). This is done by using several targets whose spatial coordinates are known.<sup>105</sup>

### **A-priori Calibration**

A test coupon is painted and put in a calibration chamber.<sup>96</sup> Pressure and temperature are varied in that chamber, and the intensity of a PSP coated coupon is measured. Then the known pressure is expressed as a biquadratic function in the following form:

$$p = a_0 + a_1 \left( \frac{I_{ref}}{I} \right) + a_2 \left( \frac{I_{ref}}{I} \right)^2 + a_3 T + a_4 T \left( \frac{I_{ref}}{I} \right) + a_5 T \left( \frac{I_{ref}}{I} \right)^2 + a_6 T^2 + a_7 T^2 \left( \frac{I_{ref}}{I} \right) + a_8 T^2 \left( \frac{I_{ref}}{I} \right)^2 \quad (1-28)$$

At least nine pressure-temperature combinations should be known in order to solve for nine unknown coefficients. This function is then applied to wind tunnel data to obtain the pressure estimates at each pixel on the image.

### **k-Fit Method**

The k-fit method is a hybrid method between in-situ and a priori calibration techniques. In this method, pressure variation at a known temperature is expressed as a second order polynomial function of ratioed intensities by using a priori calibration technique.<sup>106</sup> Then the effect of temperature differences between wind-off and wind-on conditions are defined by a factor k, which is then used in in-situ calibration functions for pressure tap data.<sup>3,89</sup>

$$\frac{P}{P_{ref}} = C_1 + C_2 \left( \frac{kI_{ref}}{I} \right) + C_3 \left( \frac{kI_{ref}}{I} \right)^2 \quad (1-29)$$

### **Uncertainties of PSP**

There are many sources of uncertainties that affect the accuracy of PSP measurements.<sup>84</sup> Some of them are related to calibration errors which arise from incomplete representation of the PSP response. Another set of errors arise due to the measurement system. Finally, there is another set of errors arising from the signal analysis. Below are several sources of errors which are described briefly.

### **Calibration Error**

The mathematical representation of the PSP response is not exact. As discussed earlier, both in-situ and priori calibration methods are used for measurements. However, both methods have drawbacks. The in-situ calibration uncertainty is a measure of the overall PSP uncertainty within the range of conditions at the pressure taps.<sup>104</sup>

Illumination changes, temperature changes and registration errors cause variations in the

calibration. Since the pressure taps do not span the full range of pressures on the model, the calibration has to be extrapolated, which adds more uncertainty in the measurement. If the paint is 'ideal',<sup>41</sup> then the uncertainty that comes from extrapolation can be decreased. In general, in-situ calibration uncertainty is ~1% of flow pressure.<sup>3</sup>

The a-priori calibration uncertainty error corresponds to minimum uncertainty over the range of calibration temperatures and pressures. However, photodegradation, humidity, and contamination effects are neglected. Moreover, PSP response on the model is usually slightly different than that of a calibration coupon, due to possible differences in the thickness of paint layers and model geometry.<sup>96</sup> A-priori calibration method requires the information of temperature distribution on the model.<sup>3</sup>

Where the range of pressures measured by pressure taps does not cover the pressure range encountered by the paint, it is then useful to implement k-fit method for data calibration. For that reason, ideal PSPs are preferred over regular paints for this calibration method.<sup>3</sup>

### **Errors Due to the Measurement System**

Detector shot noise is unavoidable, but it can be decreased by summing over many images at the cost of increased data acquisition time (Photodetector noise).<sup>9,84</sup> CCD lenses deposit more light near the center of image than near the edges. If the model moves or deforms between wind-off and wind-on conditions, flat-field correction is necessary. The need for flat field error correction becomes more important at especially high signal levels (Flat-field error).<sup>3</sup> A tare image should be subtracted from the data images in order to eliminate the effects of camera readout bias, dark charge, and ambient light (Tare correction).<sup>3</sup> Maintaining lamp stability within 1% is essential for PSP measurements. LEDs are better as stable illumination sources than UV lamps (Temporal

variations in illumination field).<sup>84</sup> Luminescence is sometimes reflected between two or more painted surfaces at right or acute angles to each other. Ruyten et al. developed an analytic correction method that predicts diffuse reflections from all painted surfaces (Self-illumination corrections).<sup>84,107</sup>

### **Errors due to Signal Analysis**

Registering the data image to a reference image eliminates the variations in signal intensity caused by the variations in paint thickness and excitation light across the surface of the model. Nonetheless, it is sometimes difficult to align wind-on and wind-off images at a desired level, which induces problems in obtaining correct results.

The largest source of uncertainty in PSP measurements is the temperature variation across the model surface.<sup>84,104</sup> Sajben et al. showed that a temperature uncertainty of 1.5 °C is accounted for 93% of the pressure uncertainty. This reveals the importance of temperature correction in PSP measurements.

### **Applications of PSP**

There are many different applications of PSP in aerodynamic research, and more yet to come. Some examples are given below.

#### **Aerodynamic Models: Car Models, Delta Wing and Aircraft Models**

Gouterman's group tested MgTFPP-PtTFPL / FIB binary paint on a simplified automobile model.<sup>88</sup> Figure 1-9A displays the results obtained at the wind speed of  $V = 94 \text{ m s}^{-1}$  at three yaw angles  $-20^\circ$ ,  $0^\circ$ , and  $+20^\circ$ . High suction peaks appearing on the front and rear windshield headers arise due to high flow curvature and acceleration. The vortices developed on the model back window and model side at high yaw angles. It is also observed the flow acceleration has induced temperature variations on the model top surface. Engineers generally do not work with absolute pressure values; rather they use a

non-dimensional coefficient for pressure which is known as  $C_p$ .  $C_p$  is the ratio of the change in pressure due to the presence of the model to the dynamic pressure of the flow and can be calculated with the following expression:

$$C_p = \frac{p - p_\infty}{\frac{1}{2} \rho_\infty V_\infty^2} \quad (1-30)$$

where  $p$  is the air pressure,  $\rho$  is the air density,  $V$  is the speed of the flow, and  $\infty$  refers to a point far from the model.

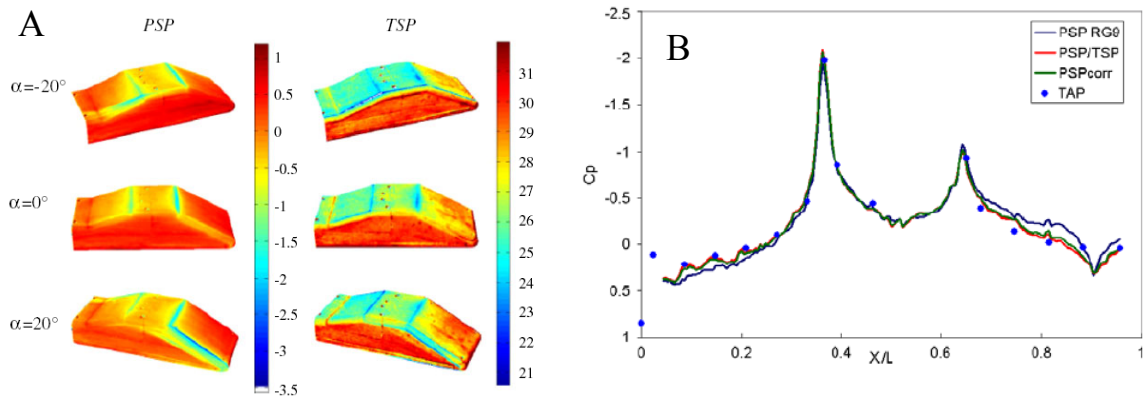


Figure 1-9: Imaging results. A)  $C_p$  results (left) and temperatures (right, in  $^\circ\text{C}$ ) from dual-luminophore PSP painted on a car model at three yaw angles:  $\alpha = -20^\circ$ ,  $\alpha = 0^\circ$ , and  $\alpha = 20^\circ$ . Flow direction from left to right. B) Comparison of pressure tap data with the results obtained from different PSP calibrations.<sup>88</sup>

The results are compared with pressure tap data located on model top surface (Figure 1-9B). PSP RG9 line corresponds to the pressure estimation of pressure sensitive dye without any correction for temperature. Since temperature variation is small on model surface, the error induced by temperature fluctuations is not very much, though it is evident. By taking simple ratio of PSP/TSP data, the temperature sensitivity of the coating can be decreased to -0.07% per Celsius and the results are improved. PSP<sub>corr</sub> data

are obtained from a more advanced calibration technique which accounts for all temperature variation on the model surface.<sup>88</sup> Figure 1-10 shows applications of PSPs to a double-delta wing model<sup>106</sup> and a civil transport model.<sup>3</sup>

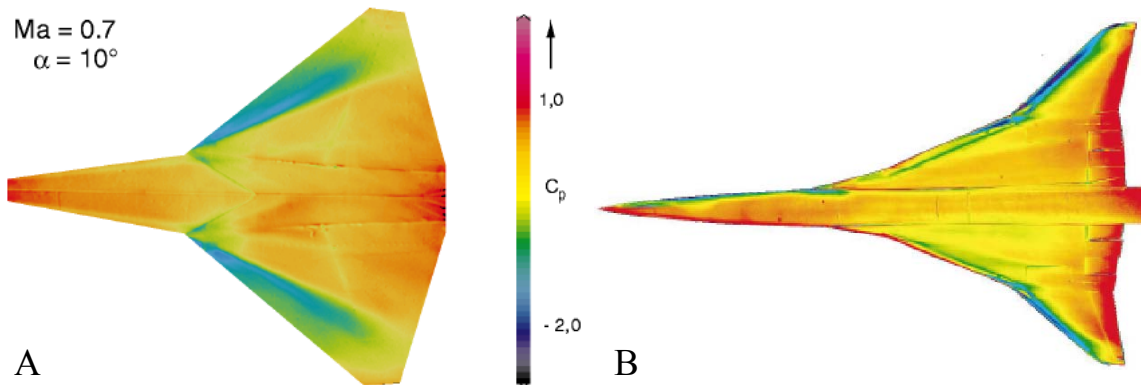


Figure 1-10: Surface pressure distribution. A)  $C_p$  distribution on a double-delta wing model. B) False colored ratioed image from high-speed civil transport model test. Low pressure is blue, and high pressure is red.<sup>3</sup>

### Turbine Blades

The application of PSP to the measurements on rotating models is important, because conventional pressure sensors on rotation parts are difficult and complex to implement.<sup>108</sup> As an example, a fan blade is illuminated with a flash light source which is fast enough to freeze the motion of blade. To increase the SNR, camera shutter is kept open and the blade is illuminated by repeated flashes when the blade comes into the same position. PSP is data corrected for temperature change by using a TSP on another blade at the same conditions.<sup>3</sup> Figure 1-11 shows the mass flow increasing from left to right.

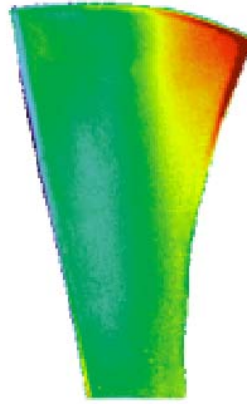


Figure 1-11: PSP results on a fan blade.<sup>3</sup>

### **Icing of Aircraft Parts**

PSP offers new measurements which were not possible with load analyses before. Measuring aerodynamics of iced aircraft parts is one of them. To perform such an experiment, wind tunnel is run wet to grow ice on the surface of the model. Then, PSP is applied to the ice surface and wind tunnel is run under dry but cold conditions. The data is analyzed using a conventional method.<sup>109</sup>

### **Detection of Sound Waves**

Sound pressure detection is possible by using pressure sensitive paints. McGraw et al. showed the principles of a phosphorescent microphone by replacing the diaphragm of a microphone with a thin film of PSP.<sup>110</sup> Changes in pressure were detected by monitoring changes in phosphorescence intensity due to cyclical variations of oxygen concentration caused by the sound wave. The pressure change corresponding to a given sound level is described in the following equation.

$$\Delta p = \sqrt{2\rho c_s I_{ref} 10^{SL/10}} \quad (1-31)$$

$\Delta p$  is the maximum amplitude of the pressure wave,  $\rho$  is the density of air,  $c_s$  is the speed of sound,  $I_{ref}$  is the reference sound intensity, and SL is the sound level in decibel (dB).

The PSP used in their experiments was able to detect acoustic pressure changes as small as 6 Pa in the frequency range 150-3500 Hz on a background pressure of  $10^5$  Pa. The same type measurements might be exploited for testing the response of PSPs to high frequency, low differential pressure fluctuations.<sup>110</sup>

### **Motivation and Summary of This Work**

The major problem in PSP technology is the inherent temperature sensitivity of PSP response which significantly affects the accuracy of the results. Eliminating and correcting the temperature problem of PSPs has been main area of research since the beginning of this technology. As well as other scientists and engineers in this field, we aimed to correct the temperature interference of PSP response. To achieve that we developed a dual-luminophore pressure/temperature sensitive paint from which we can get temperature information to correct the error induced by temperature variation in pressure estimation. Temperature sensitive luminophore has been co-precipitated with polyacrylonitrile nanospheres in order to minimize undesired interactions between TSL and PSL which were dispersed in a novel highly oxygen permeable polymer binder. Similar to this approach, we also developed a self-referencing and a three-component PSP. Emission overlap of the PSL and TSL has decreased the sensitivity of multi luminophore P/TSPs to pressure developed in this work. Then, we successfully applied a new PSP data analysis technique based on principal component analysis (PCA) which removes overlap problem. The results obtained from PCA technique is then compared to the results taken from a conventional data reduction procedure. PCA leads to more accurate results at the expense of computational time.

In this thesis, we discussed PSP properties of newly developed multi-luminophore coatings and we believe that they are good candidates for pressure measurements in aerodynamic research.

CHAPTER 2  
PREPARATION AND SPECTROSCOPIC PROPERTIES OF MULTI-  
LUMINOPHORE PRESSURE SENSITIVE PAINTS

**Introduction**

As outlined in Chapter 1, the measurement of surface air pressure distributions on aerodynamic models in wind tunnels is a key aspect in the design and testing of new aerospace vehicles. In the PSP technique, a luminescent coating combined with digital imaging technology is used to obtain high resolution surface pressure maps. Because of its inherent advantages, the PSP method has seen widespread use in wind tunnel testing.<sup>3</sup> The light emission intensity from a PSP system can be quantitatively modeled by the following form of Stern-Volmer equation:

$$\frac{I_{ref}}{I} = A + B \frac{p_{air}}{p_{ref}} \quad (2-1)$$

where  $I_{ref}$  is the emission intensity at the reference condition and A & B are the intercept and slope, respectively, of the modified SV equation.

Under ideal circumstances, the photoluminescence intensity of a PSP would respond solely to changes in the partial pressure of oxygen. However, it is well-known that the SV response of PSP systems also varies with temperature.<sup>6</sup> The temperature dependence arises from several factors including the temperature dependence of the non-radiative decay rate of the luminophore, and the diffusivity of O<sub>2</sub> in the polymer binder.<sup>11</sup> These factors were extensively explained in Chapter 1. The temperature dependence in the SV response can be viewed as interference in the measurement of air pressure with a

PSP system. In order to account for the temperature dependence, the SV equation must be modified as follows,

$$\frac{I_{ref}}{I} = A(T) + B(T) \frac{P_{air}}{P_{ref}} \quad (2-2)$$

where it is now explicit that the calibration coefficients  $A$  and  $B$  are functions of temperature.

One approach to account for the temperature dependence in the measurement of pressure is to include in the PSP a second luminophore which displays a temperature-dependent, pressure-independent luminescence intensity (dual-luminophore PSP). As is explained in Chapter 1, by using a dual-luminophore PSP, the temperature distribution over the model can be measured by monitoring the emission from the temperature sensitive luminophore, and then this information can be used to correct the temperature dependence of the pressure-sensitive luminophore. Although the concept of a dual-luminophore PSP system is straight-forward, in practice there are many issues which make it complicated to establish a usable and practical system. A key issue which must be resolved is that when two or more luminophores are incorporated in the same polymer matrix, they typically interact, leading to emission quenching, energy transfer, and other unpredictable effects.

An approach to eliminating the luminophore interactions is to separate or compartmentalize the pressure-sensitive and the temperature-sensitive luminophores in the binder. The characteristic separation length-scale must be smaller than the spatial resolution required in the PSP imaging system (0.1~1.0 mm). Consequently, the approach used to separate the dyes ideally will compartmentalize the dyes on a length

scale  $< 10 \mu\text{m}$ . Because of this limitation, to date there have been only a few examples of dual-luminophore PSPs reported in literature.<sup>38,49,50,56,90</sup>

The PSP technique also requires a reference condition for pressure measurements (equation (2-2)). Reference images are taken usually at ambient conditions (when the wind tunnel is not running). In a wind tunnel experiment, due to model movement or deformations, aligning the reference image with the run (wind-on) images is sometimes quite difficult. One of the best solutions is internal referencing where a reference sensor (pressure and temperature insensitive) is dispersed along with pressure sensor to obtain  $I_{\text{ref}}$  data. In theory, simple ratioing of the reference sensor intensity with PSL emission intensity ( $I_{\text{RL}}/I_{\text{PSL}} = I_{\text{ref}}/I_{\text{PSL}}$ ) should eliminate the necessity of acquiring a reference image in wind tunnel experiments. Towards the objective of addressing both the temperature and image registration problems, we sought to develop multi-luminophore PSPs that can measure temperature and pressure concurrently and that can also use a reference sensor for internal referencing.

Presented in this chapter is a novel approach for the formulation of multi-luminophore PSPs. The key to this approach is encapsulation of a temperature-sensitive luminophore (or a reference luminophore) in polymer-based nanospheres comprised of polyacrylonitrile (PAN). The PSP is then formulated by mixing the dye-loaded PAN nanospheres into the oxygen-permeable binder along with the pressure sensitive luminophore. Because the temperature-sensitive luminophore (or the reference luminophore) is compartmentalized within the PAN particles, molecular level interactions with the pressure-sensitive dye are minimized. In this chapter, we demonstrate the application of this approach to formulate multi-luminophore PSPs

wherein *tris*-(1,10-phenanthroline)ruthenium(II) dichloride (Ruphen), is used as the temperature sensor, and 5,10,15,20-tetrakis(pentafluorophenyl) porphyrin platinum(II) (PtTFPP) is used as the pressure sensor, and rhodamine 110 (Rh110) is used as the reference sensor. We have successfully developed dual-luminophore, self-referencing, and three-component PSPs that can be used in PSP research. To best of our knowledge, three-component PSP is the first of its kind and has been realized in our lab.

As part of this work, we have also developed a new highly oxygen-permeable polymer, poly(4-*tert*-butylstyrene-*co*-2,2,2-trifluoroethyl methacrylate) (poly-t-BS-*co*-TFEM), and this material is used as the binder for the dual-luminophore PSP. In this chapter, we will give detailed information for preparation of multi-luminophore PSPs and discuss their PSP properties. In the following chapter, the application of multi-luminophore PSPs to the imaging will be presented along with the data reduction techniques.

### **Photophysics of PtTFPP, Ruphen, and Rh110**

Before we go into the details of experimental results and discussion, it is necessary to give some background information regarding the photophysics of the luminophores used in this study. Their photophysical properties will help to understand why we chose those luminophores to be used in PSPs developed in our lab. The molecular structure of PtTFPP has already been given in Figure 1-5. PtTFPP is a fluorinated tetraphenyl porphyrin derivative and it is extremely photostable due to electron withdrawing effect of fluorine atoms which lowers HOMO substantially compared to non-fluorinated analogue. PtTFPP has absorption bands at 390 nm (Soret band,  $S_0 \rightarrow S_2$  ( $\pi, \pi^*$ )), 506 nm, and 540 nm (Q bands,  $S_0 \rightarrow S_1$  ( $\pi, \pi^*$ )). Because of the square symmetry of the porphyrins,  $S_1$  and

$S_2$  states have twofold orbital degeneracy. Pt(II) has  $(5d)^8$  electron configuration. The filled  $d_\pi$  orbitals  $5d_{xz}$ ,  $5d_{yz}$  strongly backbond to the empty  $e_g(\pi^*)$  degenerate porphyrin orbitals, resulting in spin-orbit coupling which facilitates the conversion from  $S_1(\pi, \pi^*) \rightarrow T_1(\pi, \pi^*)$ . This spin-orbit coupling is so strong that almost no fluorescence is observed from PtTFPP in 3-methylpentane, only phosphorescence is observed at 651 nm with a shoulder at 712 nm that corresponds to phosphorescence to a higher vibrational level of ground state. The lifetime of the phosphorescence is long ( $\tau = 120 \mu\text{s}$  in 3-methylpentane), which enables collisional oxygen quenching within decay lifetime of luminophore in proper mediums.

Ruphen is a member of ruthenium(II)  $\alpha$ -diimine family (Figure 1-4). The presence of phenanthroline ligands in Ruphen splits the d-orbital energy levels into three lower ( $t_{2g}$ ) and two higher ( $e_g$ ) orbitals. Transitions from  $t_{2g} \rightarrow e_g$  orbitals are forbidden. Even if such a transition occurs, the radiative rate is very low. However, the electrons can be promoted from ruthenium d orbitals to  $\pi^*$  orbitals of phenanthroline, the so-called metal-to-ligand charge transfer (MLCT) transition. This MLCT transition is the reason for strong absorbance of Ruphen near 450 nm. The complex undergoes ISC to the triplet MLCT state after absorption. This process is very efficient again due to presence of a heavy atom in complex as seen in PtTFPP. The triplet  $^3\text{MLCT}$  state decays by radiative ( $\sim 580 \text{ nm}$ ) and non-radiative pathways. Emission from the triplet  $^3\text{MLCT}$  state is long-lived enough for oxygen quenching ( $0.60 \mu\text{s}$ ). The relative levels of  $^3\text{MLCT}$  and  $^3\text{d-d}$  states determine the sensitivity of temperature dependence of Ruphen. The energy of the  $^3\text{d-d}$  state of Ruphen is slightly above the  $^3\text{MLCT}$  state. Increasing temperature populates

the  $^3d-d$  state, followed by rapid radiationless decay. This pathway is the origin of the observed decrease in Rhodamine emission upon temperature increase.

The molecular structure of rhodamine 110 (Rh110) is given in Figure 2-1. Rh110 is a laser dye and is extremely photostable. The absorption occurs ( $S_0 \rightarrow S_1$ ) at 498 nm and fluorescence is observed at around 521 nm. The Stokes shift is small, and absorption and emission spectra partially overlap. The lifetime of the fluorescence is only 4 ns, and it is not affected by the changes in the environment such as pressure and temperature variations. Moreover, the emission quantum yield of Rh110 is very high, 0.91.

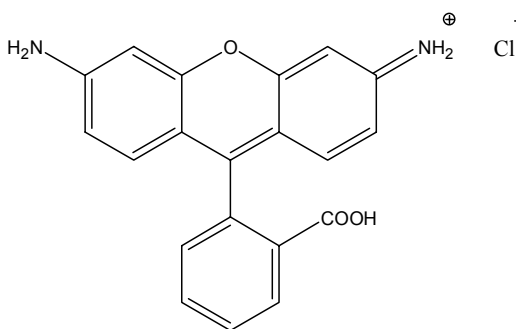


Figure 2-1: Chemical structure of Rhodamine 110.

## Results and Discussion

### Binder

For PSP applications, it is desirable to use a polymer binder that has high oxygen permeability as well as provides a medium in which the luminescent dye is stable with respect to photodegradation.<sup>12</sup> In a number of investigations it has been shown that fluorinated acrylate polymers display these properties.<sup>59,60</sup> Recently, several other investigations have highlighted the advantages of using co-polymers as binders for use as PSPs. For example, Amao and co-workers reported the use of a copolymer of styrene and 2,2,2-trifluoroethyl methacrylate (poly-styrene-co-TFEM) as the binder in a dual-luminophore PSP application. In this polymer binder, PtTFPP displays a B value of 0.70.

Although the poly-styrene-co-TFEM binder reported by Amao<sup>63</sup> has useful properties, we felt that it was necessary for the PSP to exhibit a larger SV pressure response in order to increase the sensitivity of the coating to variation in air pressure. In order to achieve a coating with higher oxygen permeability, we replaced styrene with 4-t-butylstyrene (t-BS), on the basis of previous work which shows that the diffusivity of oxygen in poly-t-BS is considerably higher than in polystyrene.<sup>111</sup> Thus, in the present investigation a co-polymer was prepared using t-BS and TFEM as the monomers, and the pressure response of PSP coatings was compared to the respective homopolymers using PtTFPP as the luminophore.

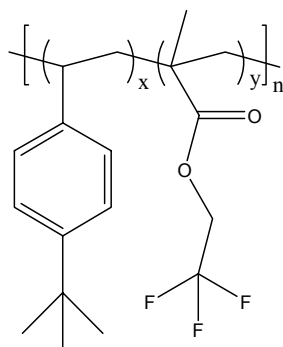


Figure 2-2: Chemical structure of poly-t-BS-co-TFEM.

Table 2-1 lists the air pressure and temperature response of these three coatings: 1) the poly-t-BS homopolymer; 2) poly-t-BS-co-TFEM (a co-polymer of 0.82:1 composition in mole amount); 3) the TFEM homopolymer. As can be seen from the data, the pressure response of the poly-t-BS-co-TFEM coating is intermediate between that of the coatings based on the two homopolymers. Interestingly, the pressure response of the poly-t-BS<sub>0.82</sub>-co-TFEM co-polymer coating is higher than that of the poly-TFEM-based coating. This is consistent with the fact that poly-t-BS is more gas permeable compared to poly-TFEM. Although the pressure response of the poly-t-BS coating is higher than

that of the co-polymer, this material has poor mechanical properties-- the coating was brittle and did not adhere well to substrates. By contrast, the poly-t-BS-co-TFEM coating has excellent mechanical properties and adheres well to the substrate.

Table 2-1: The B values and temperature dependencies of homopolymers and copolymer.

polymer	B <sup>a</sup>	%T/°C <sup>b</sup>
Poly-t-BS	0.93	0.30
Poly-TFEM	0.81	0.68
Poly-t-BS <sub>0.82</sub> -co-TFEM <sub>1</sub>	0.90	0.53

<sup>a</sup> The value of B is calculated according to equation (2-1). Regression coefficients for fitting were 0.990 for poly-t-BS and poly-TFEM, 0.989 for copolymer.

<sup>b</sup> Regression coefficients for fitting were 0.999 for all cases. Temperature dependency measured at 14.7 psi.

### Ruphen Incorporated Nanospheres

Polyacrylonitrile nanoparticles that contain Ruphen and prepared as described in the experimental section were characterized by scanning electron microscopy (SEM). Figure 2-3A shows an SEM image of film of the Ruphen/PAN nanoparticles that was produced by air-brushing a very dilute dispersion of the particles in acetone solvent. Individual particles are resolved in this image, and it can be seen that the sample is polydisperse, with particle sizes ranging from 10 nm to 90 nm and an average size of approximately 50 nm. Although it is possible to obtain isolated particles from the dilute dispersion, other SEM imaging experiments suggest that the particles are aggregated in the dispersion. In particular, the SEM images shown in Figures 2-3B and 2-3C were obtained from a glass surface that was coated with the nanoparticles by dipping the substrate into the dispersion. In these images it is evident that the particles exist in an aggregated form, wherein the individual nanoparticles are clumped together to form a more-or-less continuous network extending on a length scale of 1  $\mu\text{m}$  or more.

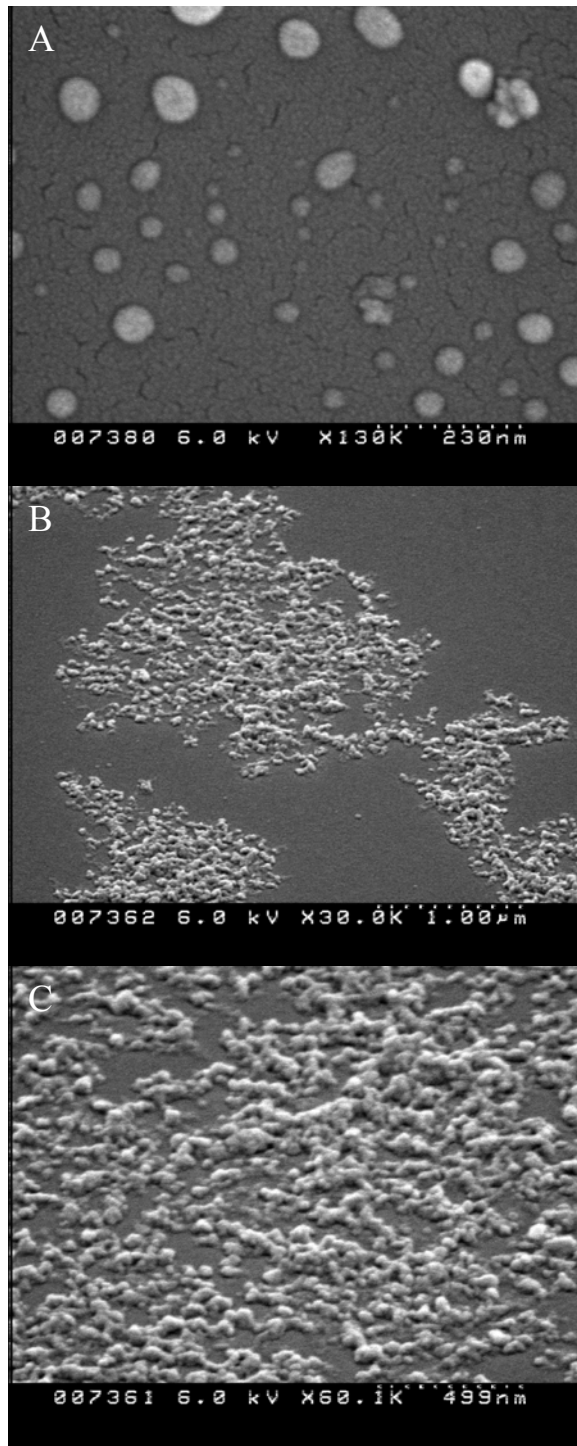


Figure 2-3: Secondary electron microscopy images of Ruphen/PAN nanospheres in acetone solution for samples A) sprayed onto glass substrate from a low concentrated nanosphere solution, B) dipped into nanospheres solution, C) a magnified portion of image B.

Despite the presence of nanoparticle aggregation, the material disperses relatively uniformly in the poly-t-BS-co-TFEM binder. In order to characterize the properties of the particles in the coating, fluorescence images were obtained on a film of the dual-luminophore PSP formulation consisting of the Ruphen/PAN particles dispersed into the PtTFPP / poly-t-BS-co-TFEM binder. Figure 2-4A illustrates a false-color image of the luminescence from the coating obtained using an epifluorescence microscope, with imaging at 560 nm (the wavelength corresponding to the Ruphen emission, see below). This image illustrates that although there is emission distributed across the entire field of view; the emission is spatially heterogeneous, suggesting that the Ruphen/PAN particles are aggregated in the poly-t-BS-co-TFEM matrix.

Despite the observation of heterogeneity on a microscopic length scale, an image obtained of a macroscopic object coated the same material displays little or no graininess. In particular, the false color image in Figure 2-4B was obtained by using a CCD camera (fitted with a 550/40 nm bandpass filter) to image a 1.5 x 3.0 inch plate. The image was obtained while the object was illuminated with a 460 nm LED array light source. The spatial non-uniformity in the intensity moving from top to bottom and left to right across the plate mainly results from the fact that the illumination provided by the LED array is not uniform and because there is a 13° C temperature gradient across the vertical axis of the plate (see below for more information). More important is the fact that on a small length scale the emission intensity is relatively uniform. The spatial uniformity of the emission is even more evident in image shown in Figure 2-4C. This image is obtained by ratioing two separate images; one with a temperature gradient on the plate and the other one at a reference condition (constant temperature and pressure). The

ratioing eliminates the effects of the non-uniform illumination field and thickness variation of paint luminescence; leaving the temperature gradient observable on the emission intensity. It is quite evident from these images that the luminescence from the dual-luminophore coating is homogeneous on the larger length scale characteristic of PSP measurements, and on the basis of this experiment it is believed that the coating is suitable for use in PSP imaging applications.

### **One-Component PSP: PtTFPP / Poly-t-BS-co-TFEM**

As is typical for PSP formulations, the luminescence intensity of PtTFPP in the t-BS and TFEM based coatings is temperature dependent. However, interestingly the temperature dependence of the dye's emission is lower in the t-BS coating, consistent with the fact that the oxygen diffusivity is higher in this matrix compared to TFEM.<sup>11</sup> The temperature dependence of the PtTFPP emission in poly-t-BS is also less than it is in poly-t-BS-co-TFEM than in poly-TFEM.

On the basis of the screening experiments, poly-t-BS-co-TFEM was selected as the binder for the multi-luminophore PSP system. In these experiments a 1 x 1 cm glass slide coated with the PSP formulation was placed into a small sample chamber that allows control of air pressure ( $p_{\text{air}}$ ) and temperature (T). The chamber was installed into the sample compartment of a SPEX Fluorolog allowing measurement of emission spectra from the coating as a function of  $p_{\text{air}}$  and T. Figure 2-5 illustrates the variation of PtTFPP phosphorescence in poly-t-BS-co-TFEM binder over a pressure range of 0.06 – 14.77 psi. Stern-Volmer plot of paint response is given Figure 2-6. The pressure response of the PtTFPP luminescence is strong with the intensity varying by approximately a factor of 11 from vacuum to ambient pressure; however, the Stern-Volmer plot is slightly non-linear, with some downward curvature at low pressure.

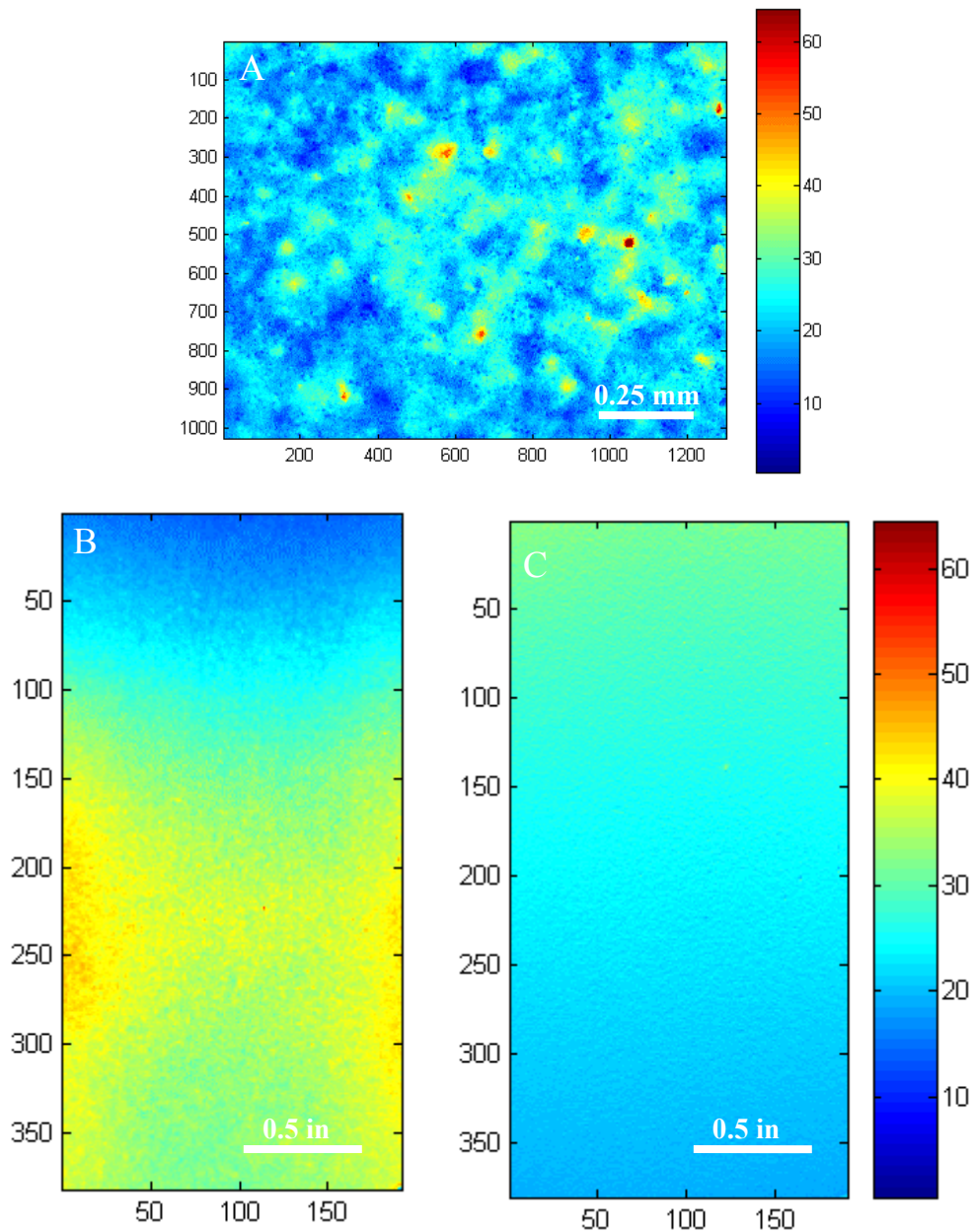


Figure 2-4: Images for RuPhen doped nanosphere emission. A) Fluorescence microscope image for RuPhen/PAN nanospheres dispersed in poly-t-BS-co-TFEM. Image size is 1.36 mm X 1.72 mm. B) Raw macroscopic CCD image for RuPhen/PAN nanospheres dispersed in poly-t-BS-co-TFEM sprayed on an aluminum coupon. The emission is collected through 550/40 nm bandpass filter. There is a 13 °C temperature gradient between the top and bottom of the sample. Image size is 3 in X 1.5 in. C) Same as B, but ratioed with a reference image which is collected at constant pressure and temperature. Ratio values are multiplied by 30.

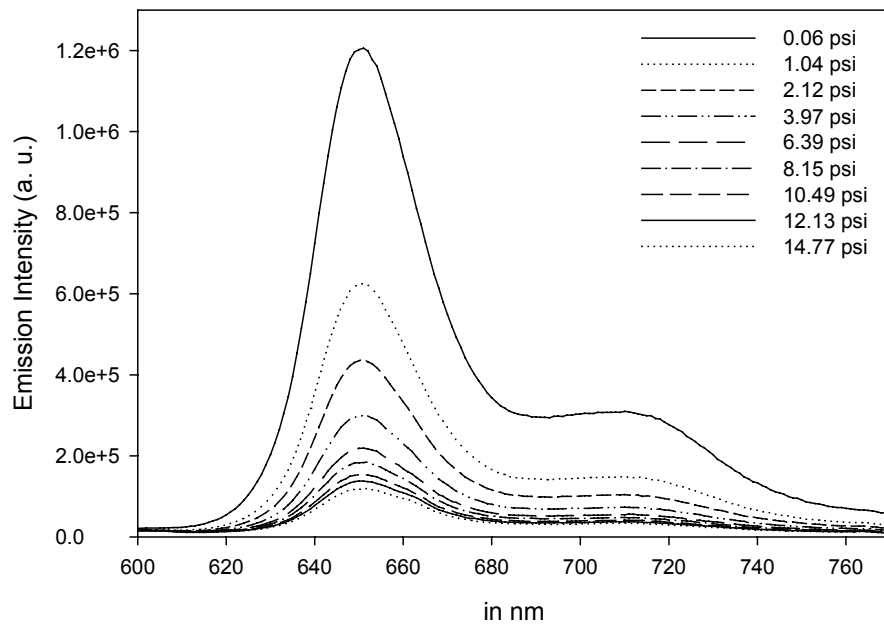


Figure 2-5: Variation of PtTFPP emission with pressure in poly-t-BS-co-TFEM binder at 312 K. The sample was excited at 465 nm.

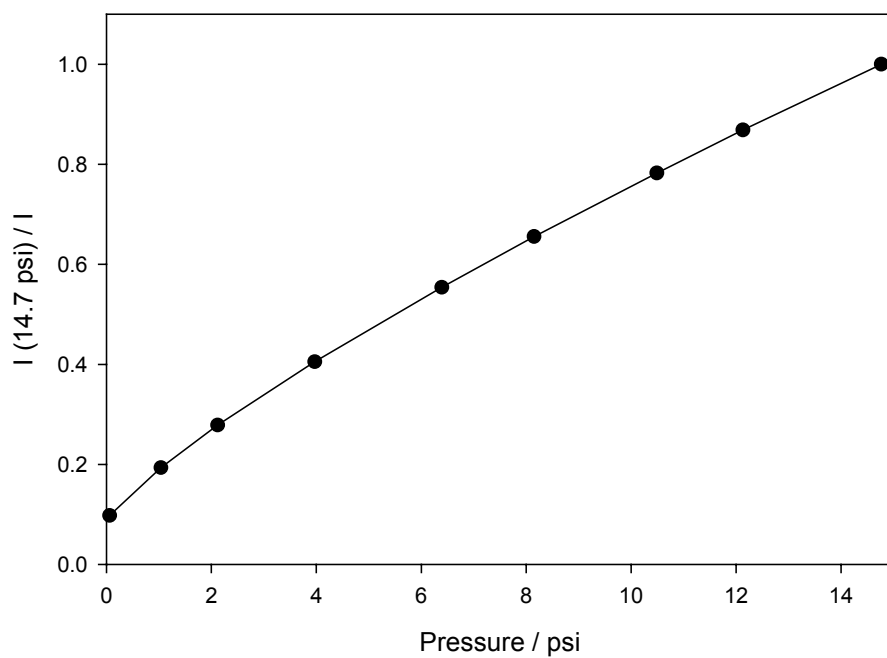


Figure 2-6: Stern-Volmer plot for PtTFPP in poly-t-BS-co-TFEM at 312 K. PtTFPP emission is integrated over an area of 635-670 nm.

PtTFPP emission also varies with temperature in poly-t-BS-co-TFEM binder (Figure 2-7) as it does in other PSPs. The temperature dependence of the PtTFPP luminescence is  $-0.53\%-\text{°C}^{-1}$  at 14.7 psi (Figure 2-8) and  $-0.50\%-\text{°C}^{-1}$  at vacuum. Thus, the temperature dependence of this coating system is nearly independent of pressure, which is a desirable property for PSP binders. PtTFPP / poly-t-BS-co-TFEM coating can be referred as an “ideal” PSP system.<sup>12</sup>

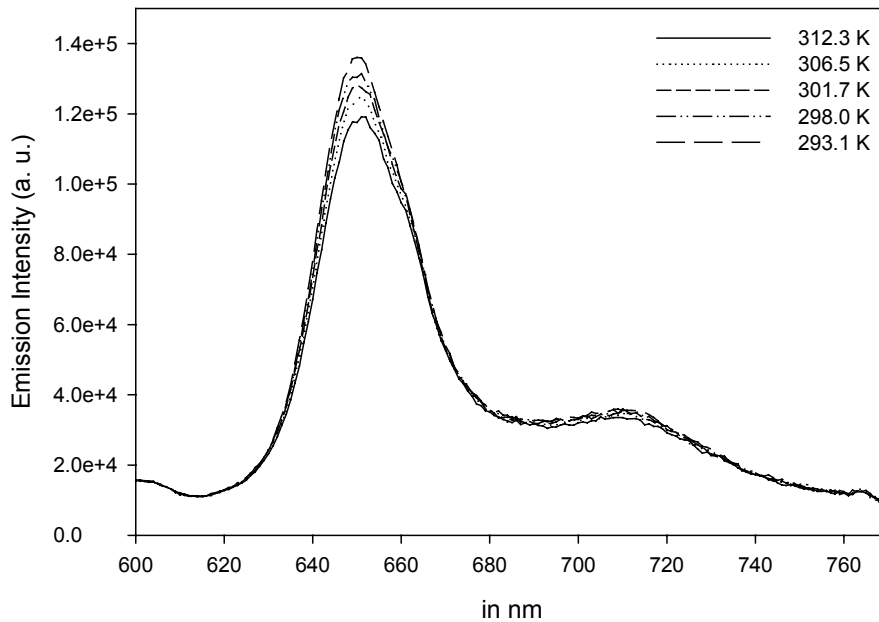


Figure 2-7: Variation of PtTFPP emission with temperature in poly-t-BS-co-TFEM binder at 14.77 psi. The sample was excited at 465 nm.

Note that the PSP films are dried at  $100\text{ °C}$  for half an hour; non-annealed PtTFPP / poly-t-BS-co-TFEM coating has a temperature dependency of  $-0.82\%-\text{°C}^{-1}$ .<sup>15</sup> Finally, the PtTFPP emission is very stable in poly-t-BS-co-TFEM, where it is observed to photodegrade at a rate of approximately  $0.5\%-\text{hr}^{-1}$ .

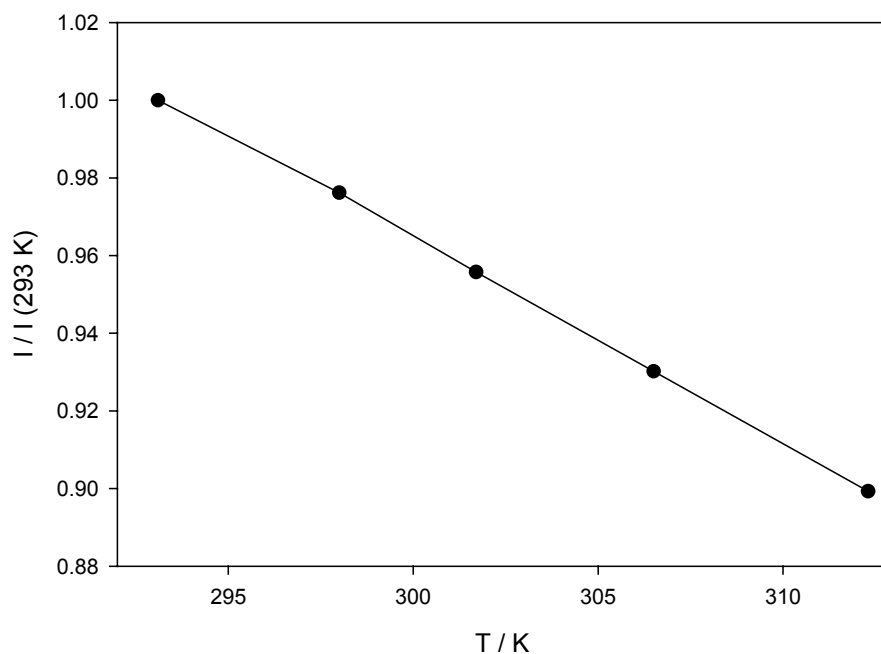


Figure 2-8: Temperature response of PtTFPP / poly-t-BS-co-TFEM coating at 14.77 psi.

#### **Dual-Luminophore PSP: PtTFPP-Ruphen/PAN / Poly-t-BS-co-TFEM**

The effects of temperature and pressure on the emission spectral properties of the PtTFPP-Ruphen/PAN / poly-t-BS-co-TFEM PSP coating were characterized. Figure 2-9 illustrates emission spectra obtained from the dual probe PSP (with excitation at 465 nm) at various pressures ranging from 0.05 – 14.7 psi at  $T = 293^{\circ}\text{C}$ . Figure 2-10 shows spectra obtained at  $p_{\text{air}} = 14.7$  psi and five temperatures ranging from 282 – 323 K. In each case the emission spectra feature two main components: 1) a broad, structureless band that ranges from 525 – 625 nm arising from Ruphen; 2) a band with maxima at 650 and 710 nm arising from PtTFPP. As can be seen from spectra obtained at constant temperature, the PtTFPP emission intensity decreases substantially with increasing pressure, whereas the higher energy emission from Ruphen decreases only slightly with

pressure. By contrast, the spectra obtained at various temperatures (Figure 2-10) show that the emission from both chromophores decreases substantially with temperature.

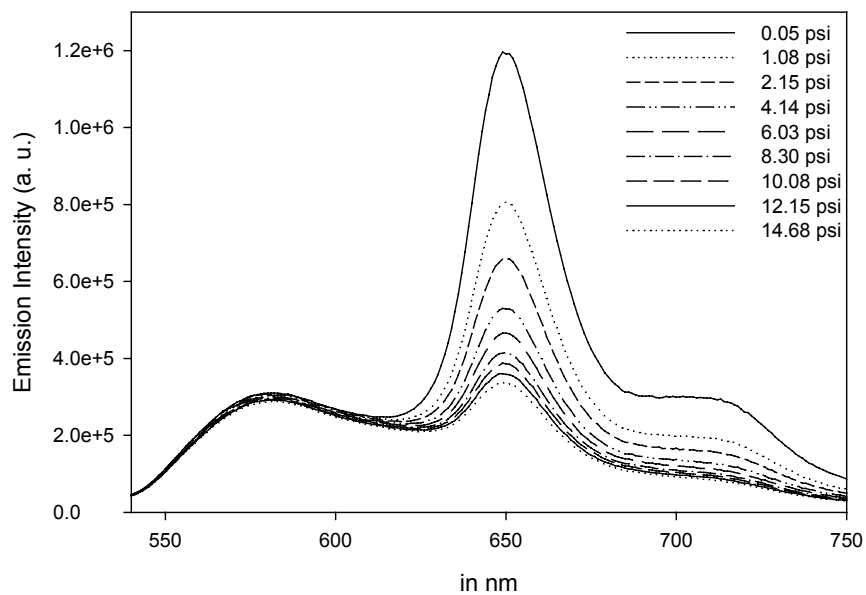


Figure 2-9: Pressure response of dual-luminophore PtTFPP-Ruphen/PAN in poly-t-BS-co-TFEM binder at 292.9 K. Excited at 465 nm.

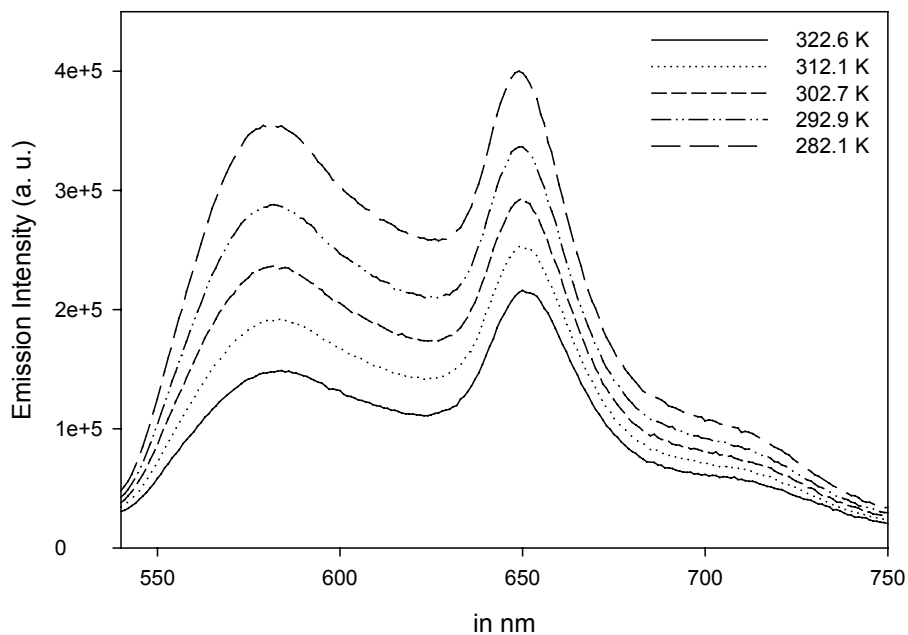


Figure 2-10: Temperature response of dual-luminophore PtTFPP-Ruphen/PAN in poly-t-BS-co-TFEM binder at 14.68 psi. Excited at 465 nm.

The quantitative pressure and temperature dependence of the two emission components is highlighted by the plots in Figure 2-11 and 2-12. First, Figure 2-11 illustrates the SV response of the emission components. This presentation shows that at all temperatures the Ruphen emission varies only slightly with pressure. The reason that the Ruphen emission is not strongly pressure dependent is that 1) the emission lifetime of the complex is relatively short (i.e.,  $< 1 \mu\text{s}$ )<sup>44</sup> and 2) the complex is encapsulated in PAN, which has a comparatively low gas permeability. By contrast, the emission of PtTFPP varies relatively strongly with air pressure. The SV plots show some curvature, and they vary with temperature. The temperature variation in the SV plots arises because of overlap of temperature dependencies in the emission of the Ruphen and PtTFPP luminophores. Note that the overall pressure response of the PtTPPP dye is less in the dual probe PSP compared to that observed for the same compound when it is dispersed alone in the poly-t-BS-co-TFEM binder (Figure 2-6).

This difference is believed to arise because of two factors: 1) in the dual probe PSP there is some spectral overlap between the emission from Ruphen and PtTFPP, and since the Ruphen emission is not strongly pressure dependent it decreases the effective pressure response in the 650 nm region where PtTFPP emits; 2) introducing nanospheres in the polymer matrix to some extent decreases diffusivity of oxygen through binder, using undoped PAN nanospheres in PtTFPP / poly-t-BS-co-TFEM coating caused 7-fold intensity change between vacuum and 14.7 psi where the same change was 11 fold for PtTFPP / poly-t-BS-co-TFEM coating.

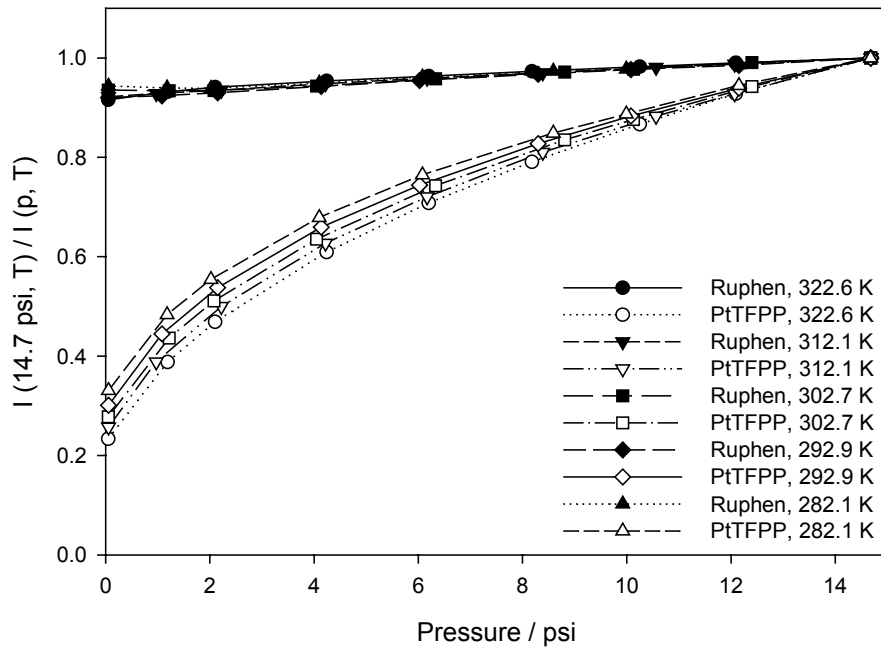


Figure 2-11: Stern-Volmer plots for dual-luminophore PtTFPP-Ruphen/PAN nanospheres in poly-t-BS-co-TFEM coating at various temperatures. Emission is integrated over an area of 635-670 nm for PtTFPP and 540-580 nm for Ruphen/PAN.

Figure 2-12 illustrates the temperature dependence of the emission intensity for the emission from the two probes at 14.7 psi. The effective temperature dependence of the Ruphen emission is  $\sim -1.4\% \cdot ^\circ\text{C}^{-1}$  whereas that of the PtTFPP is  $\sim -1.1\% \cdot ^\circ\text{C}^{-1}$ . Note that the temperature dependency of PtTFPP emission might be tailored by changing the concentrations of the dye used in the coating formulation. Using a higher concentration of PtTFPP (or lower amount of Ruphen/PAN) in dual-luminophore PSP formulation does not only decrease the temperature sensitivity of PtTFPP emission at 650 nm region but also reduces the overlap effect which causes downward curving of SV plot and diminishes the sensitivity in pressure estimation. However, in wind tunnel applications, it

is desired that both luminophores display similar magnitude of emission in order to have similar SNR from both emissions under similar illumination intensity.

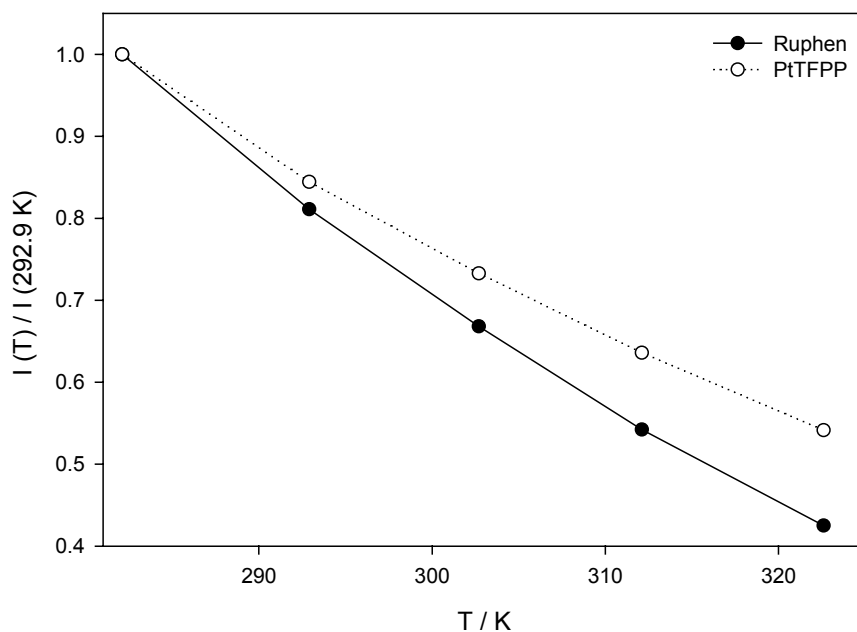


Figure 2-12: Temperature response of Ruphen/PAN and PtTFPP emissions at 14.68 psi. Emission is integrated over an area of 635-670 nm for PtTFPP and 540-580 nm for Ruphen/PAN.

Ruphen and PtTFPP emissions are very stable in the dual-luminophore PSP where only  $\sim 1\% \cdot \text{hr}^{-1}$  and  $\sim 0.5\% \cdot \text{hr}^{-1}$  decrease in their emissions are observed, respectively, under excitation light. Dual-luminophore PSP also showed similar spectroscopic changes to pressure and temperature several months after its preparation.

### **Self-Referencing PSP: PtTFPP-Rh110/PAN / Poly-t-BS-co-TFEM**

Self-referencing PSPs are utilized to solve image registration problems in PSP technology. As we summarized and explained the general issues regarding self-referencing PSPs in Chapter 1, we will only discuss our experimental findings for the self-referencing PSP developed in our lab. Dye encapsulation with PAN technique also opened up possibilities to co-precipitate other dyes in PAN nanospheres. In this context,

we searched for possible candidates for a reference sensor that can be incorporated in PAN nanospheres and after some trial-errors, we selected Rh110 as a temperature and pressure independent sensor for self-referencing PSP. Rh110 has a high quantum yield and short lifetime, and its emission ( $\lambda_{\max} = 521 \text{ nm}$ ) does not overlap with PtTFPP's emission ( $\lambda_{\max} = 651 \text{ nm}$ ). Furthermore, it can be co-precipitated with PAN nanospheres in a substantial amount. These properties of Rh110 make it ideal for a reference sensor. The preparation of self-referencing PSP is very similar to that of dual-luminophore PSP (see experimental section below). Figure 2-13 shows the pressure response of self-referencing PSP at constant temperature. As expected, Rh110 emission does not change with pressure as opposed to PtTFPP emission which varies strongly with air pressure.

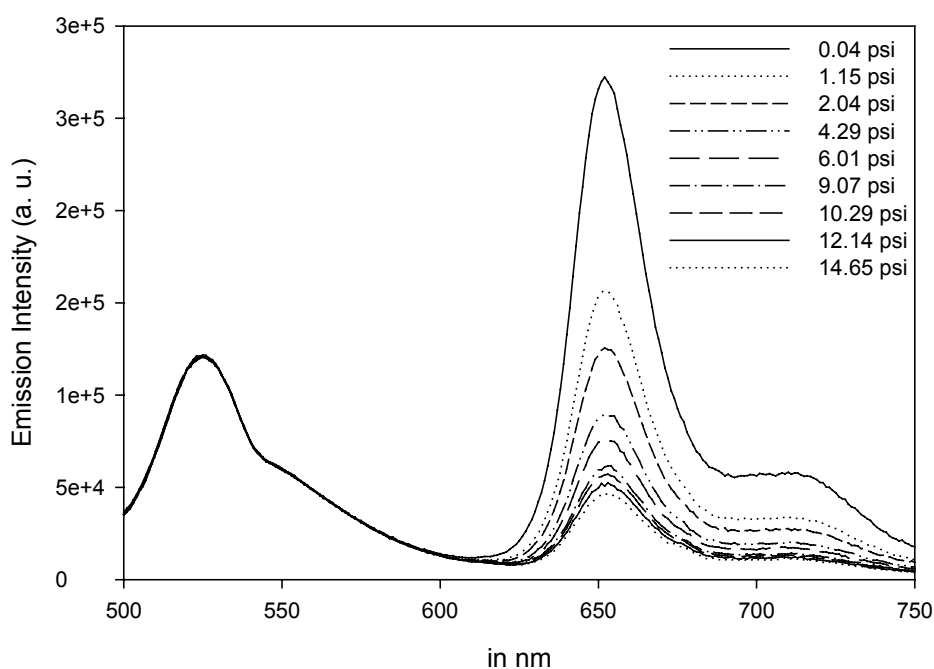


Figure 2-13: Pressure response of Rh110/PAN and PtTFPP emissions at 315.8 K. Emission is integrated over an area of 635-670 nm for PtTFPP and 500-540 nm for Rh110/PAN.

The variation of both emissions with pressure can be demonstrated quantitatively by using SV plots shown in Figure 2-14. The change in the emission intensity of Rh110 is negligible and can be assumed to be constant over 0 – 14.7 psi pressure range. SV plot of PtTFPP emission exhibits nonlinearity, especially in the low pressure region. The PtTFPP phosphorescence intensity decreases by 6-fold when going from vacuum to ambient pressure. This is less than the response observed for PtTFPP / poly-t-BS-co-TFEM coating (11 fold). This is probably due to decrease in diffusion of oxygen through the binder because of almost impermeable PAN nanospheres which fill the voids in polymer matrix.

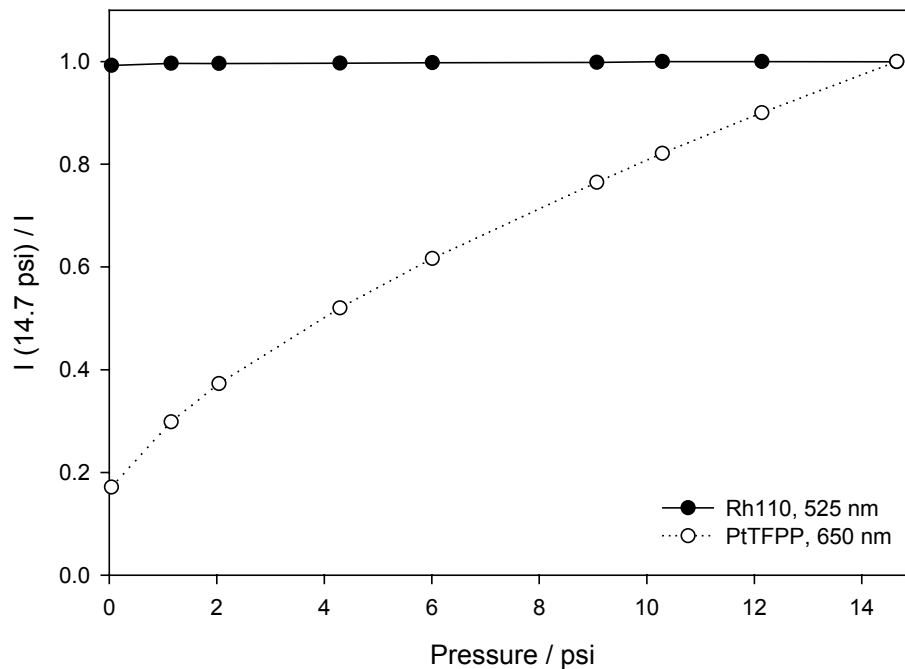


Figure 2-14: SV plots for pressure response of Rh110/PAN and PtTFPP emissions at 315.8 K. Emission is integrated over an area of 635-670 nm for PtTFPP and 500-540 nm for Rh110/PAN.

Self-referencing PSPs work by ratioing reference sensor intensity with pressure sensor intensity. If we apply this approach for PtTFPP-Rh110/PAN / poly-t-BS-co-TFEM coating, we get the following plot (Figure 2-15) for ratio versus pressure:

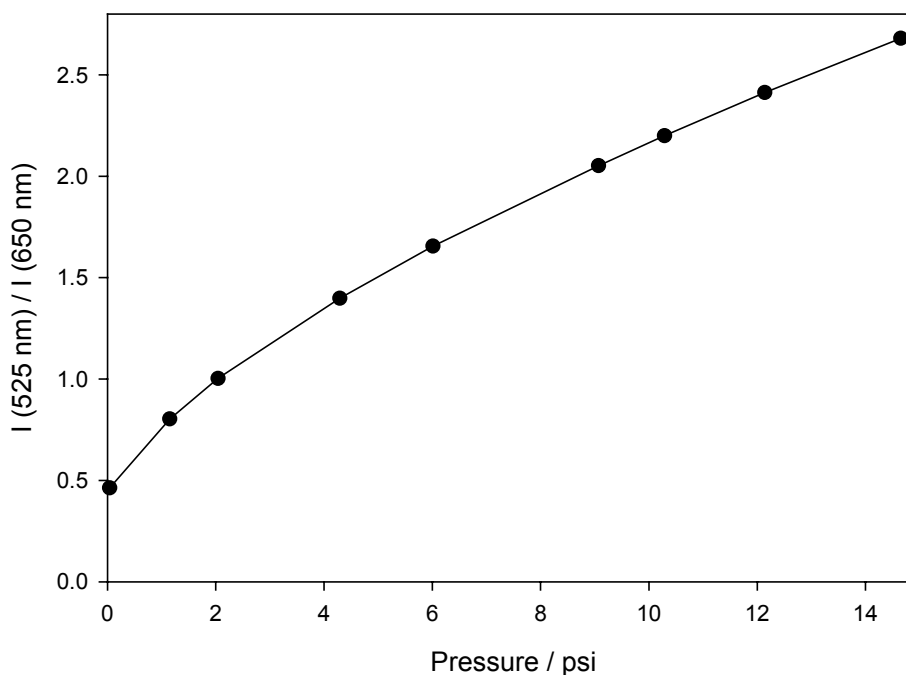


Figure 2-15: Pressure dependence of ratio  $I(525 \text{ nm}) / I(650 \text{ nm})$  in PtTFPP-Rh110/PAN / poly-t-BS-co-TFEM coating at 315.8 K. Emission is integrated over an area of 635-670 nm for PtTFPP and 500-540 nm for Rh110/PAN.

As it is anticipated, ratio plot is very similar to SV plot of PtTFPP response shown in Figure 2-14, the only difference is the scale in Figure 2-15, which depends on the relative intensities of the emissions collected with the fluorimeter. Note that self-referencing PSPs do not take account any temperature effect that might be observed throughout experiment. Temperature variations can lead to significant errors. Figure 2-16 shows the variation of ratio with temperature at constant pressure. The percent change in ratio is -0.63 per Celsius. The temperature dependence of PtTFPP / poly-t-BS-co-TFEM

coating is  $-0.53\% \cdot ^\circ\text{C}^{-1}$ . The increase in temperature dependency is believed due to the change in activation energy because of incorporation of nanospheres in the polymer binder which make oxygen diffusion slower with a higher activation barrier.

The self-referencing PSP developed here can be used in PSP applications where temperature fluctuations are minimal and/or other types of temperature correction methods are readily available (such as using infrared cameras or applying in situ calibration for data calibration).

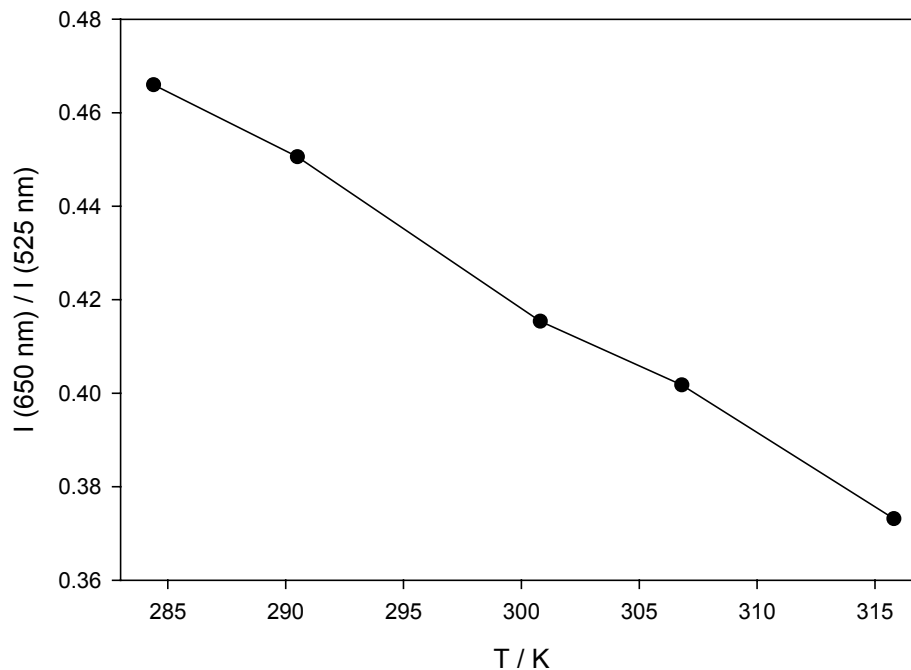


Figure 2-16: Temperature dependence of ratio  $I(525 \text{ nm}) / I(650 \text{ nm})$  in PtTFPP-Rh110/PAN / poly-t-BS-co-TFEM coating at 14.7 psi. Emission is integrated over an area of 635-670 nm for PtTFPP and 500-540 nm for Rh110/PAN.

### **Three-Component PSP: PtTFPP-Ruphen/PAN-Rh110/PAN / Poly-t-BS-co-TFEM**

Dual-luminophore PSP can be used for temperature correction whereas self-referencing PSP eliminates the image registration problem. However, neither of those PSPs are adequate for solving both image registration and temperature interference at the same time in wind tunnel experiments. Since we can compartmentalize dyes in PAN

nanospheres which limit interactions between luminophores, we envisioned a PSP that includes three dyes in the same matrix. Therefore, we dispersed Rh110/PAN and Ruphen/PAN along with PtTFPP in poly-t-BS-co-TFEM (three-component PSP, Figure 2-17). By doing so, we wanted to be able to measure pressure and temperature by internal referencing. Spectroscopic measurements revealed that three-component PSP could be used for this purpose.

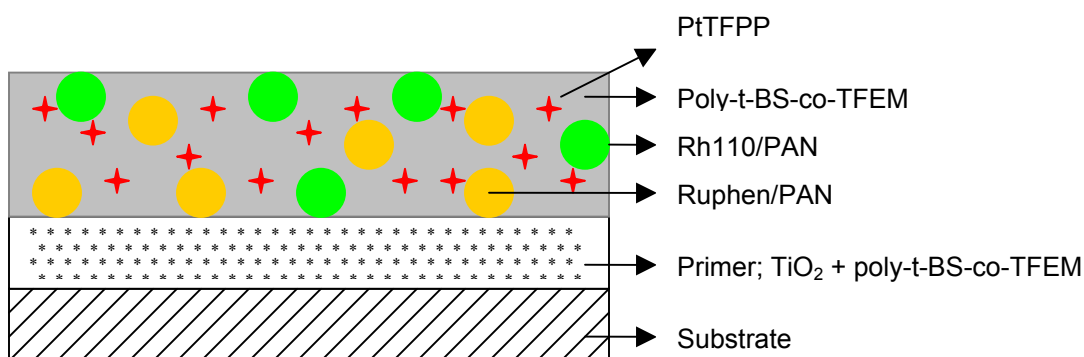


Figure 2-17: Elements of three-component PSP.

In this formulation, Rh110/PAN serves as reference, Ruphen/PAN is used for temperature correction, and PtTFPP is again used for pressure sensing. Figure 2-18 shows the pressure response of three-component PSP. The peak around at 525 nm belongs to Rh110, middle peak near 580 nm is Ruphen's emission peak, and 650 nm peak belongs to PtTFPP. Ruphen emission changes very little with air pressure whereas no change is observed for Rh110. PtTFPP emission varies strongly with pressure.

The luminophores used in three-component PSP are very stable against excitation light. Rh110, Ruphen, and PtTFPP emissions decreased ~1.5%, ~1%, ~1.5% per hour respectively under constant illumination. The coating has also excellent temporal stability, and can even be used many months after its preparation.

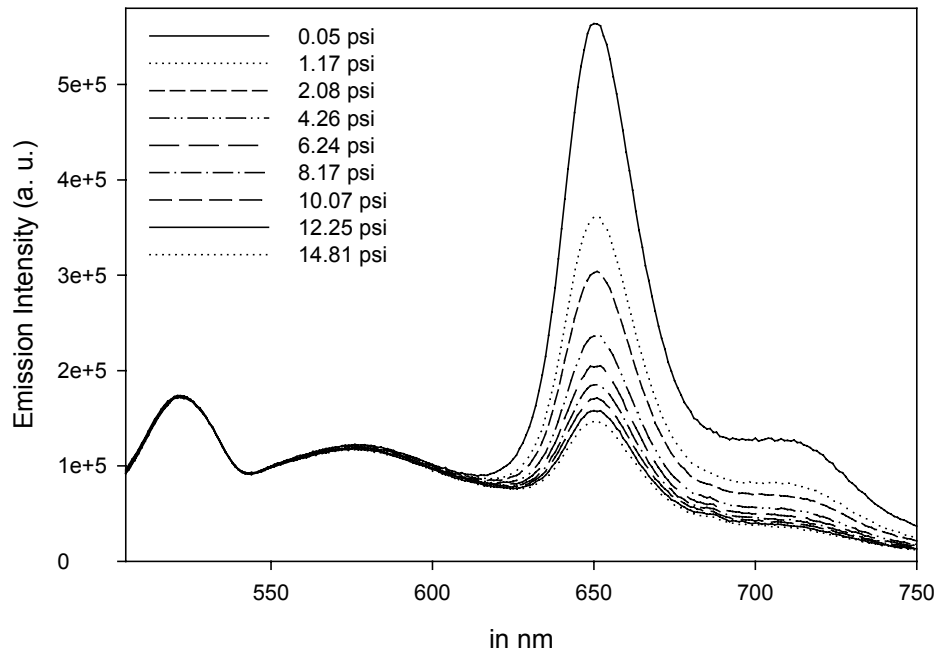


Figure 2-18: Pressure response of Rh110/PAN, Ruphen/PAN and PtTFPP emissions at 315.1 K. Emission is integrated over an area of 640-670 nm for PtTFPP, 550-580 nm for Ruphen/PAN, and 505-535 nm for Rh110/PAN.

Temperature response of coating at constant pressure is shown in Figure 2-19.

Ruphen and PtTFPP emission changes with temperature whereas very little variation with temperature is observed for Rh110. In reality, this small variation at 525 nm is not due to Rh110 emission itself, it is because of overlap of Ruphen emission with Rh110 emission and the extent of overlap slightly increases as temperature decreases which shows up as an intensity increase at 525 nm where Rh110 emits. This also reveals the importance of concentrations of the dyes used in the formulation to minimize these effects. The main issue in three-component PSP is that Ruphen emission overlaps with both Rh110 and PtTFPP emissions, which in turn decreases the sensitivity of the coating to pressure and temperature.

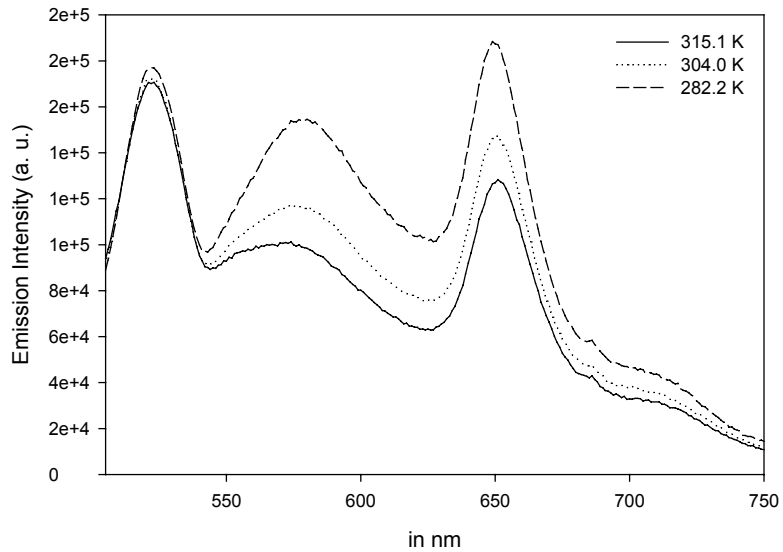


Figure 2-19: Temperature response of PtTFPP-Ruphen/PAN-Rh110/PAN / poly-t-BS-co-TFEM coating at 14.81 psi. Emission is integrated over an area of 640-670 nm for PtTFPP, 550-580 nm for Ruphen/PAN, and 505-535 nm for Rh110/PAN.

Ratio plots of Rh110 emission with PtTFPP emission at various temperatures yield nonlinear curves (Figure 2-20). Yet, the pressure sensitivity is adequate for PSP research.

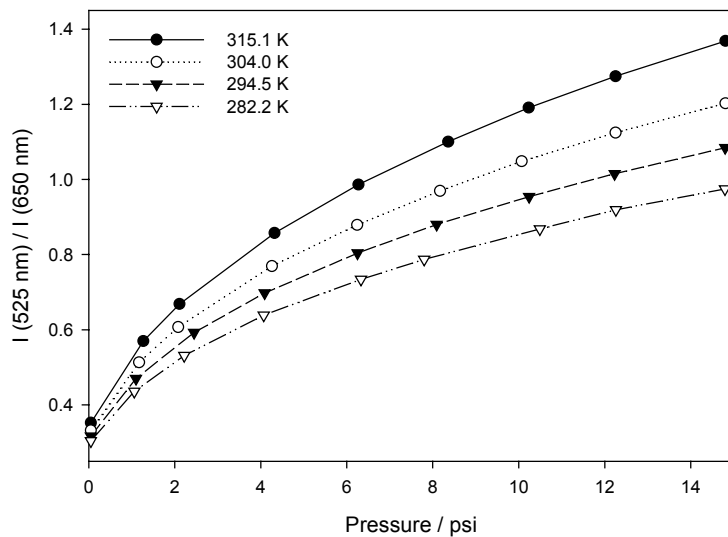


Figure 2-20: Pressure dependence of ratio  $I(525 \text{ nm}) / I(650 \text{ nm})$  in PtTFPP-Ruphen/PAN-Rh110/PAN / poly-t-BS-co-TFEM coating at various temperatures. Emission is integrated over an area of 640-670 nm for PtTFPP and of 505-535 nm for Rh110/PAN.

Similarly, ratio plots of Rh110 emission with Ruphen emission show high temperature dependence with a little pressure dependency (Figure 2-21). From these results, it can be concluded that by simply ratioing reference sensor emission with TSL and PSL emissions, one can eliminate the need for wind-off data. Moreover, the temperature correction is also possible where it can not be achieved with self-referencing PSPs.

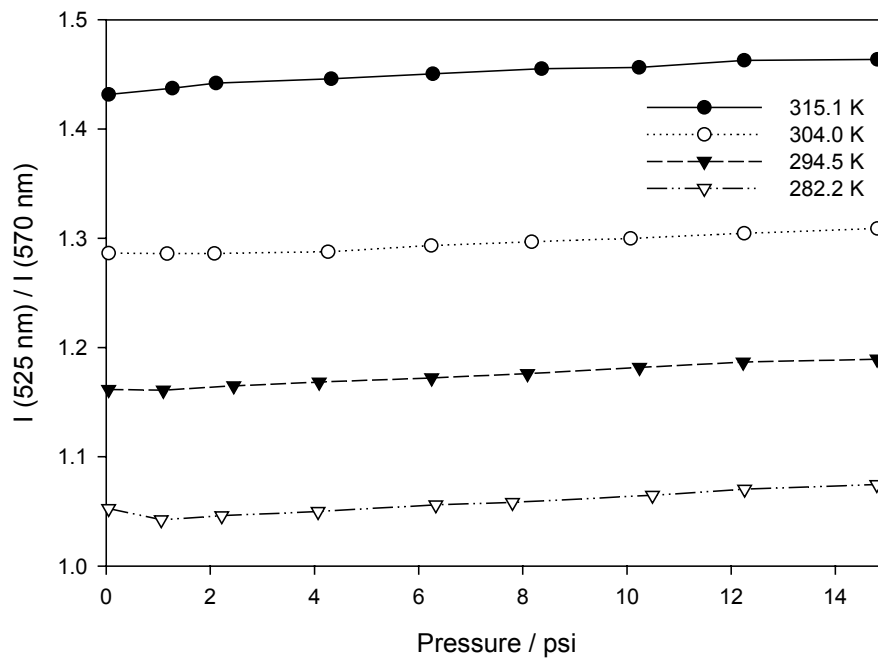


Figure 2-21: Temperature dependence of ratio  $I(525 \text{ nm}) / I(570 \text{ nm})$  in PtTFPP-Ruphen/PAN-Rh110/PAN / poly-t-BS-co-TFEM coating at various temperatures. Emission is integrated over an area of 550-580 nm for Ruphen/PAN, and of 505-535 nm for Rh110/PAN.

Figure 2-22 demonstrates the temperature dependence of ratios  $I(570 \text{ nm}) / I(525 \text{ nm})$  and  $I(650 \text{ nm}) / I(525 \text{ nm})$  at constant pressure. One can calculate the percent change of ratio values upon temperature; they are  $-0.81\% \cdot ^\circ\text{C}^{-1}$  for Ruphen/Rh110 ratio and  $-0.87\% \cdot ^\circ\text{C}^{-1}$  for PtTFPP/Rh110. These numbers are significantly different from the

ones that we reported for dual-luminophore PSP. There are several reasons for this: (1) Rh110 emission tails up to 580 nm and overlaps with Ruphen emission decreasing its sensitivity to temperature, (2) Ruphen emission also overlaps with PtTFPP emission and concentration of Ruphen/PAN in three-component PSP is different than the one used in dual-luminophore PSP, (3) the amount of nanospheres in three-component PSP is more than that of dual-luminophore PSP which is believed to be responsible for the changes in the activation energy of oxygen diffusion.

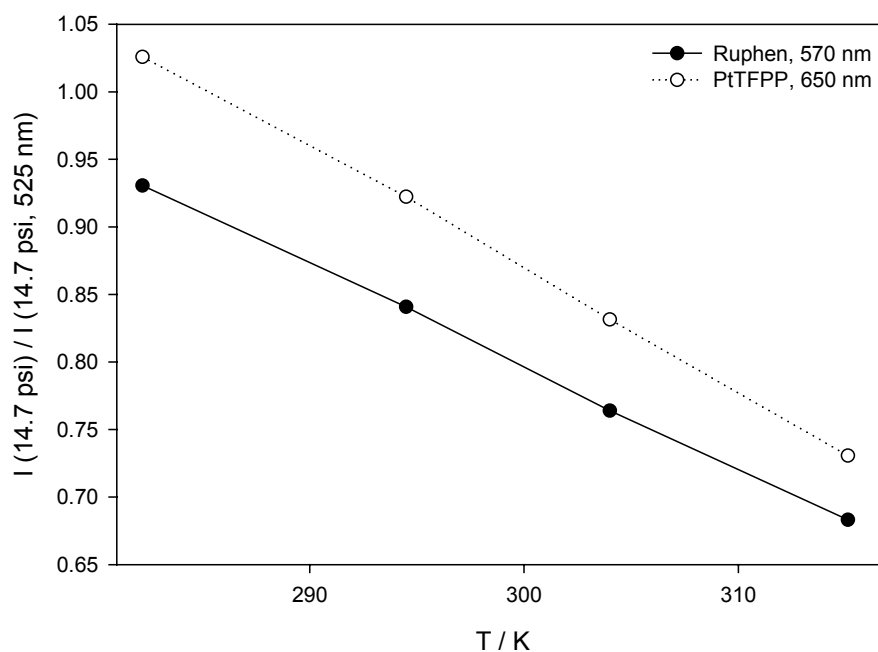


Figure 2-22: Temperature variation of  $I(570 \text{ nm}) / I(525 \text{ nm})$  and  $I(650 \text{ nm}) / I(525 \text{ nm})$  at 14.81 psi.

### Conclusions

We have developed novel one-component, dual-luminophore, self-referencing and three-component pressure sensitive paints. Three-component PSP has been realized for the first time for usage in PSP technology. Temperature and reference sensors are incorporated in PAN nanospheres with a simple procedure. This encapsulation technique

allowed us to formulate multi-luminophore PSP coatings. This procedure can also be exploited for encapsulation of other dyes. In this context, we successfully encapsulated several other rhodamine and cyanine dyes. However, we could not achieve to incorporate all of them in PAN matrix, a large fraction of these luminophores remained in water phase. Nonetheless, the dye incorporation procedure was reproducible.

One-component PSP displayed high pressure sensitivity with low temperature dependence. One can measure pressure and temperature simultaneously by using dual-luminophore PSP. Self-referencing and three-component PSPs can be utilized in PSP applications without using a reference image. The main drawback of dual-luminophore and three-component PSPs developed in this work is the emission overlaps of luminophores between each other, which decreases sensitivity of pressure and temperature response of the coatings. However, this problem can be solved by using advanced data calibration techniques such as principal component analysis which will be discussed in the following section in detail.

## **Experimental**

### **Chemicals**

5,10,15,20-tetrakis(pentafluorophenyl) porphyrin platinum(II) (PtTFPP) was purchased from Frontier Scientific. Tris(1,10-phenanthroline)ruthenium(II) dichloride (Ruphen), Rhodamine 110 (Rh110), 4-*tert*-butylstyrene (t-BS), 2,2'-azobisisobutyronitrile (AIBN), sodium dodecyl sulfate (SDS), and polyacrylonitrile (PAN) were purchased from Aldrich Chemicals. 2,2,2-Trifluoroethyl methacrylate (TFEM) was obtained from SynQuest Labs. (Alachua, FL). Titanium dioxide (Tronox CR-800) was purchased from Kerr-McGee Chemical Co. N,N,-Dimethylformamide

(anhydrous) was purchased from Acros. All other solvents were obtained from Fisher Scientific and used without purification.

### **Synthesis of Poly-t-BS-co-TFEM**

Poly-t-BS-co-TFEM was synthesized in one step from t-BS and TFEM (Figure 2-2). Inhibitors were removed from both monomers by passing through a column of activated basic aluminum oxide prior to polymerization. One molar equivalent of each monomer was dissolved in toluene (the amount of toluene used was 2 times the volume of the combined monomers). AIBN was then added to the toluene/monomer solution ( $\approx$  0.2% (wt) of AIBN relative to the total mass of the 2 monomers). The reaction mixture was heated at 70 °C for 20 hrs under a nitrogen atmosphere. After the mixture was cooled to room temperature, the polymer was precipitated into methanol. The crude polymer was then dissolved in toluene and precipitated again in methanol in order to remove unreacted monomer and low molecular weight oligomers. The resulting polymer was isolated as a white powder and it was dried under vacuum overnight to remove residual solvent. The ratio of t-BS and TFEM units in the copolymer was determined by using the molar absorption coefficient of the t-BS unit in THF at 264 nm. The composition was found to be 4:5 (t-BS:TFEM). GPC (THF, polystyrene standards):  $M_n = 108,600$ ,  $M_w = 389,000$ , PDI = 3.58. Poly-t-BS and poly-TFEM were synthesized in a similar fashion.

### **Synthesis of Dye Encapsulated Nanospheres**

Our approach to the preparation of polyacrylonitrile nanospheres in aqueous solution is based on the method described by Kürner et al.<sup>112</sup> Their method was modified so that it is possible to disperse the resulting particles in an organic solvent. The modified procedure is as follows: 120 mg of PAN was dissolved in 25 mL of N,N dimethylformamide (DMF). Ruphen (1.5 mg) was added to the PAN/DMF solution, and

the mixture was stirred vigorously. In a separate beaker 60 mg of SDS was dissolved in 125 mL of water and the solution was transferred into a burette. Then, the SDS/water solution was added dropwise into the stirred DMF/PAN/Ruphen solution. After an addition of approximately 7 mL of the aqueous SDS solution, the mixture became opalescent due to formation of nanoparticles. When the addition was complete, the solution was centrifuged and the yellow-colored residue was washed sequentially with 100 mL of water and 50 mL of acetone. The wash solutions were only in faintly yellow in color, which indicates that the amount of Ruphen trapped in the PAN particles was approximately equal to the original amount of complex used to prepare the particles. After washing the nanoparticles with acetone, the residue was transferred to a vial and some acetone was added until the total volume was 4 mL. The vial was tightly sealed in order to prevent evaporation of the acetone. The dispersion of Ruphen/PAN particles in this acetone solution is stable for at least one month.

Rh110 incorporated nanospheres were prepared by using the same procedure as Ruphen/PAN preparation. However, in Rh110/PAN synthesis, 3.0 mg of Rh110 was used instead of 1.5 mg of dye used in Ruphen/PAN synthesis. The nanospheres were washed with 15 ml of acetone, and upon washing with acetone some of the incorporated Rh110 leaked from spheres and dissolved in acetone phase. Therefore, the concentration of Rh110 in PAN nanospheres was less than actual concentration of Rh110 used at the beginning. Nonetheless, the synthesis of Rh110/PAN is reproducible if one follows the procedure described in here.

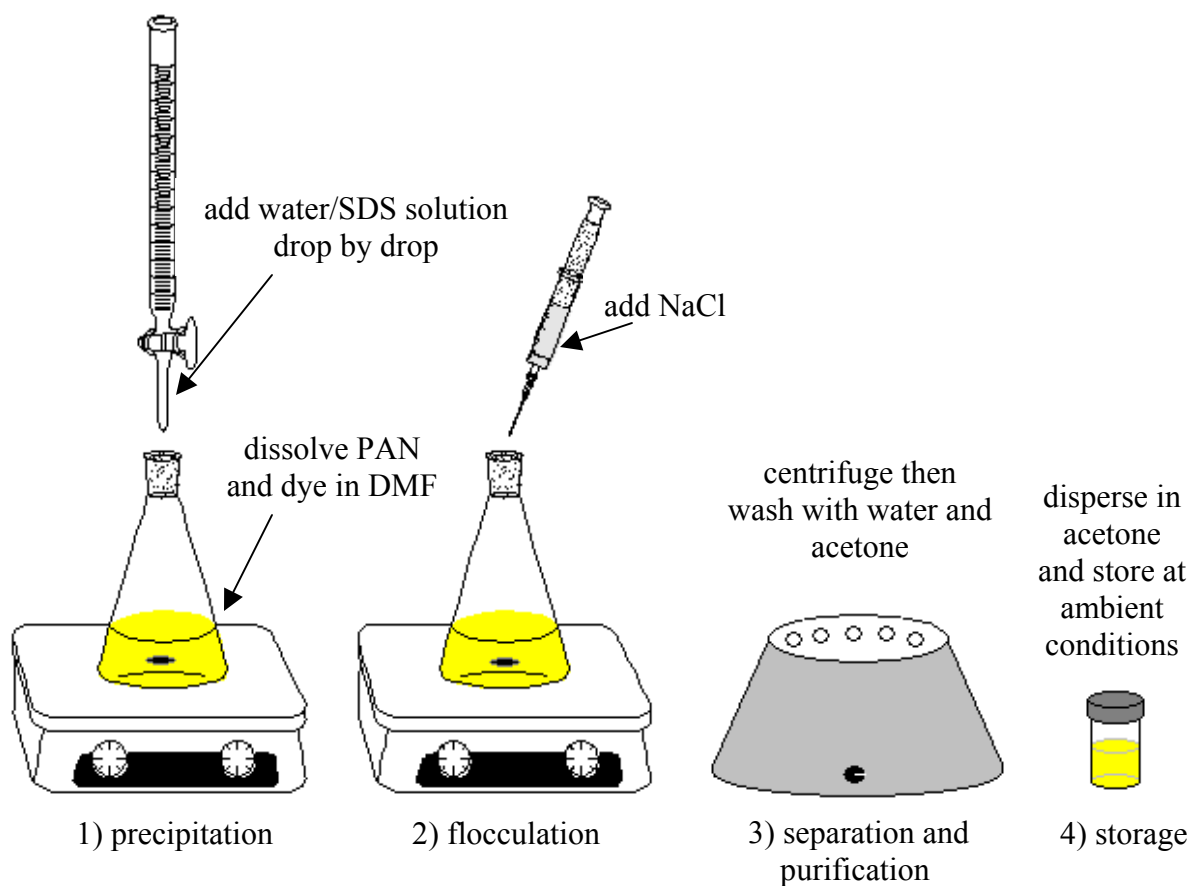


Figure 2-23: Synthesis scheme of dye incorporated nanospheres.

### Preparation of Coatings

In typical PSP applications a white primer or basecoat layer is applied to the substrate surface prior to application of the active PSP layer. The purpose of the primer layer is to provide optical uniformity and high reflectivity to the substrate surface. To prepare the primer, 100 mg of poly-t-BS-co-TFEM and 90 mg of titanium dioxide were dispersed in 3.5 ml of  $\text{CH}_2\text{Cl}_2$  and the resulting mixture was stirred overnight. The solution was then sprayed onto pre-cleaned glass slides and/or aluminum coupons with a commercially available airbrush gun (Paasche Airbrush Company), using air as a propellant (20 psi) and keeping the brush nozzle 10 cm from the surface. The basecoat was allowed to dry in an oven at 100 °C for 30 min before applying the PSP coat. To

prepare the PSP coating, 60 mg of poly-t-BS-co-TFEM, 0.2 mg of PtTFPP and 0.4 mL of the Ruphen/PAN acetone solution were mixed with 3 mL of CH<sub>2</sub>Cl<sub>2</sub>. The PSP coating was applied to the primed substrate by the same method used to apply the primer layer. It should be noted if the PSP coating is applied too rapidly, the resulting film may crack. The coated substrate was again dried at 100 °C for 30 min. The formulation described here is sufficient to coat a 6 in<sup>2</sup> area.

Above procedure is given for preparation of dual-luminophore PSP. Other PSPs were prepared by using exactly the same procedure except that the concentrations of the dyes were different. One component PSP utilizes 0.2 mg of PtTFPP in the same amount of poly-t-BS-co-TFEM used for dual-luminophore PSP. For self-referencing PSP formulation, 0.3 mL of Rh110/PAN acetone solution was mixed with 0.3 mg of PtTFPP. In three-component PSP, 0.4 mL of Rh110/PAN, 0.3 mL of Ruphen/PAN, and 0.2 mg of PtTFPP were mixed together.

### **Spectroscopic Measurements and Imaging**

Steady state emission studies were carried out on a commercially available fluorescence spectrophotometer (SPEX Industries, F-112A). The samples were excited at 465 nm. Temperature and pressure were controlled by placing the samples in a home-built chamber. The pressure was controlled with a vacuum pump and monitored with a vacuum gauge (model DPI 260, Druck). Temperature was controlled by a water recirculating bath (model RTE 140, Neslab) and was monitored by a thermocouple. The photoluminescence of the coatings was monitored front-face to the chamber window. Full field PSP luminescence images were collected with a thermoelectrically cooled 14-bit CCD camera. The samples were illuminated with a blue-LED array, and images were collected through 550/40 nm (03 FIV 044, from Melles Griot) bandpass filter.

The fluorescence microscope system consisted of an inverted microscope platform (Olympus, model IX 70) fitted with a 100 W Hg source (USH-102DH) and a CCD camera (Princeton, RTE 1300 X 1030) mounted on the side port. Fluorescence microscopy was carried out with a blue-violet modular filter cube (Chroma Technology, excitation 425 nm, 40 nm band-pass; emission 525 nm, 50 nm band-pass; 475 nm dichroic splitter). Fluorescence images were collected through 10X objective lenses (Olympus U Plan Fl, 0.30 NA and SLC Plan Fl, 0.55 NA, respectively). Neutral density filters and an IR blocking filter were used to adjust excitation intensity and prevent extraneous excitation light from reaching the CCD.

Secondary electron microscopy images were taken with a Hitachi S-4000 FE-SEM and the samples were sputter coated with Au-Pd (100 Angstroms). Steady state absorption spectra were obtained from a Varian Cary 100 dual-beam spectrophotometer.

## CHAPTER 3 APPLICATIONS OF MULTI-LUMINOPHORE COATINGS TO THE IMAGING

### **Introduction**

In recent years, pressure sensitive paints (PSPs) have gained a lot of popularity for measuring air pressure distributions over aerodynamic models.<sup>3,6,9</sup> PSPs use full field imaging systems to obtain surface pressure with very high resolution. They possess many advantages over conventional methods (such as pressure taps, which are installed at discrete locations on an aerodynamic model) in terms of cost, labor, and the amount of data collected.<sup>3</sup> One of the major drawbacks in PSP technology is the temperature dependency of PSP response.<sup>11,113</sup> When an aerodynamic test experiment is conducted in a wind tunnel, the temperature changes over the model throughout the experiment, so that PSP response becomes erroneous due to temperature variation. In order to correct the temperature interference on PSP response, the temperature surface distribution of the model should be measured at the same time with the pressure surface distribution. One way to achieve that is using a temperature sensitive luminophore (TSL) dispersed along with pressure sensitive luminophore (PSL) in the same polymer matrix, such systems are known as dual-luminophore PSPs.<sup>38,88,90</sup>

In the previous chapter, we described the development of novel multi-luminophore PSPs and presented their spectroscopic properties in PSP context. In dual-luminophore PSP formulation, we used Ru(phen)<sub>3</sub> (dichlorotris(1,10-phenanthroline)ruthenium(II)) as TSL, which was co-precipitated with polyacrylonitrile (PAN) nanospheres, and PtTFPP (platinum(II) meso-tetra(pentafluorophenyl)porphine) as PSL. Both of the luminophores

were dispersed in poly-t-BS-co-TFEM (poly-4-*tert*-butylstyrene-co-2,2,2-trifluoroethyl methacrylate) binder. Spectroscopic results indicated that Ruphen emission overlaps with PtTFPP emission which in turn decreases the sensitivity of dual coating response in pressure estimations. Three-component PSP utilizes Rh110 as reference signal which was also co-precipitated with PAN nanospheres.

In the present chapter, we demonstrate the imaging application of dual-luminophore PSP and three-component PSP to correct the temperature interference in pressure measurements. Two different calibration methods have been used to extract pressure and temperature information from dual-luminophore and three-component PSP data. One of the methods is a conventional ‘intensity-ratio method’ which utilizes the measurements taken at  $\lambda_{\max}$  (emission) of TSL and of PSL. The other one (principal component analysis<sup>114-123</sup> (PCA) approach) uses data collected by four different filters throughout the spectral region of TSL and of PSL. PCA approach is able to separate overlapped emissions, which in turn yields better approximations in pressure measurements. PCA has been applied to spectroscopic data sets before by our group,<sup>124,125</sup> however, this work is believed to be the first of its kind where PCA is applied to PSP imaging data. Both PCA and intensity-ratio data reduction techniques and statistical comparisons of the results obtained from the methods are discussed in detail throughout the text.

Most of the articles published regarding the dual-luminophore PSPs concentrate on the development of that type of paints. A similar work presented in here is published by Woodmansee et al. who compared different data reduction methods by applying a commonly used PSP to transverse jet-in crossflow experiment. They evaluated

isothermal, in-situ, k-fit, and temperature corrected pressure calibration results against pressure tap data.<sup>89</sup> The experimental setup used in this work closely resembles a-priori type calibration, yet, data reduction has been done by using two different mathematical methods: PCA and intensity-ratio method.

### Data Analysis Methods

#### Calibration Using Intensity-Ratios

In this method, two empirical expressions are used to fit the pressure (P) and temperature (T) for the known conditions to the emission intensity ratios ( $I_{ref}/I$ ) collected at two emission wavelengths corresponding to the emission from the TSL and PSL,<sup>3</sup>.

$$P = a_1 + b_1 \cdot X + c_1 \cdot Y + d_1 \cdot X \cdot Y + e_1 \cdot X^2 + f_1 \cdot Y^2 + g_1 \cdot X^2 \cdot Y + h_1 \cdot X \cdot Y^2 + i_1 \cdot X^2 \cdot Y^2 \quad (3-1)$$

$$T = a_2 + b_2 \cdot X + c_2 \cdot Y + d_2 \cdot X \cdot Y + e_2 \cdot X^2 + f_2 \cdot Y^2 + g_2 \cdot X^2 \cdot Y + h_2 \cdot X \cdot Y^2 + i_2 \cdot X^2 \cdot Y^2 \quad (3-2)$$

where  $X = I_{ref}^{TSL}(P_0, T_0) / I^{TSL}(P, T)$ ,  $Y = I_{ref}^{PSL}(P_0, T_0) / I^{PSL}(P, T)$  and the TSL and PSL superscripts refer to images obtained with the 550/40 nm and 650/10 nm filters, respectively, and  $I_{ref}(P_0, T_0)$  is the emission intensity collected with the coupon at the reference condition (P = 14.57 psi, isothermal coupon at T = 24.3 °C). The coefficients  $a_1$ - $i_1$  and  $a_2$ - $i_2$  are determined from a least squares fit of at least nine known pressure and temperature combinations. Nevertheless, we used 65 known pressure and temperature combinations in order to find these coefficients by using a regression routine available in SigmaPlot (SigmaPlot version 8.0, SPSS Inc.).

Although the Stern-Volmer relationship is mathematically pretty simple, we need to use higher order polynomials, such as equations (3-1) and (3-2) in order to fit the calibration points to represent the temperature and pressure responses of sensor data. This

is because oxygen responses of most of the pressure sensors exhibit non-linear variations in the intensity over large pressure ranges, which requires either two-site modeling<sup>30</sup> or at least second order polynomial fitting for PSP calibration points. In addition, there is some degree of “cross-talk” between the PSL and TSL dyes due to spectral overlap which significantly affect the linearity of sensor responses.

### Calibration Using Principal Component Analysis

Principal component analysis is an analysis technique that is used for reducing the matrices of data to their lowest dimensionality by the use of orthogonal factors space and transformations, which in turn results in predictions for recognizable factors.<sup>126</sup> In order for a data matrix to be factor analyzable, the data should be able to be modeled as a linear sum of product terms of the form:

$$d_{ik} = \sum_{j=1}^n r_{ij} c_{jk} \quad (3-3)$$

In equation (3-3),  $r_{ij}$  is the  $j$ th factor associated with row  $i$ , and  $c_{jk}$  is the  $j$ th factor associated with column  $k$ . We will refer  $r_{ij}$  as scores and  $c_{jk}$  as loadings. We may also write equation (3-3) in matrix multiplication form:

$$D = RC \quad (3-4)$$

where  $\mathbf{D}$  is the experimental data matrix,  $\mathbf{R}$  is called the scores matrix, and similarly  $\mathbf{C}$  is the loadings matrix. From a known matrix of  $\mathbf{D}$ , we aim to find  $\mathbf{R}$  and  $\mathbf{C}$  matrices that can reproduce the original data matrix as in equation (3-4). Initially, we decompose the data matrix into eigenvectors and eigenvalues. The first mathematical step is to find the covariance matrix, which is inherently a square matrix:

$$Z = D^T D \quad (3-5)$$

Then this matrix is diagonalized by finding a matrix  $\mathbf{Q}$  such that

$$Q^{-1}ZQ = [\lambda_j \delta_{jk}] \quad (3-6)$$

This step can be easily calculated by using an eigenvector solver, from which we can also get eigenvectors to the corresponding eigenvalues. Therefore, we can write the following equation:

$$Zq_j = \lambda_j q_j \quad (3-7)$$

where  $q_j$  is the  $j$ th column of  $\mathbf{Q}$ . Since these columns (also called eigenvectors) constitute a mutually orthonormal set, we can use the following relationship:

$$Q^{-1} = Q^T \quad (3-8)$$

By exploiting equation (3-8), one can show that:

$$R = DQ \quad (3-9)$$

and

$$C = Q^T \quad (3-10)$$

Using these two equations, the data matrix can be reproduced from  $\mathbf{R}$  and  $\mathbf{C}$ , which is called abstract reproduction. The procedure explained so far is a general scheme for abstract factor analysis.<sup>126</sup> However, in principal component analysis,  $\mathbf{R}$  and  $\mathbf{C}$  are found in a different manner. In this method, the eigenvectors are consecutively calculated so as to minimize the residual error in each step. Therefore, each successive eigenvector accounts for the largest variation in the data. When all the eigenvalues are calculated by using equation (3-6), the variation corresponding to largest eigenvalue and eigenvector is subtracted from covariance matrix as shown in the following equation:

$$R_1 = Z - \lambda_1 q_1 q_1^T \quad (3-11)$$

From this residual matrix, the second principal eigenvector and its associated eigenvalue are calculated.

$$R_1 q_2 = \lambda_2 q_2 \quad (3-12)$$

To obtain the third eigenvector, we define  $\mathbf{R}_2$  as:

$$R_2 = Z - \lambda_1 q_1 q_1^T - \lambda_2 q_2 q_2^T \quad (3-13)$$

When one continues in this fashion, the remaining eigenvectors and eigenvalues are extracted in succession.<sup>126</sup>

### Target Transformation

As we pointed out in previous section, the  $\mathbf{R}$  and  $\mathbf{C}$  matrices constitute an abstract solution. Although they have mathematical meaning, they do not have any physical or chemical meanings in their present form. Target transformation helps one to obtain the meaningful factors, which can be recognized as physical or chemical factors. This is achieved by a transformation matrix, which can be combined with equation (3-14) as below:

$$D \cong D'' = (RT)(T^{-1}C) \quad (3-14)$$

Transformation matrix,  $\mathbf{T}$  is an  $n \times n$  square matrix, where  $n$  is the number of important factors determined by PCA. Transformation matrix has the following form for a data matrix which can be described with two principal factors:

$$T = \begin{bmatrix} a \cdot \cos(\theta) & -b \cdot \sin(\theta) \\ c \cdot \sin(\theta) & d \cdot \cos(\theta) \end{bmatrix} \quad (3-15)$$

If the transformation is orthogonal (preserving the angles between factor axes), then  $a$ ,  $b$ ,  $c$ , and  $d$  constants are equal to 1. However, if the transformation is non-orthogonal,

then these constants should be determined by taking account the prior information about the real factors.<sup>124,126</sup>

### Factor Analyzability

In order for a data set to be factor analyzable it should be possible to represent the data in matrix form as shown in equation (3-3). Here, we demonstrate that dual-luminophore PSP data fit this criterion. The dual-luminophore PSP data consist of emission intensities obtained from temperature sensitive and pressure sensitive luminophore for various pressure-temperature conditions obtained by using a fluorescence spectrometer or a CCD imager fitted with bandpass filters. The absolute intensity obtained in any luminescence measurement depends on many factors. The observed emission intensity can be described as:

$$I_{obs}(\lambda_{em}) = AN_{dye}\phi_{dye}F(\lambda_{em}) \quad (3-16)$$

In equation (3-16), A is a constant which is affected by many factors; such as the light intensity impinging on the sample, the efficiency of photodetector, the efficiency of the support electronics, and so on.  $N_{dye}$  is the number of excited state dye molecules,  $\Phi_{dye}$  is the quantum yield for emission, and  $F(\lambda_{em})$  is the emission intensity distribution function (i.e., the spectral bandshape of fluorescence and/or phosphorescence emission). Ideally, in PSP experiments, everything but pressure and temperature are constant. Therefore, any change in pressure and/or temperature will change  $\Phi_{dye}$ . Hence, equation (3-16) can be re-cast as follows:

$$I_{obs} = A'\phi_{dye}F(\lambda_{em}), \text{ where } A' = AN_{dye} \quad (3-17)$$

Consider a situation in which two dyes contribute to the total emission intensity at a given wavelength (e.g., a TSL and PSL). Then, the above equation becomes:

$$I_{obs}(P, T, \lambda) = A_{TSL}' \phi_{TSL}(P, T) F_{TSL}(\lambda_{em}) + A_{PSL}' \phi_{PSL}(P, T) F_{PSL}(\lambda_{em}) \quad (3-18)$$

In general, TSLs display little or no pressure sensitivity. Incorporating the constants with  $F(\lambda_{em})$ , one obtains:

$$I_{obs}(P, T, \lambda) = \phi_{TSL}(T) F_{TSL}(\lambda_{em})' + \phi_{PSL}(P, T) F_{PSL}(\lambda_{em})' \quad (3-19)$$

where  $F_{TSL}(\lambda_{em})' = A_{TSL}' F_{TSL}(\lambda_{em})$  and  $F_{PSL}(\lambda_{em})' = A_{PSL}' F_{PSL}(\lambda_{em})$ . Note that equation (3-19) is very similar in nature to equation (3-3) with  $n$  being 2. With this theoretical background, we can now seek  $\mathbf{R}$  and  $\mathbf{C}$  matrices that will explain the physical phenomena as in equation (3-19).

$$I_{obs}(P, T, \lambda) = R_1(\lambda) C_1 + R_2(\lambda) C_2 \quad (3-20)$$

In here,  $\mathbf{R}_1(\lambda) = F_{PSL}(\lambda_{em})'$ ,  $\mathbf{R}_2(\lambda) = F_{TSL}(\lambda_{em})'$ ,  $\mathbf{C}_1 = \Phi_{PSL}(P, T)$ , and  $\mathbf{C}_2 = \Phi_{TSL}(T)$ . By using this information, we can search for a transformation matrix that will give us the spectral shape of each luminophore once we calculate abstract factors. However, it has been argued that finding such a matrix is not easily accomplished in most systems.<sup>125</sup> Indeed, in the course of this work we had difficulties in determining such a transformation matrix for our spectroscopic data matrix,  $\mathbf{D}$ . In addition, a transformation which seeks to separate the spectra of the individual dyes does not necessarily lead to an optimal solution to separate the pressure and temperature response of a dual-luminophore PSP. Since the emission quantum yields of the TSL and PSL are dependent on temperature, we can alternatively seek a transformation matrix that will afford matrices that separate the temperature and pressure response of the coating, e.g.,  $\mathbf{R}_1(P)$ ,  $\mathbf{C}_1(P)$ ,  $\mathbf{R}_2(T)$ , and  $\mathbf{C}_2(T)$  matrices. Note that this condition is met only when temperature responses of both TSL and PSL are similar, and the temperature response of PSL is independent of pressure (i.e., an 'ideal' PSP).<sup>12</sup>

Fortunately, the temperature response of PtTFPP in poly-t-BS-co-TFEM polymer binder is independent of pressure, displaying ideal behavior. However, the temperature response of Ruphen/PAN nanospheres ( $\sim -1.42\% \cdot ^\circ\text{C}^{-1}$ ) is very different than that of PtTFPP ( $-0.53\% \cdot ^\circ\text{C}^{-1}$ ) in this binder. Thus, as shown below, PCA analysis of the spectral data for the dual-luminophore PSP used in the present work does not allow us resolve two important eigenvectors, where one is purely dependent on temperature and the other one is purely dependent on pressure. On the other hand, it is possible to optimize the target transformation so that one eigenvector expresses mainly the pressure dependence of the dual luminophore data, with a small temperature dependence,  $\mathbf{C}_1(\text{P}, \sigma\text{T})$ , whereas the second expresses most of the temperature dependence, with a small pressure dependence,  $\mathbf{C}_2(\text{T}, \sigma\text{P})$ .

Experimental data obtained on the PtTFPP-Ruphen/PAN / poly-t-BS-co-TFEM sensor using a fluorescence spectrometer (spectroscopic data set) and a CCD camera equipped with bandpass filters was subjected to the PCA analysis outlined above by using two different macros written using Matlab (version 6.1.0, release 12.1, MathWorks, Inc.). One macro applies PCA analysis to spectroscopic data comprising a  $261 \times 40$  matrix ( $\mathbf{D}_{261 \times 40}$ , 261 wavelengths and 40 P/T conditions), while the second executes the same algorithm for CCD image data comprising a  $4 \times 65$  matrix ( $\mathbf{D}_{4 \times 65}$ , 4 wavelengths and 65 P/T conditions). More detailed information is given below concerning the methods used, and the Matlab macros are available in Appendix A (application of PCA to a small size hypothetical data is also given in Appendix B for tutorial purposes). The coefficients resolved from the PCA analysis ( $\mathbf{C}_1(\text{P}, \sigma\text{T})$  and  $\mathbf{C}_2(\text{T}, \sigma\text{P})$ ) were used to fit

pressure and temperature according to the equations (3-1) and (3-2) by using least-squares regression analysis in SigmaPlot.

## **Results and Discussion**

We applied PCA method and intensity-ratio method to both spectroscopic and CCD camera set data of dual-luminophore and three-component PSPs. The results are discussed in the sections below.

### **Calibration Results for Dual-Luminophore PSP**

#### **PCA Calibration for Spectroscopic Data Set**

In order to develop an understanding of the method, PCA was initially carried out on a spectroscopic data set. Thus, emission spectra were collected with a fluorescence spectrometer using the PtTFPP-Ruphen/PAN / poly-t-BS-co-TFEM dual-luminophore coating at the 40 different P-T combinations listed in Table 3-1. These data were collected by equilibrating the dual-luminophore PSP coated coupon at a given temperature, and then emission spectra were obtained at seven different pressures. (In this series of experiments the seven pressure values used at the different temperatures are not identical—there are slight mismatches because the pressure was established by manual control of a pressure valve.) The set of 40 emission spectra for the pressure/temperature conditions are displayed in Figure 3-1. The emission maximum ( $\lambda_{\max}$ ) for PtTFPP is  $\approx 650$  nm, whereas Ruphen exhibits a broad emission, with  $\lambda_{\max} \approx 580$  nm, however the red side of the emission band overlaps the PtTFPP emission.

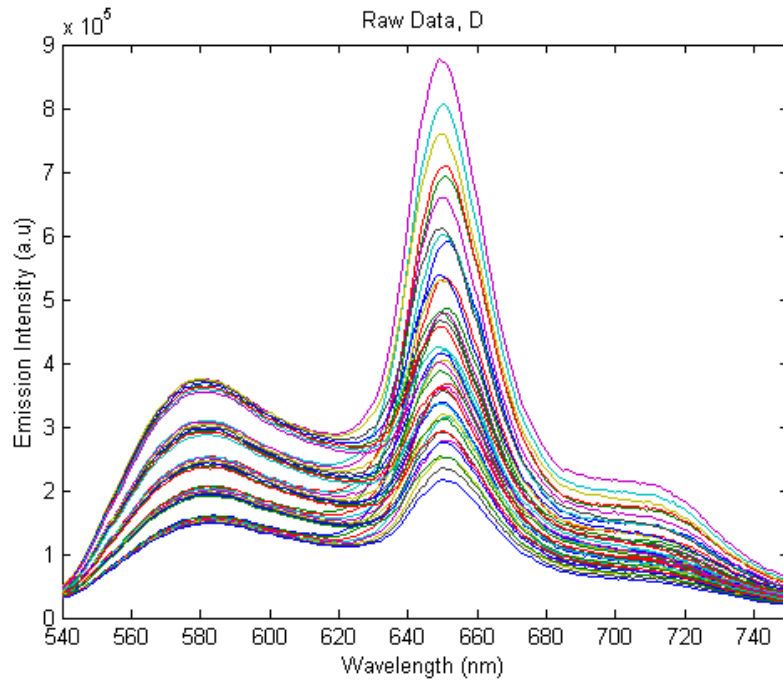


Figure 3-1: Emission intensity spectra of dual-luminophore PSP at various pressure-temperature combinations listed in Table 3-1. Excitation wavelength: 465 nm.

Table 3-1: Conditions and their corresponding C matrix elements.

Environmental Conditions		C <sup>T</sup> matrix elements	
Temperature (K)	Pressure (psi)		
322.6	1.19	C <sub>1,1</sub>	C <sub>2,1</sub>
322.6	2.10	C <sub>1,2</sub>	C <sub>2,2</sub>
322.6	4.24	C <sub>1,3</sub>	C <sub>2,3</sub>
322.6	6.20	C <sub>1,4</sub>	C <sub>2,4</sub>
322.6	8.18	C <sub>1,5</sub>	C <sub>2,5</sub>
322.6	10.25	C <sub>1,6</sub>	C <sub>2,6</sub>
322.6	12.09	C <sub>1,7</sub>	C <sub>2,7</sub>
322.6	14.69	C <sub>1,8</sub>	C <sub>2,8</sub>
312.1	0.97	C <sub>1,9</sub>	C <sub>2,9</sub>
312.1	2.22	C <sub>1,10</sub>	C <sub>2,10</sub>
312.1	4.22	C <sub>1,11</sub>	C <sub>2,11</sub>
312.1	6.17	C <sub>1,12</sub>	C <sub>2,12</sub>
312.1	8.39	C <sub>1,13</sub>	C <sub>2,13</sub>
312.1	10.56	C <sub>1,14</sub>	C <sub>2,14</sub>
312.1	12.07	C <sub>1,15</sub>	C <sub>2,15</sub>
312.1	14.69	C <sub>1,16</sub>	C <sub>2,16</sub>
302.7	1.22	C <sub>1,17</sub>	C <sub>2,17</sub>
302.7	2.08	C <sub>1,18</sub>	C <sub>2,18</sub>
302.7	4.05	C <sub>1,19</sub>	C <sub>2,19</sub>
302.7	6.33	C <sub>1,20</sub>	C <sub>2,20</sub>
302.7	8.81	C <sub>1,21</sub>	C <sub>2,21</sub>
302.7	10.13	C <sub>1,22</sub>	C <sub>2,22</sub>
302.7	12.40	C <sub>1,23</sub>	C <sub>2,23</sub>
302.7	14.68	C <sub>1,24</sub>	C <sub>2,24</sub>
292.9	1.08	C <sub>1,25</sub>	C <sub>2,25</sub>
292.9	2.15	C <sub>1,26</sub>	C <sub>2,26</sub>
292.9	4.14	C <sub>1,27</sub>	C <sub>2,27</sub>
292.9	6.03	C <sub>1,28</sub>	C <sub>2,28</sub>
292.9	8.30	C <sub>1,29</sub>	C <sub>2,29</sub>
292.9	10.08	C <sub>1,30</sub>	C <sub>2,30</sub>
292.9	12.15	C <sub>1,31</sub>	C <sub>2,31</sub>
292.9	14.68	C <sub>1,32</sub>	C <sub>2,32</sub>
282.1	1.18	C <sub>1,33</sub>	C <sub>2,33</sub>
282.1	2.02	C <sub>1,34</sub>	C <sub>2,34</sub>
282.1	4.10	C <sub>1,35</sub>	C <sub>2,35</sub>
282.1	6.08	C <sub>1,36</sub>	C <sub>2,36</sub>
282.1	8.59	C <sub>1,37</sub>	C <sub>2,37</sub>
282.1	9.99	C <sub>1,38</sub>	C <sub>2,38</sub>
282.1	12.15	C <sub>1,39</sub>	C <sub>2,39</sub>
282.1	14.68	C <sub>1,40</sub>	C <sub>2,40</sub>

The PCA algorithm was applied to the spectroscopic data,  $\mathbf{D}_{261 \times 40}$  (i.e., the experimental data in Figure 3-1). The analysis produced two significant eigenvalues (out of a total of 40), which account for 99.91% of the variation in the raw data,  $\mathbf{D}$ . As pointed out above, the initial PCA produces abstract factors that do not have physical significance. For example, one of the abstract eigenvectors features negative amplitude. Subsequent to the PCA, a non-orthogonal transformation matrix (equation (3-21)) was applied for rotation of the abstract eigenvectors  $\mathbf{C}_1$  and  $\mathbf{C}_2$ . The coefficients and  $\theta$  in the transformation matrix were determined semi-empirically based on the facts that (1) one of the eigenvectors should be mostly pressure dependent, while the other should be mostly temperature dependent, (2) there can not be any negative emission in the spectra, and (3) one of the eigenvector elements should be able to be grouped in 5 different sets, element values within each set displaying similar number. The final constraint arises because of the manner in which the spectral data were obtained, i.e., five temperatures and seven pressures (see Table 3-1). Thus, if one of the eigenvectors represents temperature variation, the corresponding elements of this temperature eigenvector should be similar in value for the same temperature, i.e.,  $C_{2,1} \cong C_{2,2} \cong C_{2,3} \cong C_{2,4} \cong C_{2,5} \cong C_{2,6} \cong C_{2,7} \cong C_{2,8}$  and  $C_{2,9} \cong C_{2,10} \cong C_{2,11} \cong C_{2,12} \cong C_{2,13} \cong C_{2,14} \cong C_{2,15} \cong C_{2,16}$ , and so on. With these guidelines, the transformation matrix shown in equation (3-21) was generated. It is important to note that many attempts of finding orthogonal transformation matrix did not yield factors that meet the requirements mentioned above.

$$T = \begin{bmatrix} 0.11 \cdot \cos(343.8) & -0.12 \cdot \sin(343.8) \\ 0.54 \cdot \sin(343.8) & 0.24 \cdot \cos(343.8) \end{bmatrix} \quad (3-21)$$

Multiplication of abstract  $\mathbf{R}$  matrix with equation (3-21) (non-orthogonal transformation matrix) affords the row matrices  $\mathbf{R}_1$  (blue line) and  $\mathbf{R}_2$  (green line) displayed in Figure 3-2.  $\mathbf{R}_1$  represents the fundamental spectrum (score matrix for the first eigenvector) for eigenvector  $\mathbf{C}_1(\text{P}, \sigma\text{T})$  (the pressure eigenvector), whereas  $\mathbf{R}_2$  represents the fundamental spectrum (score matrix for the second eigenvector) for eigenvector  $\mathbf{C}_2(\text{T}, \sigma\text{P})$  (the temperature eigenvector). Note that  $\mathbf{R}_1$  is similar in bandshape to the phosphorescence spectrum of PtTFPP in poly-t-BS-co-TFEM binder (see Chapter 2). This is consistent with the fact that the PtTFPP component dominates the pressure dependence of the dual-luminophore PSP emission. Note that there is some intensity at  $\approx 590$  nm in  $\mathbf{R}_1$  which arises due to the (weak) pressure dependence of the Ruphen emission. Row matrix  $\mathbf{R}_2$  features two peaks, one at  $\approx 580$  nm and a second at  $\approx 650$  nm. The shape of  $\mathbf{R}_2$  is consistent with the fact that the emission from both luminophores is temperature dependent.

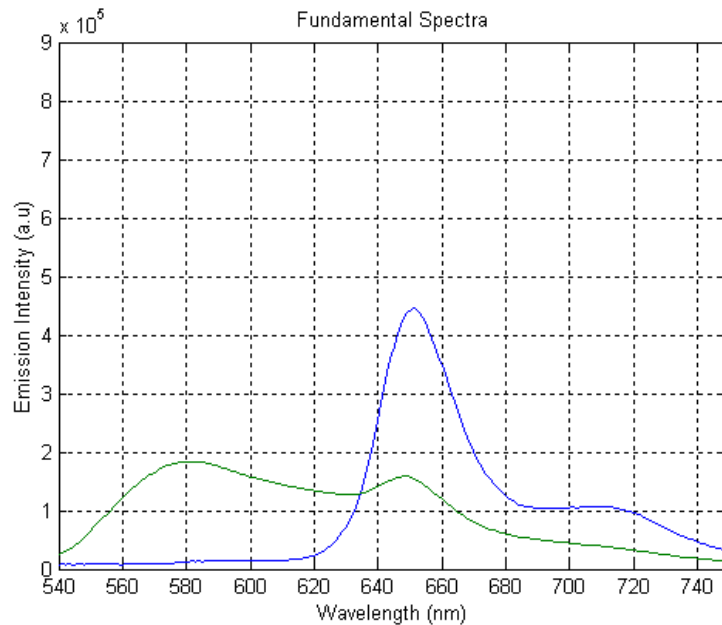


Figure 3-2: Fundamental spectra (row matrices,  $\mathbf{R}$ ) for two largest eigenvalues.

Figure 3-3A and 3-3B show the fractional total contribution of first and second eigenvectors to the reconstructed data matrix,  $\mathbf{D}''$  (Figure 3-3C) for the conditions given in Table 3-1, respectively. As noted above, the pressure conditions for each of the temperatures differed slightly, and consequently, it is difficult to discern from Figure 3-3A that  $C_1$  varies with pressure, but it is relatively temperature independent. On the other hand, it is easy to see from Figure 3-3B that  $C_2$  varies with temperature, but it is only slightly pressure dependent (i.e., the spectra are grouped into five sets, each set corresponding to a given temperature condition). Hence, the results indicate that the target transformation successfully resolves most of the pressure and temperature variation of the total emission from the dual-luminophore PSP by using two factors.

Even though the separation is not perfect ( $C_1$  is still slightly temperature dependent whereas  $C_2$  is slightly pressure dependent), the PCA method leads to improved accuracy for both temperature and pressure estimation. This conclusion is supported by comparing the pressure response (at constant temperature) of the raw emission intensity ratio from the PtTFPP PSL ( $I_{14.7 \text{ psi}}/I$ , obtained at 650 nm, Figure 3-4A) with the pressure response of  $1/C_1$  (Figure 3-4B). This comparison clearly shows that the pressure eigenvector ( $C_1$ ) is much more strongly pressure dependent than the raw emission intensity ratio. Specifically, over the 1 – 14.7 psi range, the raw intensity ratio varies by a factor of 2.2, while  $1/C_1$  varies by a factor of 5.2. Moreover, the PCA method also eliminates the small pressure response of the Ruphen/PAN emission. As can be seen in Figure 3-4A (filled circles), the raw emission intensity for the Ruphen component of the dual-luminophore PSP (monitored at 580 nm) varies approximately 10% over the 1 - 14.7 psi range, whereas the temperature eigenvector ( $C_2$ , Figure 3-4B) is virtually pressure independent.

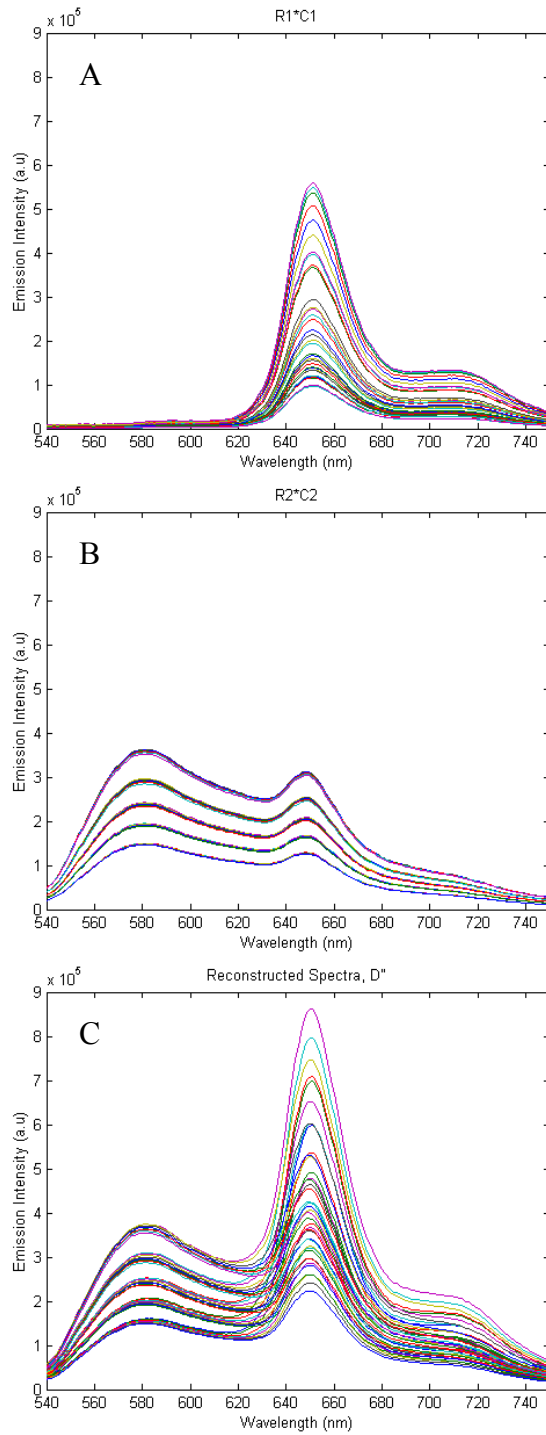


Figure 3-3: Fundamental and reconstructed spectra. A) The contribution of first fundamental spectrum ( $\mathbf{R}_1$ ) to total emission at various pressure-temperature combinations. B) The contribution of second fundamental spectrum ( $\mathbf{R}_2$ ) to total emission at various pressure-temperature combinations. C) The reconstructed spectra  $\mathbf{D}'' = \mathbf{R}_1\mathbf{C}_1 + \mathbf{R}_2\mathbf{C}_2$ , which are obtained by combining the total contributions from two largest eigenvalues.

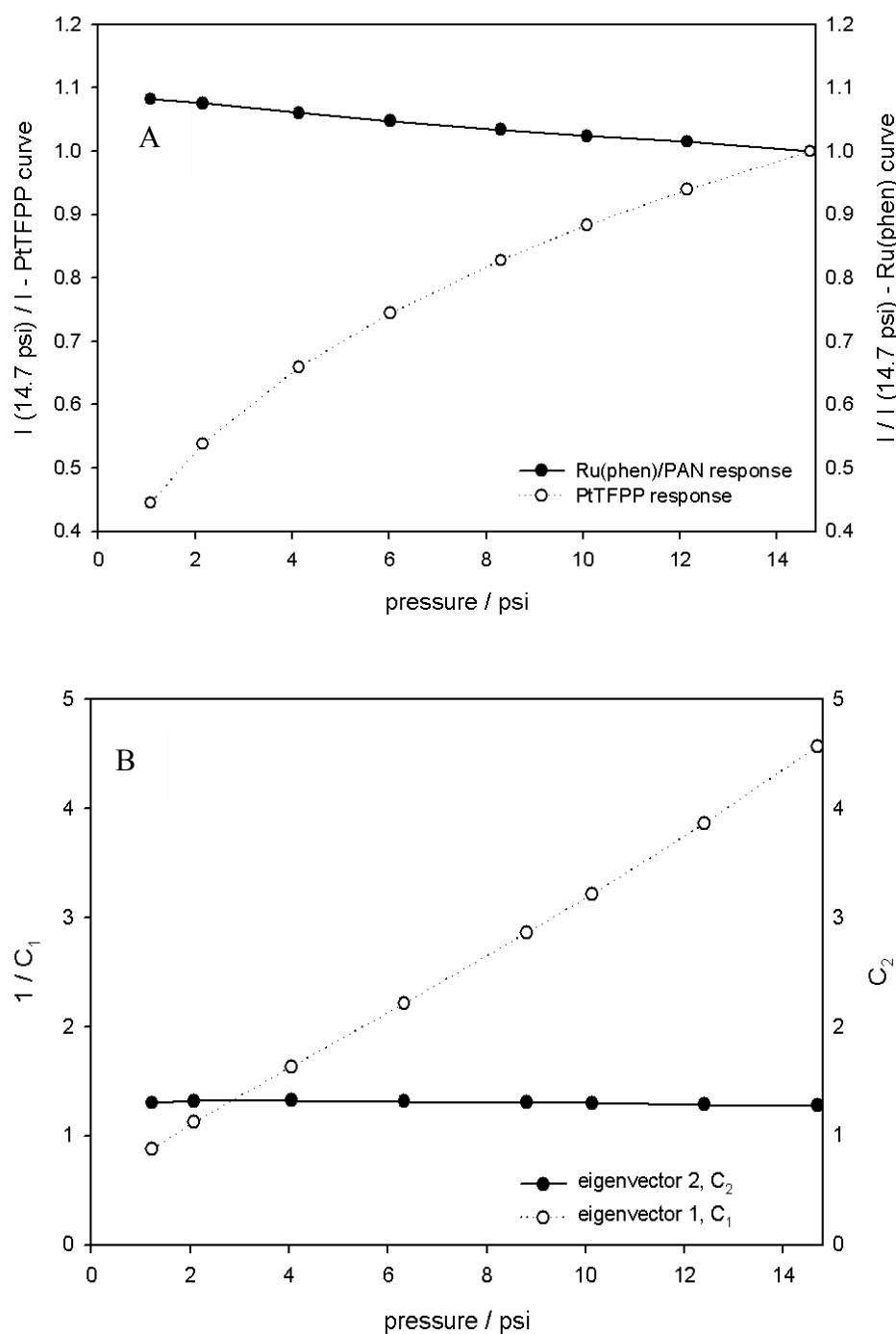


Figure 3-4: Comparison of intensity-ratios with their corresponding eigenvector elements. A) The pressure response of PtTFPP emission centered at 650 nm (blank circles), and of Ruphen/PAN emission centered at 580 nm (filled circles). Data are collected from fluorimeter for the conditions that correspond to 292.9 K listed in Table 3-1. B) The variation of  $C_1$  and  $C_2$  with pressure for various pressures at 292.9 K.

In summary, PCA of the spectroscopic data set illustrates that it is possible to separate the pressure and temperature dependence of the dual-luminophore PSP. In the next section, the application of PCA to CCD image data will be presented as it is the one of main objectives of this study.

### PCA Results for CCD Camera Data Set

CCD image data was obtained on a dual-luminophore PSP coated coupon installed into a pressure chamber as described in the experimental section. The coupon was subjected to a temperature gradient, and there were 5 thermocouples installed to provide five specific points on the surface where the temperature is calibrated (Figure 3-5).

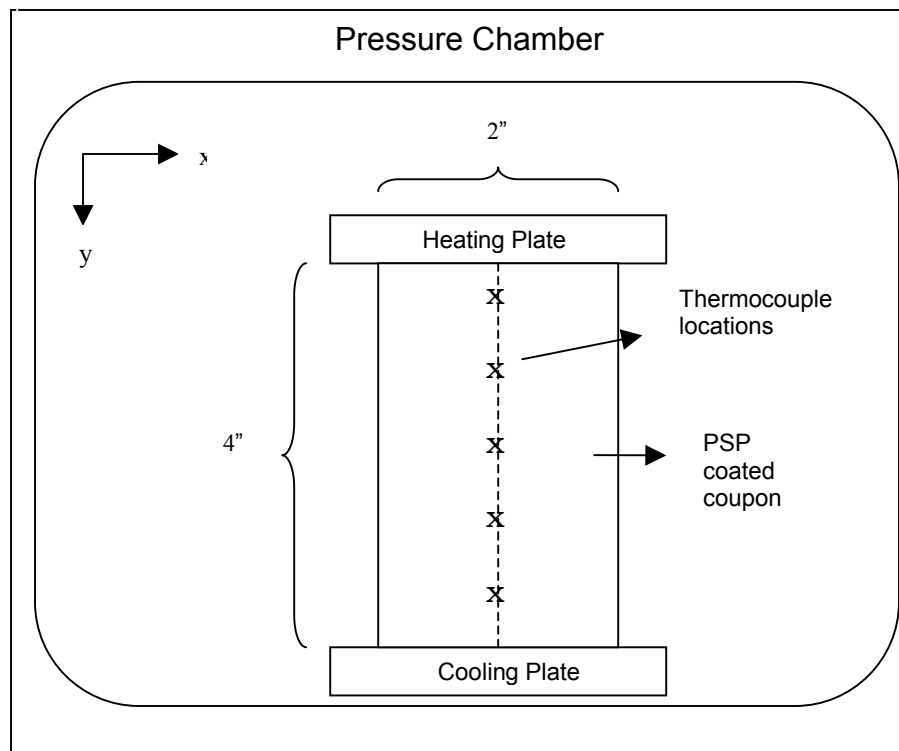


Figure 3-5: Experimental setup for CCD image data collection. Thermocouple locations are shown as 'X' marks.

CCD images were obtained at 13 different pressures, affording  $5 \times 13 = 65$  known P-T conditions. At each pressure, CCD images were obtained with 4 different bandpass filters covering the spectral range from 550 – 700 nm. Thus, the PCA algorithm was applied to a matrix of size 4 (wavelengths)  $\times$  65 (pressure-temperature combinations),  $\mathbf{D}_{4 \times 65}$ . The transformation matrix used for the CCD image data was the same as the one optimized for the spectroscopic data (equation (3-21)); however, the rotation angle ( $\theta$ ) was empirically chosen to be  $10^\circ$  in order to maximize the pressure and temperature decoupling in  $\mathbf{C}_1(P, \sigma T)$  and  $\mathbf{C}_2(T, \sigma P)$  for the CCD calibration data set.

In order to allow prediction of the pressure and temperature values at unknown points on the model, the  $\mathbf{C}_1$  and  $\mathbf{C}_2$  values determined from PCA for the calibration data are fitted to pressure and temperature using equations (3-22) and (3-23), where the coefficients were determined by a non-linear least squares regression in SigmaPlot. These expressions provide “calibration surfaces” that are then used to predict P and T for any combination of  $\mathbf{C}_1$  and  $\mathbf{C}_2$  values which are recovered from points on the coupon surface where P and T are not known. The correlation coefficients for the empirical fits were 0.999 or better. Confidence interval of fits at 95% for P and T are also given with the equations below.

$$P = -3.098 + 8.792 \cdot C_1 - 3.040 \cdot C_2 - 5.782 \cdot C_1 \cdot C_2 - 2.023 \cdot C_1^2 + 15.36 \cdot C_2^2 + 2.639 \cdot C_1^2 \cdot C_2 - 20.01 \cdot C_2^2 \cdot C_1 + 7.498 \cdot C_1^2 \cdot C_2^2 \pm 0.10 \text{ psi}(95\%) \quad (3-22)$$

$$T = 237.3 + 107.8 \cdot C_1 + 14.16 \cdot C_2 - 13.52 \cdot C_1 \cdot C_2 - 36.59 \cdot C_1^2 - 0.2342 \cdot C_2^2 + 5.046 \cdot C_1^2 \cdot C_2 + 2.182 \cdot C_2^2 \cdot C_1 - 1.075 \cdot C_1^2 \cdot C_2^2 \pm 0.40 \text{ K}(95\%) \quad (3-23)$$

In order to calculate the  $\mathbf{C}_1$  and  $\mathbf{C}_2$  values for an unknown pixel in the CCD images (unknown P and T), the data for one of the calibration conditions (the last column in the

calibration data matrix,  $\mathbf{D}_{4 \times 65}$ ) is replaced with the data for the unknown pixel (a column of 4  $I_{\text{ref}}/I$  values corresponding to the four wavelengths at the unknown point). Then the PCA algorithm is applied to this new  $\mathbf{D}'_{4 \times 65}$  matrix. The newly found  $C_1^{\text{unk}}$  and  $C_2^{\text{unk}}$  for the unknown point are then put in equations (3-22) and (3-23) to estimate P and T for the pixel. Initial results showed that this approach leads to an approximate 1% error in the predicted P and T for the unknown pixel. This is because introducing an unknown column of data into the  $\mathbf{D}$  matrix slightly changes the values of the  $\mathbf{C}$  elements (for which equations (3-22) and (3-23) are fitted) obtained from original calibration data matrix,  $\mathbf{D}_{4 \times 65}$ . In essence, introduction of the unknown pixel data into the PCA analysis slightly changes the calibration surfaces defined by equations (3-22) and (3-23).

Hence,  $C_1^{\text{unk}}$  and  $C_2^{\text{unk}}$  can not be used for the calibration surfaces given by equations (3-22) and (3-23). Let us assume that  $C_1^{\text{unk, corr}}$  (corrected  $C_1^{\text{unk}}$ ) and  $C_2^{\text{unk, corr}}$  (corrected  $C_2^{\text{unk}}$ ) are true coefficients that lie on the original pressure and temperature calibration surfaces before an unknown point is introduced in  $\mathbf{D}_{4 \times 65}$  matrix. If we can find the difference between  $C^{\text{unk, corr}}$  and  $C^{\text{unk}}$ , we would then add this difference to  $C^{\text{unk}}$  and obtain  $C^{\text{unk, corr}}$  and use  $C^{\text{unk, corr}}$  in equations (3-22) and (3-23) to get the correct pressure and temperature. This can be achieved by first estimating the pressure and temperature by using  $C_1^{\text{unk}}$  and  $C_2^{\text{unk}}$ , then by calculating the average change as a function of pressure and temperature ( $\Delta C_1(P) = C_1(P) - C_1^{\text{unk}}(P)$  and  $\Delta C_2(T) = C_2(T) - C_2^{\text{unk}}(T)$ ) in the values of original  $\mathbf{C}$  elements upon introduction of unknown points for different pressures and temperatures. Finally, the correction to  $C_1^{\text{unk}}$  and  $C_2^{\text{unk}}$  is made by adding  $\Delta C_1$  and  $\Delta C_2$ , respectively. This procedure essentially maps the  $C_1^{\text{unk}}$  and  $C_2^{\text{unk}}$

values onto the calibration surfaces defined by equations (3-22) and (3-23) determined by using the original **D** matrix.

In order to explore the effects of varying the parameters for the PCA analysis on the results, the size of the **D** matrix was varied ( $\mathbf{D}_{4 \times 15}$ ,  $\mathbf{D}_{4 \times 30}$ , and  $\mathbf{D}_{4 \times 70}$ ) by decreasing the number of conditions to explore the magnitude of  $\Delta C_1$  and  $\Delta C_2$  dependence with **D**. It was found that as the dimension of **D** decreases,  $\Delta C_1$  and  $\Delta C_2$  increases and correction to  $C_1^{\text{unk}}$  and  $C_2^{\text{unk}}$  becomes more important. The effect of the number of different image wavelengths (bandpass filters) used on the results was also examined. It was found that removal of the 700/10 nm filter data, thereby reducing **D** to a 3 x 65 matrix, had very little effect on the PCA results. However, decreasing **D** to a 2 x 65 matrix (using 550/40 and 650/10 filter images only) produced relatively poor results.

The procedure outlined above was applied to every pixel in the CCD image (231 x 426 = 98,406 pixels). For each pressure image (this corresponds to the 4 ratio images obtained using the 4 different color filters), the PCA algorithm required *ca.* 2 hrs to calculate the P and T surface distributions on a WinTel-based PC (P4 CPU, 2.40 GHz, 1 GB ram).

Table 3-2 collects the predicted average P values for the coupons at the 13 different pressures (the average and standard deviation in P was determined by averaging the estimated P values at all points in each image). Note that the predicted pressures are very close to the experimental measurements and the highest standard deviation is only 0.05 psi, indicating that the dual-luminophore PSP combined with PCA analysis provides good precision and accuracy when predicting pressure, even though the coupon is subjected to a *ca.* 20 °C temperature gradient.

Table 3-2: Accuracies of average pressure estimates for intensity-ratio method and PCA method for dual-luminophore PSP imaging data.

<b>P(exp)±0.01 psi</b>	<b>PCA calibration</b>			<b>Intensity-ratio Calibration</b>		
	P(est)	$\sigma$ (psi)	% error for P	P(est)	$\sigma$ (psi)	% error for P
<b>1.04</b>	1.09	0.01	+4.8	1.08	0.03	+3.8
<b>1.99</b>	1.98	0.02	-0.5	1.99	0.02	0
<b>3.01</b>	3.00	0.02	-0.3	3.00	0.02	-0.3
<b>4.01</b>	3.97	0.02	-1.0	3.98	0.03	-0.8
<b>5.04</b>	5.01	0.02	-0.6	5.01	0.05	-0.6
<b>6.00</b>	6.04	0.03	+0.7	6.02	0.06	+0.3
<b>6.97</b>	7.01	0.03	+0.6	7.01	0.06	+0.6
<b>8.00</b>	8.04	0.03	+0.5	8.05	0.06	+0.6
<b>9.00</b>	9.07	0.03	+0.8	9.06	0.06	+0.7
<b>9.96</b>	10.01	0.03	+0.5	10.07	0.06	+1.1
<b>12.02</b>	12.06	0.05	+0.3	12.10	0.07	+0.7
<b>12.99</b>	13.04	0.05	+0.4	13.08	0.10	+0.7
<b>14.00</b>	14.00	0.05	0	14.10	0.12	+0.7

Figure 3-6 provides examples of CCD images obtained on the coupon surface as well as example P and T surface maps. The top two images in Figure 3-6 show uncorrected image ratios ( $I_{ref}/I$ ) for four pressures obtained at the wavelengths corresponding to the emission maximum for the Ruphen and PtTFPP dyes. Note that in each image there is a well-defined gradient in the uncorrected intensity ratio; since the pressure on the surface is constant, the gradient arises due to the temperature gradient on the coupon.

The bottom two images in Figure 3-6 show the PCA-calibrated P and T surface distributions. As expected, the pressure maps are spatially uniform, while the temperature maps quantify the temperature gradient created by the experimental arrangement.

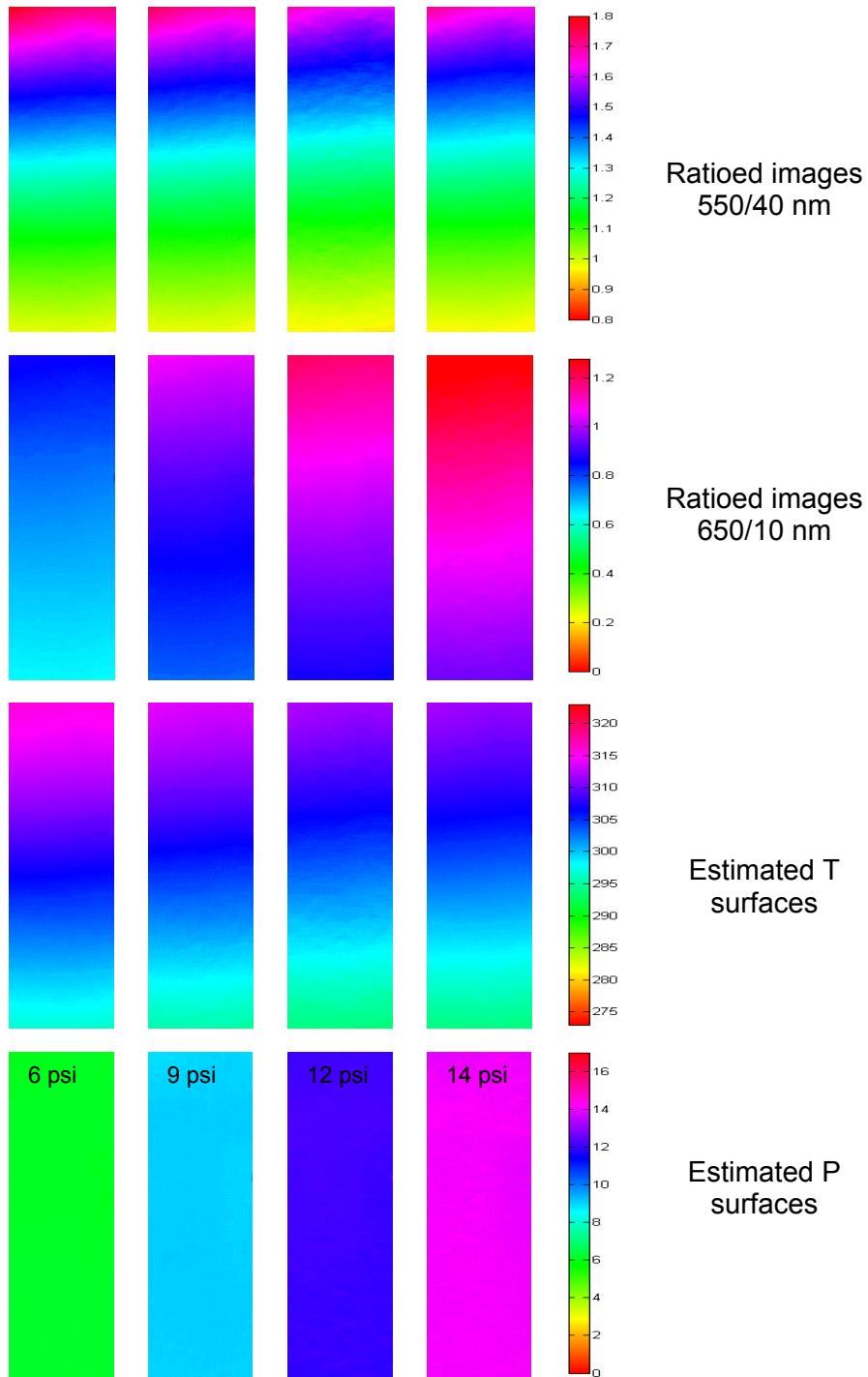


Figure 3-6: First and second rows: Images were obtained from ratio images of 550/40 nm and 650/10 nm filters at 6, 9, 12, and 14 psi, respectively. Third and fourth rows: The false colored predicted temperature (third row) and pressure surfaces (fourth row) obtained by using PCA calibration method. Each surface image is 1" X 3.86" in size, the images were cropped from the same segment of 2" X 4" coupon shown in Figure 3-5.

Quantitative information concerning the precision and accuracy by which temperature is predicted is provided in Figure 3-7, where the estimated values are plotted as lines from the top to the bottom of the coupon for 6 different pressures (the values comprising the lines were taken from a vertical column of pixels at the center of the coupon). The calibration points (thermocouple locations) are shown in the plots as circles.

Overall it is evident that the PCA method accurately predicts the surface temperature. The highest error in estimated temperature was 0.4 K, and the average error was 0.2 K. Interestingly, it is evident that the average temperature of the coupon increases with decreasing pressure. This effect arises because the rate of convective cooling of the plate increases with the pressure in the chamber.

Finally, it is also evident that the standard deviation in the predicted temperature increases with decreasing pressure (this is evident as noise in the line plots at low pressures in Figure 3-7). It is believed that the origin of this effect arises because at lower pressures the  $\mathbf{D}$  matrix is dominated by the PtTFPP emission and small variations in the intensity of the signal gives rise to the error in  $T$ .

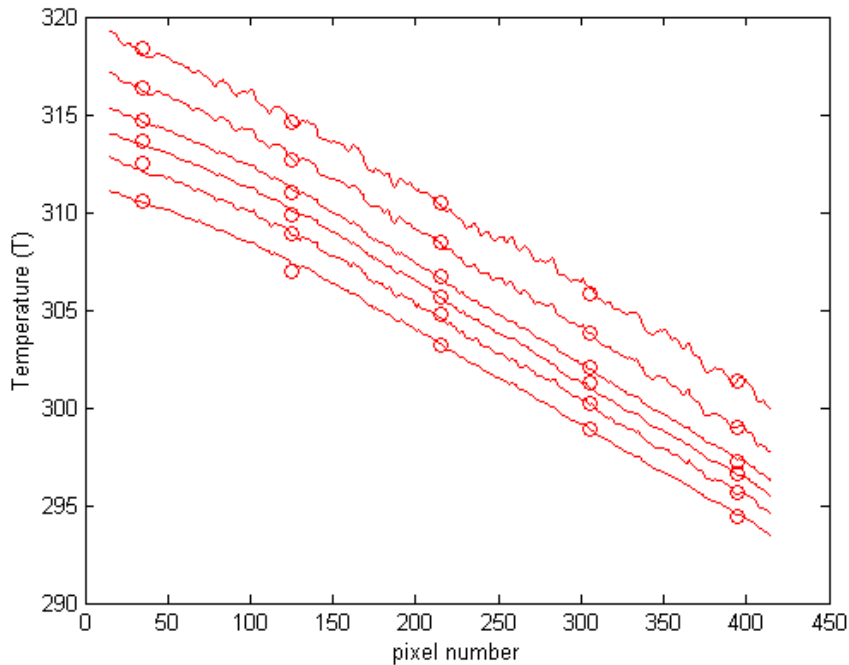


Figure 3-7: The predicted temperature gradient from top to the bottom of the coupon as indicated by lines for 6 different pressures (top-1.99 psi, 4.01 psi, 6.00 psi, 8.00 psi, 9.96 psi, 14.00 psi-bottom). The thermocouple data are depicted as circles. Only six estimated temperature surface is shown, the others are omitted for clarity.

### Intensity-Ratio Method Results for CCD Camera Data Set

In order to provide a benchmark by which to assess the improvement in recovery of P and T values afforded by using dual-luminophore PSP data, the CCD image data was also subjected to intensity-ratio analysis. This method has been used by others to construct pressure and temperature surfaces from dual-luminophore PSP image data.<sup>3</sup> Intensity ratios for 65 known P-T conditions for image data acquired using the 550/40 and 650/10 nm bandpass filters ( $2 \times 65 = 130$  points) were fitted by non-linear regression in SigmaPlot to equations (3-1) and (3-2) affording the calibration coefficients shown in equations (3-24) and (3-25). By analogy to the PCA calibration functions, the correlation coefficients for the non-linear regressions were  $\geq 0.999$ . The P and T calibration surfaces

plotted by using equations (3-24) and (3-25) are shown in Figure 3-8A and 3-8B, respectively.

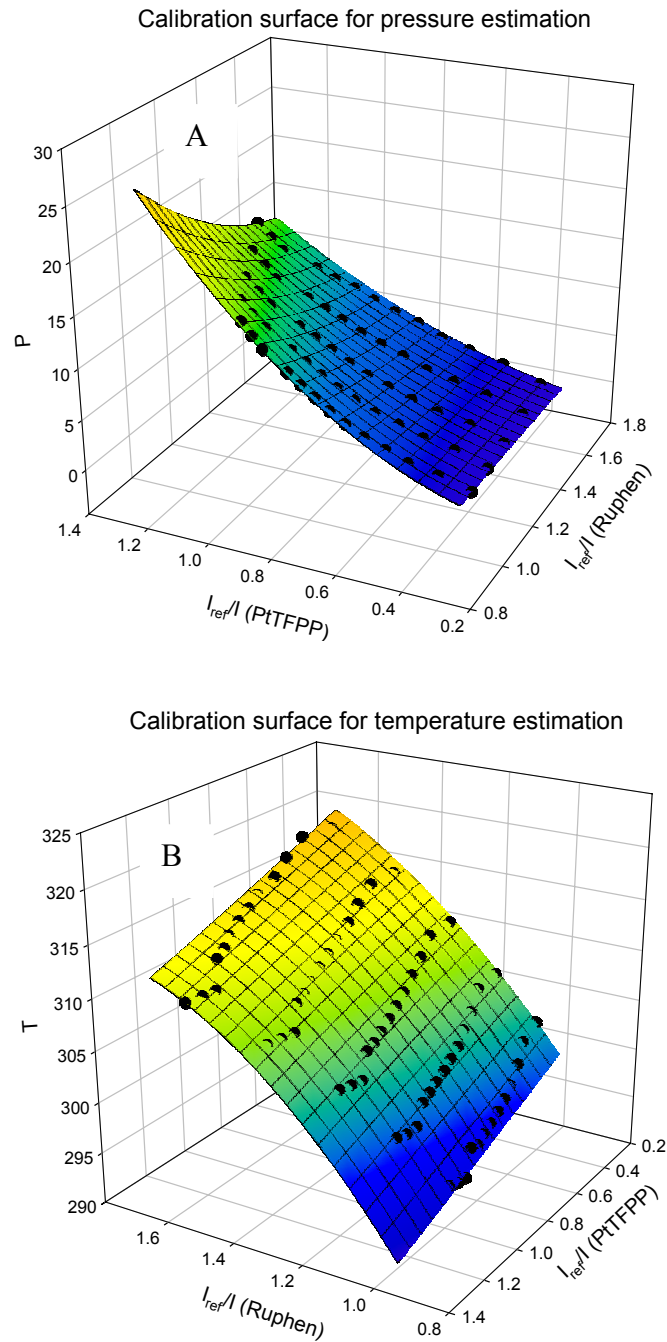


Figure 3-8: Calibration surfaces. A) The calibration surface for pressure obtained from intensity-ratio method. The calibration points are represented as dots. B) The calibration surface for temperature obtained from intensity-ratio method. The calibration points are represented as dots.

In these 3-D plots, the points represent the 65 known P-T calibration points, whereas the surfaces represent the functions in equations (3-24) and (3-25).

$$P = -3.842 + 5.895 \cdot X - 0.9546 \cdot Y - 1.332 \cdot X \cdot Y - 2.323 \cdot X^2 + 41.12 \cdot Y^2 + 1.553 \cdot X^2 \cdot Y - 35.50 \cdot Y^2 \cdot X + 9.034 \cdot X^2 \cdot Y^2 \pm 0.18 \text{psi}(95\%) \quad (3-24)$$

$$T = 261.3 + 48.88 \cdot X - 54.55 \cdot Y + 75.30 \cdot X \cdot Y - 7.381 \cdot X^2 + 18.56 \cdot Y^2 - 28.62 \cdot X^2 \cdot Y - 30.21 \cdot Y^2 \cdot X + 11.64 \cdot X^2 \cdot Y^2 \pm 0.42 \text{K}(95\%) \quad (3-25)$$

It is important to note that the precision of the fit of the intensity-ratio pressure calibration data at the 95% confidence interval (equation (3-24)) is two times that which is recovered for the PCA coefficient calibration (equation (3-22)). By contrast, the 95% confidence intervals for fitting of the calibration values for T by the intensity-ratio and PCA methods are similar (equations (3-23) and (3-25)).

By using equations (3-23) and (3-24) the P and T values at every pixel on the coupon surface were computed, and then the average and standard deviation in the pressure was determined and the results are listed in the right set of columns in Table 3-2. It is evident that the average pressure prediction from the intensity-ratio method at high pressure is not as good as those recovered from the PCA method. The larger error likely results from the fact that the temperature interference is larger at higher pressures. In addition the intensity-ratio method also gives rise to larger standard deviations for pressure images which likely results from the fact that the sensitivity of the image-ratios to pressure is lower (Figure 3-4A vs. Figure 3-4B).

### **Calibration Results for Three-Component PSP**

#### **Image Registration**

As discussed in Chapter 2, a three-component PSP allows both internal referencing and temperature correction by using the emission from three luminophores immobilized

in the polymer medium. In this formulation, Rh110 emission was used as reference signal which was proposed to eliminate the need for wind-off image in PSP applications.

The imaging experiment for three-component PSP was almost the same as that used for the dual-luminophore PSP, except that a new filter (530/10 nm) was used for Rh110 emission. All images collected with 550/40 nm, 600/10 nm, and 650/10 nm filters were ratioed by the images collected with 530/10 nm filter images at the same condition. Figure 3-9A shows Rh110 ratioed image obtained by ratioing 530/10 nm filter with 650/10 nm filter with a temperature gradient across the coupon (disregard the circular points (screws) which appear at the corners in the images and on the middle center line). PtTFPP emission at 650 nm is temperature dependent; however, Rh110 emission at 525 nm is not sensitive to temperature changes. Therefore, Figure 3-9A should show a smooth temperature gradient across the image. The image illustrates such a gradient; however, the gradient is not uniform.

This result means that a simple ratio with Rh110 emission does not totally account for the variations due to the illumination field and paint thickness.<sup>92</sup> The expected temperature variation on the coupon is demonstrated by the ratio image shown in Figure 3-9B where there is a uniform change in intensities across the coupon from top to bottom.

In the literature, it has been shown that by using ratio-of-ratios  $(I_{\text{ref}}/I)_{\text{PtTFPP}} / (I_{\text{ref}}/I)_{\text{Rh110}}$ , it is possible to obtain registered images that fully compensate the changes in excitation light variation and paint thickness variation on the model.<sup>93</sup> It has also been argued that ratio-of-ratios increase uncertainty by doing multiple image registrations and lacks the advantage of internal referencing.

In this context, we also calculated ratio-of-ratio images by using three-component PSP raw images. One of them is illustrated in Figure 3-9C. As opposed to Figure 3-9A, Figure 3-9C shows a uniform temperature gradient that resembles the one seen in Figure 3-9B.

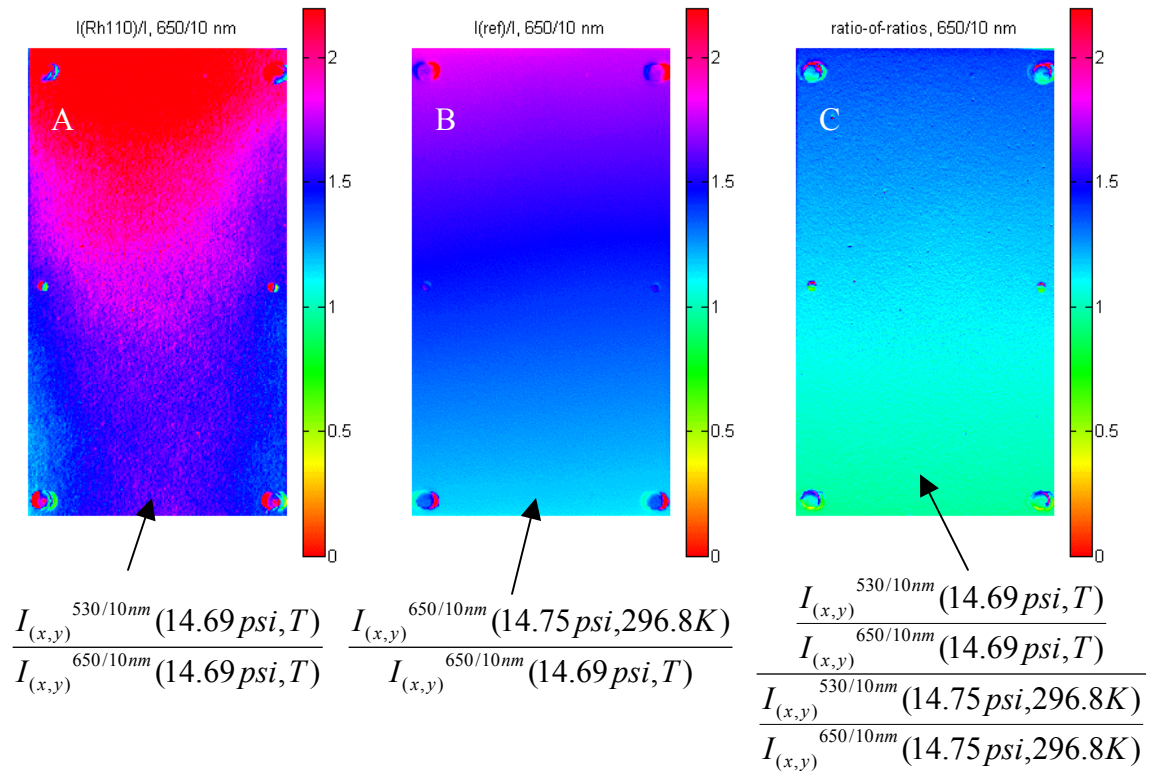


Figure 3-9: Ratio images. A) Image obtained by ratioing 530/10 nm and 650/10 nm filter images collected at 14.69 psi with a temperature gradient across the coupon. B) Image obtained by ratioing 650/10 nm filter reference image with 650/10 nm filter image collected at 14.69 psi with a temperature gradient across the coupon. C) Image obtained by ratioing image A with the ratio of corresponding reference filter images.

Nevertheless, the image in Figure 3-9C is grainy and the intensity variation is not as smooth as the one shown in Figure 3-9B. This behavior led us to analyze the standard

deviation in the paint response upon temperature difference with different image registration methods.

Figure 3-10 shows the ratio values for the images shown in Figure 3-9 as one follows the dashed line in Figure 3-5 (middle center line in y axis). Blue line is obtained from Figure 3-9A and has the highest amount of noise in the plot. Moreover, the blue line is not decreasing linearly as would be expected since the sample has a linear temperature gradient. The green line is obtained from Figure 3-9B and shows the lowest noise in the plot with a nice linear response. Red line is obtained from Figure 3-9C and although the response is linear, it has more noise compared to green line.

The reason for noisier response for ratio-of-ratios image is that we have to do image ratioing three times as opposed to one time in a regular image registration operation. Moreover, PtTFPP is molecularly dissolved in the paint and Rh110 is encapsulated in nanoparticles which itself induces some noise in the paint response. Nonetheless, the same type of noise in ratio-of-ratios images was also observed for other filters (600/10 nm and 550/40 nm) where they map the nanoparticle emission.

This suggests that the main reason for noisier response in ratio-of-ratio images is the necessity for increased number of image registrations which increases the uncertainty in paint response.

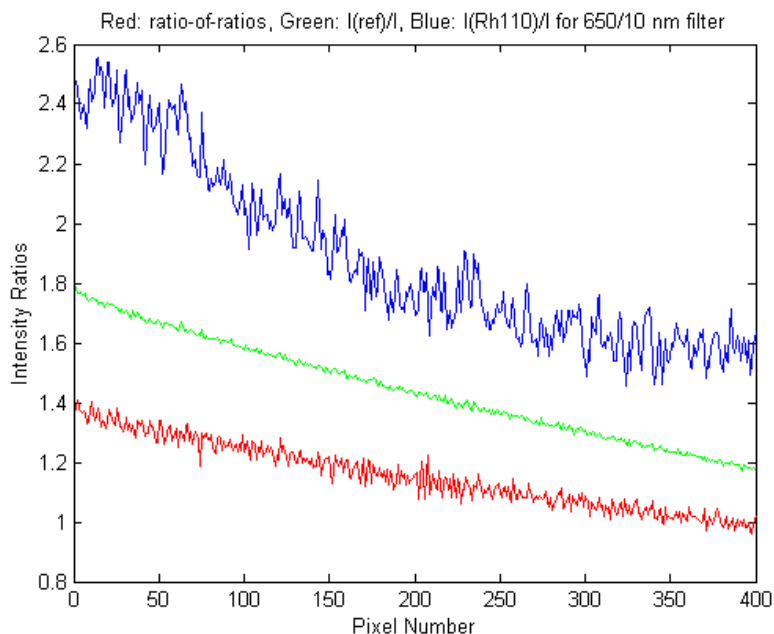


Figure 3-10: Comparison of noise levels of the images shown in Figure 3-9.

The question that remains to be answered is why internal referencing does not work completely. To be able to answer that question, it is helpful to analyze the reference images obtained through 530/10 nm and 650/10 nm filter. Figure 3-11A and 3-11B are reference images for Rh110 and PtTFPP emissions respectively, collected at constant pressure and temperature. The variation in the illumination field caused by blue LED excitation is visible in both images. More excitation light impinges on the lower segment of the coupon than on the upper part. Since both images were collected at constant temperature and pressure, ratioing the two images should result in an image that is single in color. Figure 3-11C shows such a ratioed image which is mostly green in color; however, there is also some intensity variation in the ratioed values. Although it is evident that most of the illumination light variation has been eliminated by taking ratios of two reference images, there is still substantial spatial variation in intensity remaining in the ratioed image (as much as 15%). This result means that PtTFPP and Rh110 reacts

differently to different illumination field intensity, for example, if the excitation light intensity is doubled at some part of the coupon, the emissions emanating from Rh110 and PtTFPP do not follow the same trend. PtTFPP emission increases by 1.9-fold and Rh110 emission increases by 1.8-fold. When the ratio image is calculated by using Rh110 as reference, Rh110 ratioed image successfully accounts for most of the excitation light variation, but not all of it. Note that the coating thickness is relatively uniform, so we do not expect there to be an effect of thickness variation in the ratioed image.

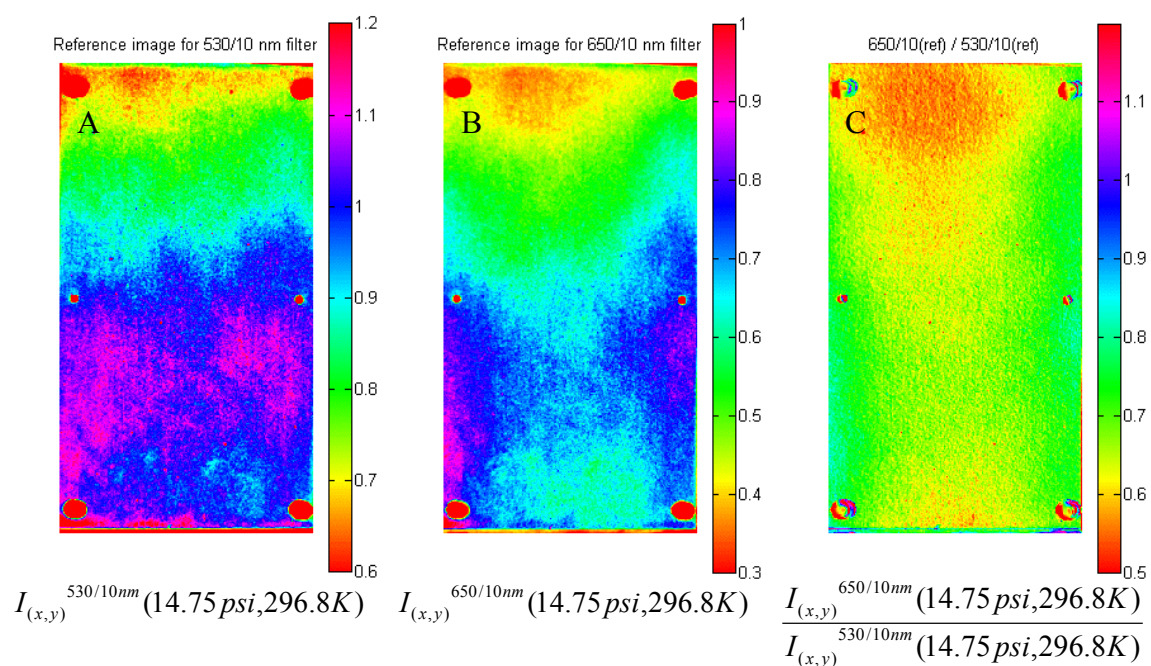


Figure 3-11: Reference images. A) Reference image obtained through 530/10 nm filter. B) Reference image obtained through 650/10 nm filter. C) Ratio of A and B.

Although the ratio-of-ratios,  $(I_{RL}/I_{PSL})_{run} / (I_{RL}/I_{PSL})_{ref}$  introduces more uncertainty and requires more image registration, we believe that this type of image registration is still an improvement over conventional image registration,  $(I_{PSL})_{ref} / (I_{PSL})_{run}$ . There are several reasons for that: (1) flat-field correction is not necessary for ratio-of-ratios images, (2)  $(I_{RL}/I_{PSL})_{run}$  and  $(I_{RL}/I_{PSL})_{ref}$  images are easy to calculate because of minimal

model movement, yet ratioing  $(I_{RL}/I_{PSL})_{run}$  with  $(I_{RL}/I_{PSL})_{ref}$  might be difficult, though, since most of the illumination field and paint thickness variations are accounted in  $(I_{RL}/I_{PSL})_{run}$  images, aligning  $(I_{RL}/I_{PSL})_{run}$  and  $(I_{RL}/I_{PSL})_{ref}$  images is not very crucial, (3) ratio-of-ratios images compensate for variations in incident light intensity, (4) ratio-of-ratios images also compensate for varying luminophore concentration (for instance; photobleaching of luminophores or dye leaking) in the binder. Thus, we employed ratio-of-ratios images in data calibration for three-component PSP.

### **PCA Calibration for Spectroscopic Data Set**

Three-component PSP spectra were collected with a fluorimeter at 28 different pressure-temperature combinations. PCA algorithm was applied to the spectroscopic data set ( $\mathbf{D}_{246 \times 28}$ ) in order to reveal the factors that define pressure and temperature variation in the data (Figure 3-12). PCA produced three important factors for this data set. As a matter of fact, there are three real factors in the spectra; one of the factors is due to reference sensor emission which is constant at all pressures and temperatures, another one should represent the temperature variation, and the third one should represent the pressure variation.

Although two factors can describe 98.4% of the variation in the spectra, omitting third factor leads to erroneous representation of raw data,  $\mathbf{D}$ . Thus, using only two factors is not sufficient to account for all of the variation in the data (Figure 3-13). If three factors are used, then a true reproduction of  $\mathbf{D}$  is possible which describes 99.99% of variation in raw data set (Figure 3-14).

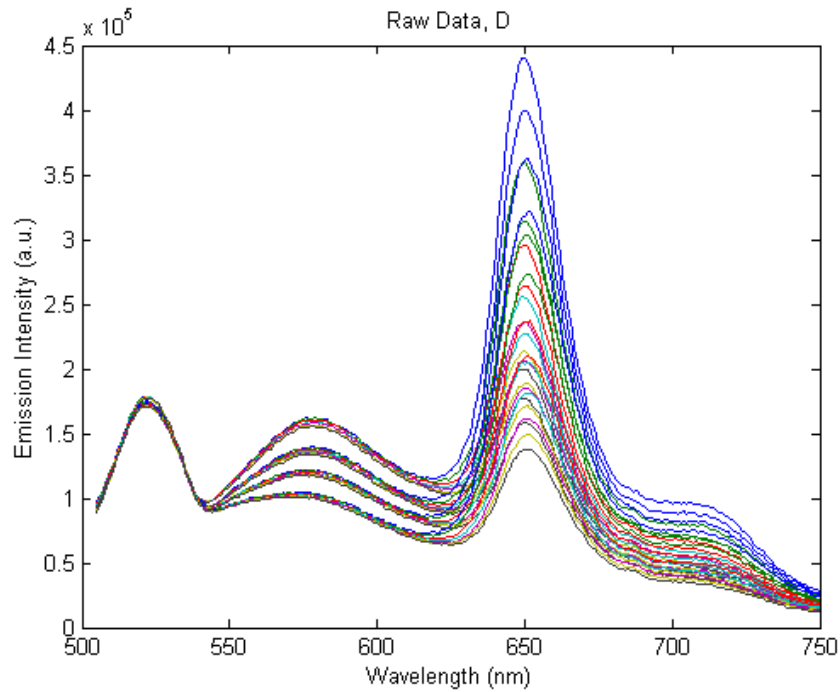


Figure 3-12: Emission intensity spectra of three-component PSP at various pressure-temperature combinations. Excitation wavelength: 470 nm.

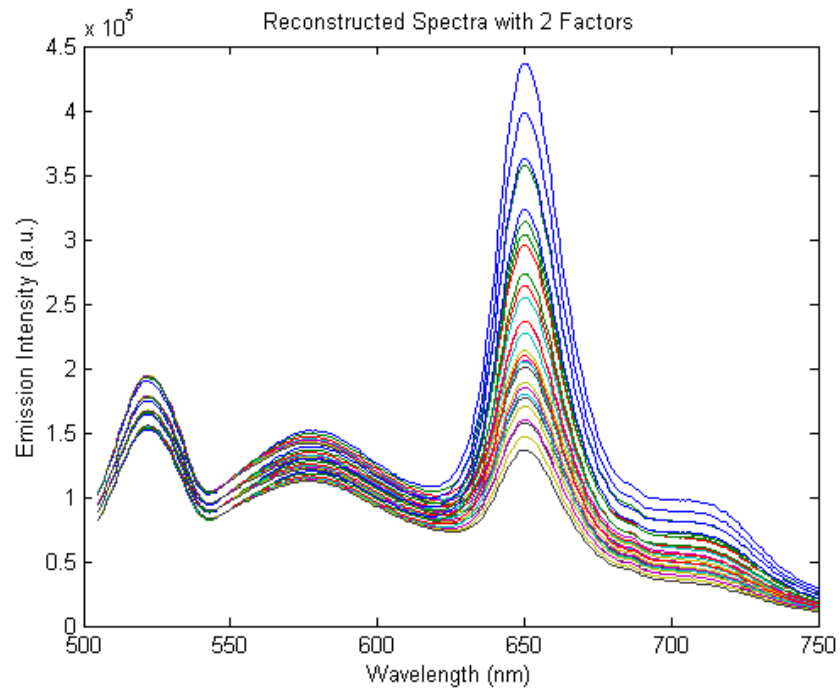


Figure 3-13: Reconstructed spectra,  $D''$  for three-component PSP obtained with two largest factors.

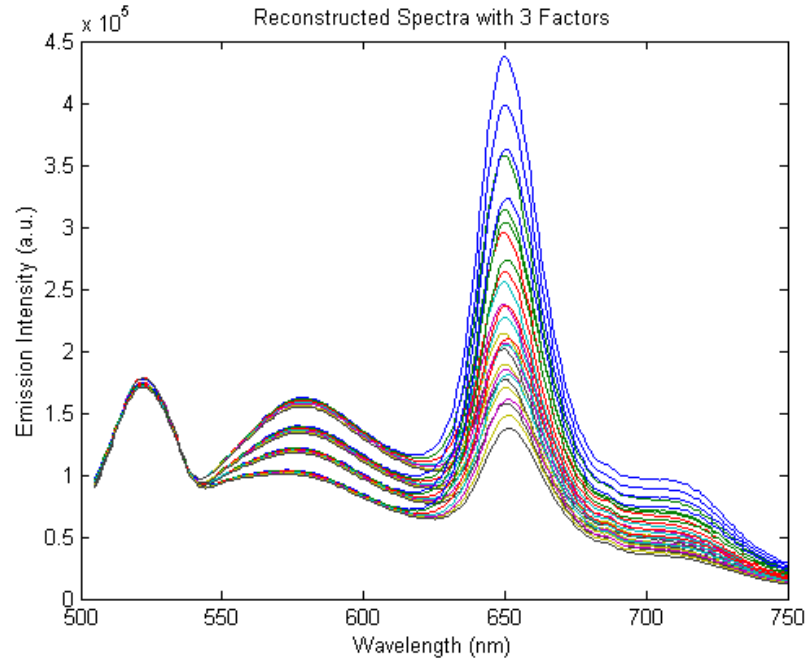


Figure 3-14: Reconstructed spectra,  $D''$  for three-component PSP obtained with three factors.

We first applied orthogonal transformation matrices that allow rotation in x, y, and z axis, because we have three factors in factors space which need to be rotated in three axes (equation 3-26). However, since there are many combinations ( $360 \times 360 \times 360$ , considering only integer numbers) associated with rotations in three axes, the method was discontinued.

$$\begin{aligned}
 T_x &= \begin{bmatrix} 1 & 0 & 0 \\ 0 & \cos(\theta_x) & -\sin(\theta_x) \\ 0 & \sin(\theta_x) & \cos(\theta_x) \end{bmatrix} \\
 T_y &= \begin{bmatrix} \cos(\theta_y) & 0 & -\sin(\theta_y) \\ 0 & 1 & 0 \\ \sin(\theta_y) & 0 & \cos(\theta_y) \end{bmatrix} \\
 T_z &= \begin{bmatrix} \cos(\theta_z) & -\sin(\theta_z) & 0 \\ \sin(\theta_z) & \cos(\theta_z) & 0 \\ 0 & 0 & 1 \end{bmatrix} \\
 T &= T_x T_y T_z
 \end{aligned} \tag{3-26}$$

Instead, we used a 3 x 3 transformation matrix to simplify the calculations. Yet, the transformation matrix has 9 unknown elements that need to be determined in order to find real factors. Many attempts to find the correct transformation matrix that will resolve these factors led to no meaningful results. Therefore, we report here one of the best results that was achieved in factor rotation.

Figure 3-15 illustrates the fundamental spectra of three factors before target transformation while Figure 3-16 shows the fundamental spectra after target transformation. Note that Figure 3-16 does not demonstrate real factor spectra; it represents one of the best results that we achieved in our search for true factor rotation.

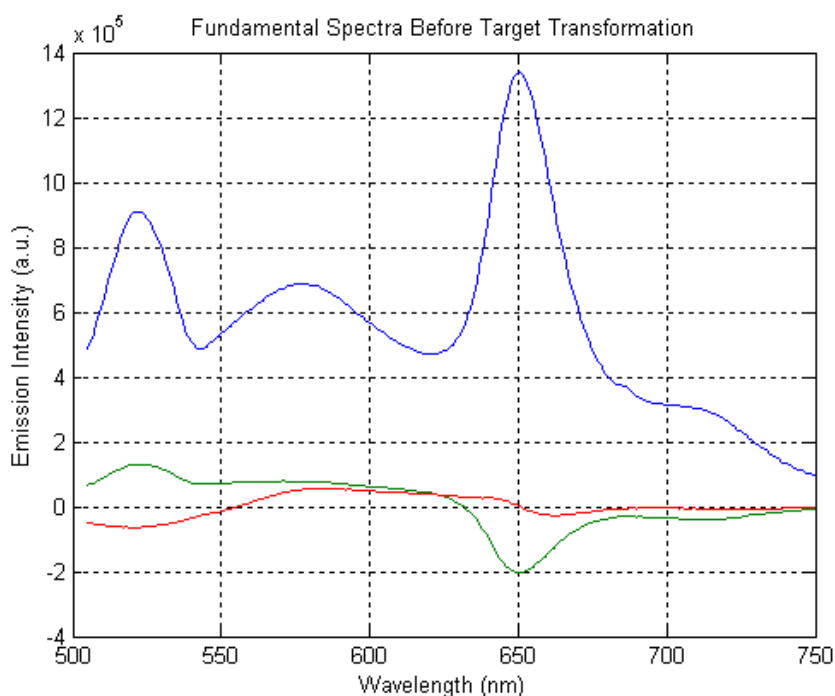


Figure 3-15: Fundamental spectra for abstract factors.

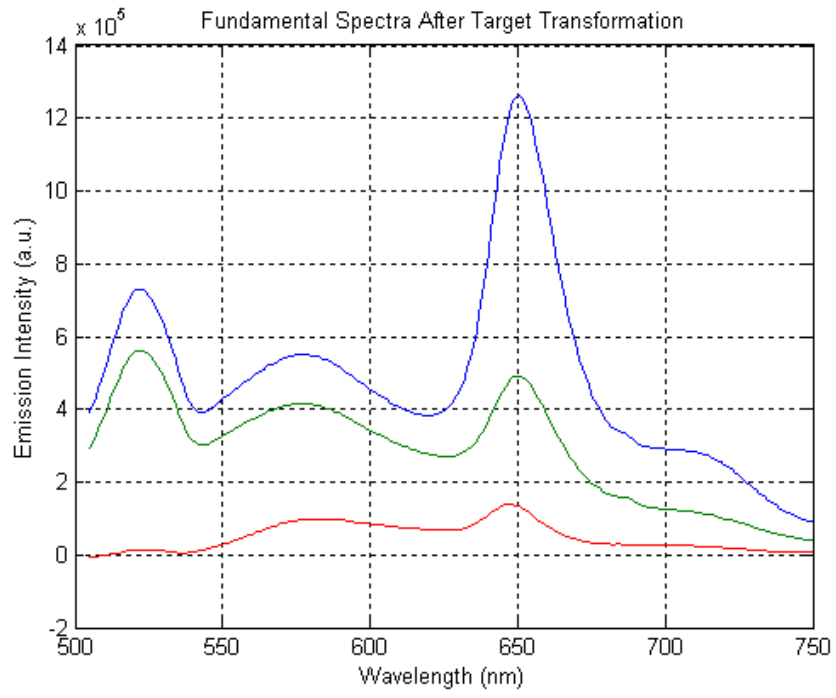


Figure 3-16: Fundamental spectra of three factors after target transformation.

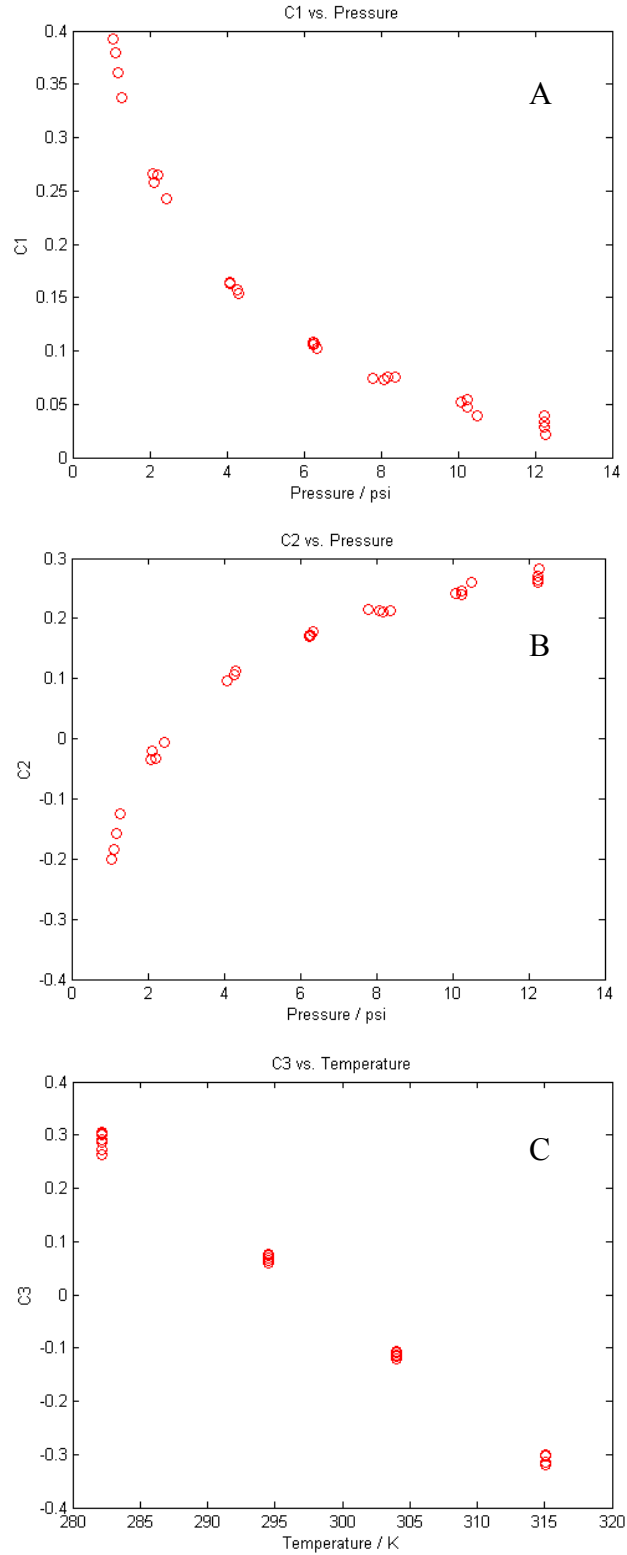


Figure 3-17: Variation of eigenvector elements with pressure and temperature A) Pressure dependence of  $C_1$ . B) Pressure dependence of  $C_2$ . C) Temperature dependence of  $C_3$ .

When we analyze the pressure and temperature dependence of the factors obtained after rotation, we see that the eigenvectors of first two factors (blue and green spectra in Figure 3-16) are mostly pressure dependent (Figure 3-17A and 3-17B), the eigenvector of third factor (red spectrum in Figure 3-16) is mostly temperature dependent (Figure 3-17C).

### PCA Calibration Results for CCD Camera Set Data

We calculated ratio-of-ratios  $(I_{(x,y)}^{530/10nm}/I_{(x,y)}^{filter})_{run} / (I_{(x,y)}^{530/10nm}/I_{(x,y)}^{filter})_{ref}$  images by using the raw three-component PSP images obtained through 530/10 nm, 550/40 nm, 600/10 nm, and 650/10 nm filters from CCD camera in the vacuum chamber experiment in order to construct imaging calibration data set.

PCA algorithm also produced three important factors for a  $\mathbf{D}_{4 \times 65}$  filter data. Due to the difficulties in finding the correct transformation matrix that will yield real factors, we did not apply any transformation on the factors; instead, we used abstract factors in the calibration functions. Since  $\mathbf{C}_1$  and  $\mathbf{C}_2$  described most of the variance in the data, we fitted pressure and temperature as a function of elements of  $\mathbf{C}_1$  and of  $\mathbf{C}_2$  with regression coefficients 0.999 and 0.998, respectively. Confidence interval of fits at 95% for  $P$  and  $T$  are given with the equations below.

$$P = -15.16 + 474.5 \cdot C_1 - 36.33 \cdot C_2 - 1511 \cdot C_1 \cdot C_2 - 2292 \cdot C_1^2 - 9.92 \cdot C_2^2 + 7023 \cdot C_1^2 \cdot C_2 + 828.4 \cdot C_2^2 \cdot C_1 - 2044 \cdot C_1^2 \cdot C_2^2 \pm 0.13 \text{psi}(95\%) \quad (3-27)$$

$$T = 167.6 + 1331 \cdot C_1 - 227.6 \cdot C_2 + 4816 \cdot C_1 \cdot C_2 - 1564 \cdot C_1^2 + 751.9 \cdot C_2^2 - 18610 \cdot C_1^2 \cdot C_2 - 8338 \cdot C_2^2 \cdot C_1 + 22280 \cdot C_1^2 \cdot C_2^2 \pm 0.76 \text{K}(95\%) \quad (3-28)$$

### Intensity-Ratio Method Results for CCD Camera Set Data

In intensity-ratio method,  $(I_{(x,y)}^{530/10nm}/I_{(x,y)}^{600/10nm})_{run} / (I_{(x,y)}^{530/10nm}/I_{(x,y)}^{600/10nm})_{ref}$  and  $(I_{(x,y)}^{530/10nm}/I_{(x,y)}^{650/10nm})_{run} / (I_{(x,y)}^{530/10nm}/I_{(x,y)}^{650/10nm})_{ref}$  ratio-of-ratios filter data were used for obtaining calibration functions for pressure and temperature. The regression coefficients of fitting for equations (3-29) and (3-30) are 0.999 and 0.998, respectively.

$$P = -2.64 + 0.4111 \cdot X + 23.29 \cdot Y - 39.11 \cdot X \cdot Y + 1.592 \cdot X^2 + 27.47 \cdot Y^2 + 13.93 \cdot X^2 \cdot Y - 5.117 \cdot Y^2 \cdot X - 5.084 \cdot X^2 \cdot Y^2 \pm 0.08 \text{ psi}(95\%) \quad (3-29)$$

$$T = 149.0 + 345.4 \cdot X - 166.5 \cdot Y + 10.78 \cdot X \cdot Y - 150.9 \cdot X^2 + 222.5 \cdot Y^2 + 70.91 \cdot X^2 \cdot Y - 244.1 \cdot Y^2 \cdot X + 60.72 \cdot X^2 \cdot Y^2 \pm 0.62 \text{ K}(95\%) \quad (3-30)$$

Notice that the precision of fit at 95% confidence interval for equations (3-29) and (3-30) is less than that of reported for equations (3-27) and (3-28). If we analyze the imaging results for both methods (Table 3-3), we see that the results determined by intensity-ratio calibration are more accurate than PCA calibration results. Nonetheless, the results estimated by PCA calibration show more sensitivity at high pressures than those obtained by intensity-ratio method. Note that PCA calibration did not utilize any type of target transformation which might have improved the results.

Moreover, PCA calibration functions used only two factors where there were actually three factors that represent the data. Therefore, comparison of accuracies and sensitivities of both methods might not be very appropriate with the information provided in Table 3-3.

Table 3-3: Accuracies of average pressure estimates for intensity-ratio method and PCA method for three-component PSP imaging data.

<b>P(exp)±0.01 psi</b>	<b>PCA calibration</b>			<b>Intensity-ratio calibration</b>		
	P(est)	$\sigma$ (psi)	% error for P	P(est)	$\sigma$ (psi)	% error for P
<b>2.01</b>	2.03	0.05	+1.0	2.01	0.01	0
<b>3.00</b>	2.99	0.04	-0.3	3.00	0.02	0
<b>4.01</b>	3.99	0.04	-0.5	3.99	0.03	-0.5
<b>4.99</b>	4.99	0.04	0	4.99	0.03	0
<b>5.99</b>	5.99	0.05	0	5.98	0.04	-0.2
<b>7.00</b>	7.00	0.05	0	7.00	0.05	0
<b>8.00</b>	7.98	0.06	-0.3	7.97	0.06	-0.4
<b>9.00</b>	9.03	0.06	+0.3	9.02	0.06	+0.2
<b>10.01</b>	10.06	0.08	+0.5	9.99	0.08	-0.2
<b>11.01</b>	11.08	0.07	+0.6	11.05	0.07	+0.4
<b>12.01</b>	12.07	0.07	+0.5	12.00	0.10	-0.1
<b>13.00</b>	13.02	0.07	+0.2	12.99	0.11	-0.1
<b>14.69</b>	14.72	0.10	+0.2	14.69	0.14	0

### Conclusions

In this work, we applied PCA to both spectroscopic and CCD image data of a dual-luminophore and a three-component paint. We compared the results of PCA calibration with intensity-ratio calibration and found out that the former leads to better results for the prediction of pressure for dual-luminophore coating. Temperature prediction accuracy of both methods was similar. It has been shown that PCA method eliminates the problem of overlapped emissions of luminophores by decoupling their emission within PCA framework, and hence leads to improved accuracies and sensitivities in pressure prediction.

The pressure and temperature prediction capability of three-component coating has also been analyzed by PCA and intensity-ratio method. Unlike the results obtained with dual-luminophore coating, intensity-ratio method was found to be better calibration method for three-component PSP data. The most important reason for that is the difficulty in finding the true transformation matrix that will resolve the pressure and

temperature variation in the data. The comparison of the results obtained by dual-luminophore coating and three-component coating reveals that dual-luminophore coating is more sensitive to pressure where three-component coating is more accurate in predicting pressure.

PCA method is computationally demanding, however one can work on the algorithm in order to decrease the amount of time to calculate pressure and temperature surfaces. The use of more factors and fitting the calibration points to higher order polynomials might improve the accuracy of results for both coatings. The temperature correction abilities of dual-luminophore PSP and three-component PSP have been proven to be successful and very promising for wind tunnel PSP applications.

## **Experimental**

### **Preparation of Basecoat and PSP**

The syntheses of poly-t-BS-co-TFEM and Ruphen doped nanospheres was described in Chapter 2. To prepare the primer basecoat, 140 mg of poly-t-BS-co-TFEM and 125 mg of titanium dioxide (Tronox CR-800) were dissolved in 4 mL of  $\text{CH}_2\text{Cl}_2$  and the solution was stirred overnight. The solution was then sprayed at 20 psi with a commercially available airbrush onto pre-cleaned aluminum coupon using air as the propellant. The basecoat was allowed to dry in an oven at 100 °C for 30 min before applying the PSP coat.

For the dual-luminophore PSP coating, 80 mg of poly-t-BS-co-TFEM, 0.45 mg of PtTFPP, and 0.8 mL of Ruphen/PAN acetone solution was mixed together with 3 mL of  $\text{CH}_2\text{Cl}_2$ . For the three-component PSP coat, 75 mg of poly-t-BS-co-TFEM, 0.75 mg of PtTFPP, 0.3 mL of Ruphen/PAN, and 0.7 mL of Rh110/PAN acetone solutions were mixed together with 3 ml of  $\text{CH}_2\text{Cl}_2$ . The PSP solution was coated onto the substrate in

same manner described for the primer layer and the PSP was then dried at 80 °C for 1 hr. This formulation covered an area of 8 in<sup>2</sup>. A borosilicate microscope glass slide was also coated simultaneously with the coupons in order to allow data to be collected with a fluorescence spectrometer.

### **Fluorimeter Measurements and CCD Imaging**

Steady state emission studies were carried out on a commercially available fluorescence spectrophotometer (SPEX industries, F-112A). Samples were excited at 465 nm. Temperature and pressure were controlled by placing the samples in a home-built chamber. The pressure was controlled with a vacuum pump and monitored with a vacuum gauge (model DPI 260, Druck). Temperature was controlled by a water recirculating bath (model RTE 140, Neslab) and was monitored by a thermocouple. The photoluminescence of the coatings was monitored front-face to the chamber window. The integrated areas under the curves between 535 nm and 580 nm (for Ruphen) and between 635 nm and 680 nm (for PtTFPP) are used for plots.

Full field PSP emission image was collected with a thermoelectrically cooled 14-bit CCD camera with 512 x 512 resolution (Photometrics, Model CH250). The sample was illuminated with an array of blue-LEDs which has an emission maximum at 465 nm. The images were collected through 530/10 nm (03 FIV 111, from Melles Griot), 550/40 nm (03 FIV 044, from Melles Griot), 600/10 nm (03 FIV 046, from Melles Griot), 650/10 nm (03 FIV 048, from Melles Griot), and 700/10 nm (03 FIV 058, from Melles Griot) bandpass filters. The experimental setup is shown in Figure 3-5.

The dual-luminophore PSP and the three-component PSP coated coupons were placed in a vacuum chamber within which pressure can be controlled from 0.6 psi to 14.7 psi. The bottom of the coupon was cooled with a water recirculating temperature

controller while the top was heated in order to form a temperature gradient across the coupon. The thermocouples were located on the back of the coupon as their positions are illustrated by 'X' marks shown in Figure 3-5. A filter wheel was positioned in front of CCD camera. Special care was taken to not displace the camera when switching the filters in the filter wheel. Initially, images were taken at constant pressure and temperature by using the filters mentioned above. Those images were used as reference images. The CCD shutter was opened for a sufficient time (10 – 50 msec, depending on the filter used) to obtain an optimum signal-to-noise ratio. Then, dark images were collected with the same exposure times with the LED illumination off. After that, the bottom of the coupon was cooled while the top was heated. When the temperature gradient was stabilized, the pressure varied in the vacuum chamber to collect images. For each pressure, four images were collected with four filters. For dual-luminophore PSP, 550/40 nm, 600/10 nm, 650/10 nm, and 700/10 filters were used, whereas for the three-component PSP, 530/10 nm, 550/40 nm, 600/10 nm, 650/10 nm filters were placed in the filter wheel. To obtain ratio images for dual-luminophore PSP, raw filter images were subtracted from dark images and then ratioed to the corresponding reference filter images. In most cases image registration was not needed because the object and camera were fixed securely during the experiments. However, in some cases slight (sub-pixel) registration improved the quality of the ratioed images. In these cases, the image registration toolbox (projective transformation) in Matlab was utilized to ensure the correct alignment of images. Finally, the ratioed images were subjected to spatial filtering (Matlab imfilter command, 10 x 10 pixels). Image registration for three-component PSP images was almost the same, though in some cases, the 530/10 nm

images were used as reference images to obtain ratio-of-ratios images. More information regarding the image registration of three-component PSP was provided previously in this chapter.

Within each of the resulting ratioed images there are five specific locations where the temperature is known (at the positions where the thermocouples are located, see “X”s in Figure 3-5). Since images were obtained at 13 different pressures using four different bandpass filters, this gives rise to  $5 \times 13 = 65$  known pressure/temperature conditions at which  $I_{\text{ref}}/I$  can be calibrated for each of the four dual-luminophore PSP emission wavelengths (this gives a data matrix consisting of 4 wavelengths and 65 unique pressure/temperature combinations). The  $I_{\text{ref}}/I$  values for each of the unique conditions was taken as a single pixel in the image at the location in the CCD image matrix corresponding to the thermocouple position on the surface of the coupon.

## CHAPTER 4 SUMMARY AND CONCLUSIONS

Pressure sensitive paint is a powerful tool for the aerodynamic community to acquire full field pressure distributions on aerodynamic models. PSP technique is not only important for the amount of data that are collected in wind tunnel experiments, but also it significantly reduces the time and cost of the experiments compared to loads analyses. However, the technique has some drawbacks, the most important one being temperature interference in pressure estimation. The second most of important disadvantage of PSP technique is image registration which might be difficult to achieve for some PSP experiments. The origin of temperature dependency of PSP, image registration problem, and some other shortcomings of PSP technology have been discussed in detail in Chapter 1.

The most successful approach to the temperature problem is introducing a temperature sensitive luminophore in PSP coating along with a pressure sensitive luminophore which can be used to measure temperature variation concurrently with pressure variation. Afterwards, correction to the PSL response is made by using temperature information in the coating. Similarly, image registration problem can be eliminated by using a reference luminophore again in PSP coating which is neither temperature nor pressure sensitive.

Although there are some promising coatings (such as dual-luminophore PSPs and self-referencing PSPs) reported in the literature that can be used in wind tunnel testing in this context, correcting temperature interference and registering images are still an area of

active research. We developed several multi-luminophore coatings in order to solve the weaknesses of PSPs. Chapter 2 mainly discusses the development, characterization, and spectroscopic properties of multi-luminophore PSPs. The key approach in developing those coatings is co-precipitation of Ruphen and of Rh110 in PAN nanospheres, and then dispersing these nanospheres along with PtTFPP in a novel polymer binder, poly-t-BS-co-TFEM. This technique enabled us to develop one-component, dual-luminophore, self-referencing, and three-component PSPs. The PtTFPP / poly-t-BS-co-TFEM coating showed high sensitivity for pressure ( $B = 0.90$ ) between vacuum and atmospheric pressure with small temperature dependence ( $-0.53\%-\text{°C}^{-1}$ ). The coating also displayed ideal behavior. Dual-luminophore PSP is obtained by dispersing Ruphen/PAN with PtTFPP in poly-t-BS-co-TFEM. Ruphen emission displays high temperature sensitivity ( $\sim -1.4\%-\text{°C}^{-1}$ ) and small pressure sensitivity ( $B = 0.09$ ) where PtTFPP exhibits a B value of  $\sim 0.6$  with significant non-linearity of SV plot and a temperature dependence of  $\sim -1.1\%$  per Celsius. Ruphen emission overlaps with PtTFPP emission causing an increase in temperature dependence and a decrease in pressure sensitivity at 650 nm region. Rh110/PAN is used along with PtTFPP in self-referencing PSP formulation.  $I(525\text{ nm}) / I(650\text{ nm})$  ratio emission increases by 6-fold when going from vacuum to ambient pressure and percent temperature dependence of  $I(650\text{ nm}) / I(525\text{ nm})$  ratio is  $-0.63\%-\text{°C}^{-1}$ . Three-component PSP is formulated by dispersing Ruphen/PAN, Rh110/PAN, and PtTFPP in poly-t-BS-co-TFEM. PtTFPP emission decreases by 4-fold between vacuum and atmospheric conditions. Temperature dependence of  $I(570\text{ nm}) / I(525\text{ nm})$  and of  $I(650\text{ nm}) / I(525\text{ nm})$  at constant temperature are  $-0.81\%-\text{°C}^{-1}$  and

-0.87%·°C<sup>-1</sup>, respectively. All of the coatings showed high photo- and temporal stability which are very essential for wind tunnel experiments.

The PSP properties of coatings indicate that all of the coatings developed in this study can be used in PSP applications. One-component PSP and self-referencing PSP have high sensitivity to pressure with low temperature dependence. Besides, self-referencing PSP has the potential for eliminating the requirement for image registration. Dual-luminophore and three-component PSPs account for temperature variation of PSP response, which enables the correction to the erroneous pressure response induced by temperature. Similar to self-referencing PSP, three-component PSP also employs internal referencing.

The ultimate aim of this project was to develop and to test a dual-luminophore PSP to correct the temperature interference in PSPs. We have two different formulations that can be utilized for this purpose: a dual-luminophore PSP and a three-component PSP. Both of them can provide the temperature information of the PSP coating. The application of these coatings to imaging and the data reduction techniques are described in Chapter 3. We investigated both of the PSPs in a vacuum chamber by inducing a temperature gradient across a PSP coated coupon, and imaging the sample by using a CCD camera through color bandpass filters. Although testing a coupon in a vacuum test chamber is not the same as the experiments performed in a wind tunnel, both of the PSPs demonstrated useful properties which suggest their suitability for PSP applications. The collected dual-luminophore PSP imaging data was analyzed by using intensity-ratio method initially. Then, a method based on principal component analysis was used for data reduction which yielded better results in pressure estimation. The application of

PCA method to PSP imaging is achieved for the first time with our study. The PtTFPP-Ruphen/PAN / poly-t-BS-co-TFEM coating was able to predict pressures within 0.5% of its actual value with a maximum standard deviation of 0.05 psi with PCA method. Average error in temperature prediction was only 0.2 °C. The PtTFPP-Ruphen/PAN-Rh110/PAN / poly-t-BS-co-TFEM coating used ratio-of-ratios for image registration. Intensity-ratio method was found to be a better technique for analysis of three-component PSP data. The temperature and pressure sensitivity was not as good as dual-luminophore coating; however, the results were more accurate in predicting pressure.

In summary, both dual-luminophore and three-component PSPs developed in this study are suitable for PSP applications to correct temperature interference. However, there are some possible improvements that can be done for the formulations of these coatings. As mentioned in several places in the previous chapters, emission overlap of the dyes decreases sensitivity of pressure and temperature measurements for dual-luminophore and three-component PSPs. We used PCA algorithm to eliminate this setback for dual luminophore coating imaging data; however, the same approach did not improve the results much for three-component PSP imaging data. The best solution to this problem would be using other luminophores that are spectrally resolved. There are several directions that can be pursued to correct this shortcoming and some other setbacks described in Chapter 1. A couple of them are given in the sections below.

### **Future Directions**

#### **PtTFPL / Poly-t-BS-co-TFEM**

As we stated in many places in this work, the main problem of dual-luminophore and three-component PSPs developed in our lab is the emission overlap of the dyes that causes negative effect in the pressure and temperature sensitivities of the coatings. One

can resolve this problem by choosing other luminophores that emit at different part of the spectrum so that the luminophore emissions are spectrally resolved. Then, intensity-ratio method would be applied as the data reduction method which is much easier to implement than PCA calibration method. One of the best candidates in this context is PtTFPL (Figure 1-5),<sup>37</sup> which emits at 740 nm and displays similar pressure sensitivity as PtTFPP. The pressure response of PtTFPL / poly-t-BS-co-TFEM coating is given in Figure 4-1.

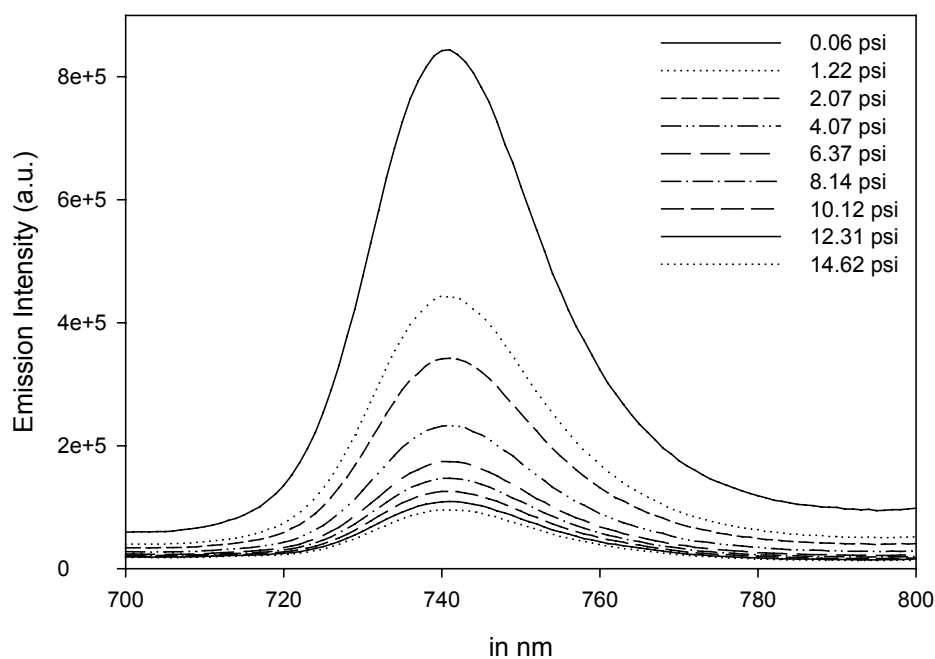


Figure 4-1: Pressure response of PtTFPL / poly-t-BS-co-TFEM coating at 294.5 K.

Stern-Volmer plots obtained at different temperatures are shown in Figure 4-2. PtTFPL emission decreases 10-fold between vacuum and atmospheric pressure. The temperature dependence of the coating is  $-0.69\% \cdot ^\circ\text{C}^{-1}$ , and is independent of pressure

(ideal coating). Furthermore, PtTFPL is more photostable than PtTFPP in similar environments.

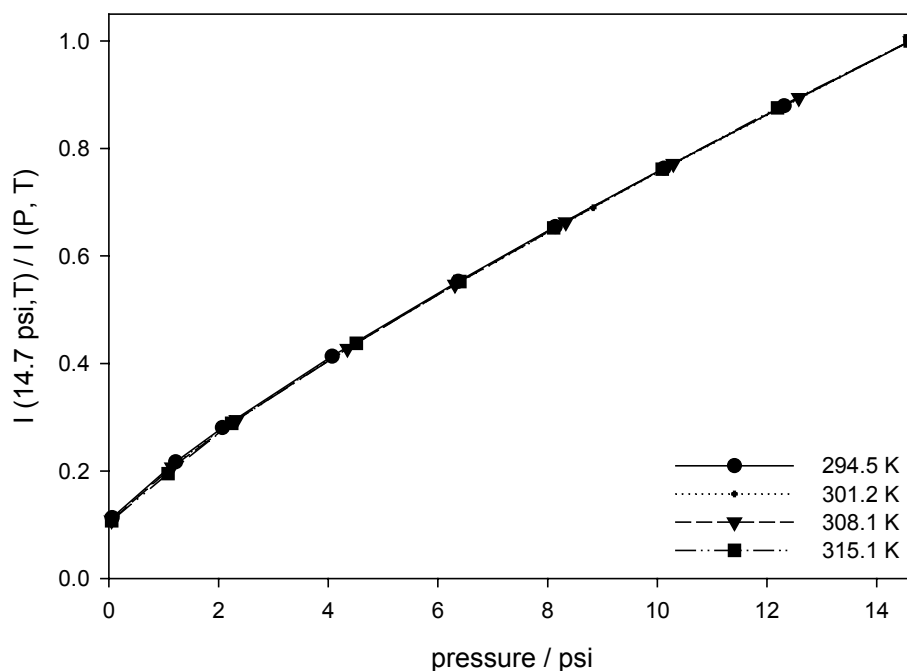


Figure 4-2: Stern-Volmer plots obtained at various temperatures. PtTFPL emission is integrated over an area of 720 nm and 760 nm.

Since PSP properties of PtTFPL in poly-t-BS-co-TFEM coating are very similar to those for PtTFPP / poly-t-BS-co-TFEM coating, PtTFPP can be replaced by PtTFPL in the multi-luminophore coatings that we developed in this work. However, the major drawback of PtTFPL is its synthesis difficulty and high cost.<sup>37</sup> PtTFPL is synthesized in two steps with very low yields and the starting materials are also expensive. Unless a more robust synthesis scheme is developed, its application in PSP experiments will be limited. Other PSLs that emit at the same spectral region are either very long lived or less photostable.

### PtTFPP - DAP3 / Poly-*t*-BS-co-TFEM

The luminophore encapsulation technique that we described in this study is easy and robust. Nevertheless, it would be desired to formulate a dual-luminophore coating by simply dispersing TSL and PSL in the same polymer matrix. We have developed such a coating in our lab by using 5-(*p*-dimethylaminophenyl)-2-phenyl-2,4-pentadienenitrile (DAP3) as TSL and PtTFPP as PSL. The excimer emission of DAP3 is temperature dependent ( $\sim -1.45\% \cdot ^\circ\text{C}^{-1}$ ). The chemical structure of DAP3, excimer emission, and the temperature response is shown Figure 4-3.

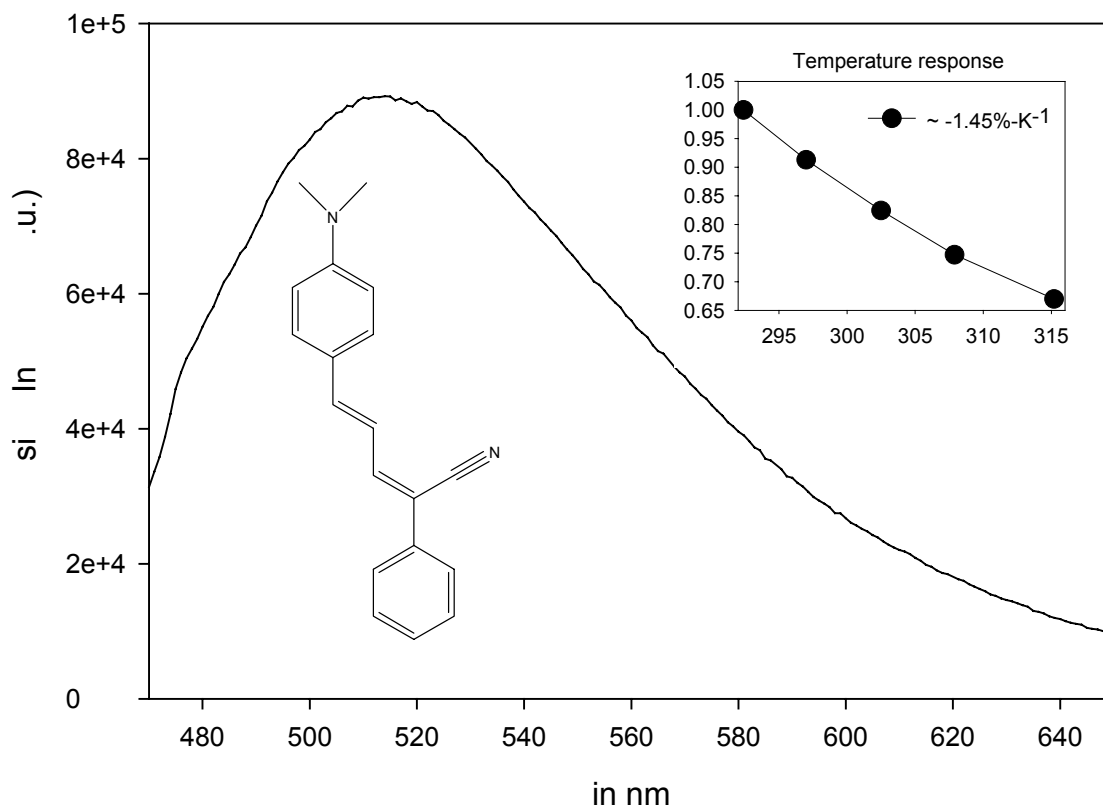


Figure 4-3: Excimer emission and chemical structure of DAP3. Inset – The temperature response of DAP3 / poly-*t*-BS-co-TFEM coating at 14.7 psi.

The pressure response of PtTFPP-DAP3 / poly-t-BS-co-TFEM coating is shown in Figure 4-4. The structured DAP3 emission is caused by Q absorption bands of PtTFPP. Emissions from both luminophores are spectrally resolved.

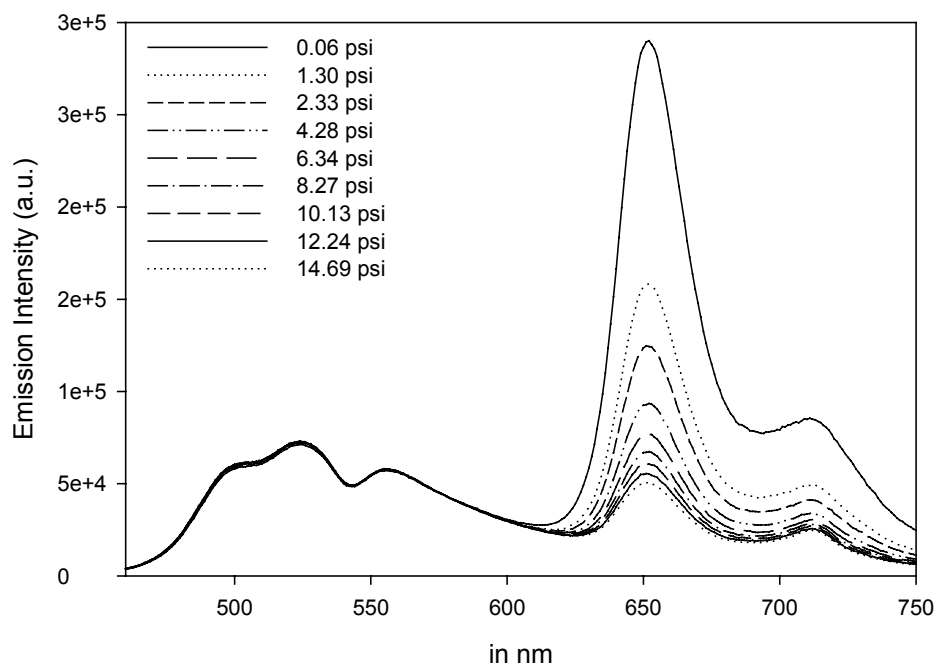


Figure 4-4: The pressure response of PtTFPP-DAP3 / poly-t-BS-co-TFEM coating at constant T.

The Stern-Volmer plot of the coating's response is given in Figure 4-5. PtTFPP response is not as sensitive as one would expect and Stern-Volmer plot corresponding to PtTFPP emission is curving substantially. These results indicate that there is significant interaction between DAP3 and PtTFPP in the matrix. Nonetheless, both pressure and temperature sensitivities of this coating are satisfactory for PSP applications. The major drawback of this coating, however, is the fast sublimation rate of DAP3 from the polymer matrix. DAP3 emission decreases by  $\sim 3\% \cdot \text{hr}^{-1}$  at room temperature. At higher temperatures, the DAP3 evaporates much faster. On the other hand, one can retard the

sublimation of DAP3 by either dispersing DAP3 in primer layer along with TiO<sub>2</sub> or by using it in a new (TSP) layer between primer and active layer. It might be then possible to achieve stable enough emission from DAP3 that would allow wind tunnel applications.

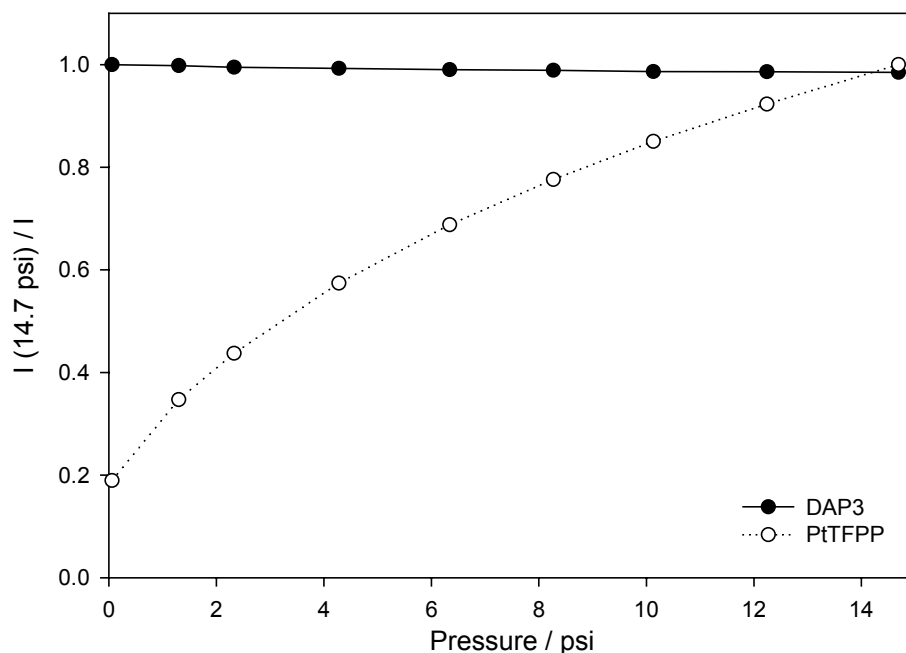


Figure 4-5: Stern-Volmer plots for PtTFPP and DAP3 emissions. PtTFPP emission is integrated over an area of 635 nm and 670 nm, where DAP3 emission is integrated over an area of 500 nm and 550 nm.

#### **PtTFPP-Pyrene / Poly-IBM-co-TFEM**

The PSP properties PtTFPP-pyrene / poly-IBM-co-TFEM coating are very similar in nature to PtTFPP-DAP3 / poly-IBM-co-TFEM coating. In this formulation, excimer emission of pyrene is temperature dependent. Interestingly, pyrene excimer emission intensity increases with temperature for this coating (Figure 4-6 and 4-7). Temperature dependence of pyrene is  $+0.39\% \cdot ^\circ\text{C}^{-1}$  where temperature dependence of PtTFPP is  $-1.15\% \cdot ^\circ\text{C}^{-1}$  in poly-IBM-co-TFEM.

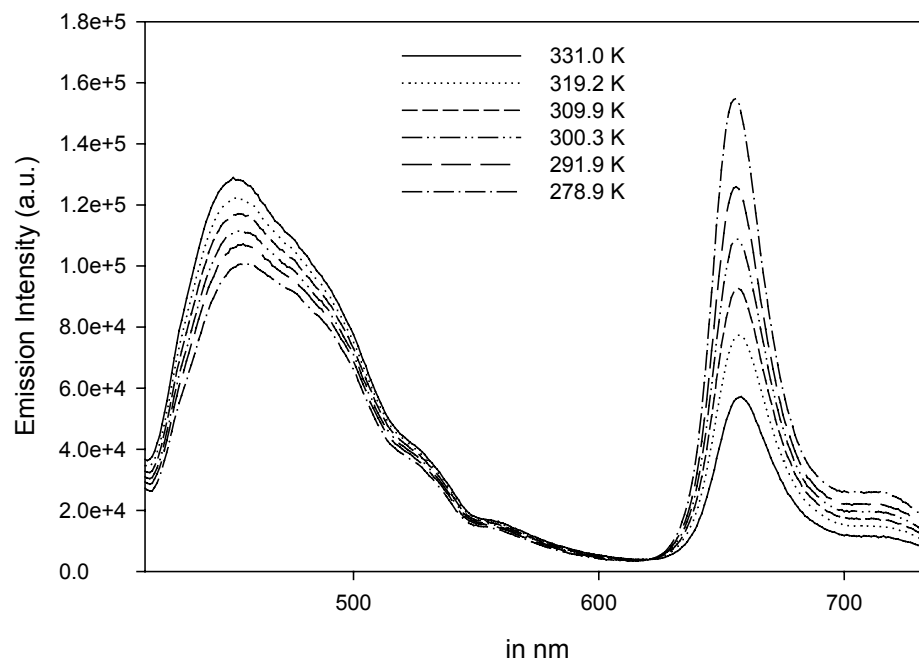


Figure 4-6: Temperature response of PtTFPP-pyrene / poly-IBM-co-TFEM coating at 14.7 psi.

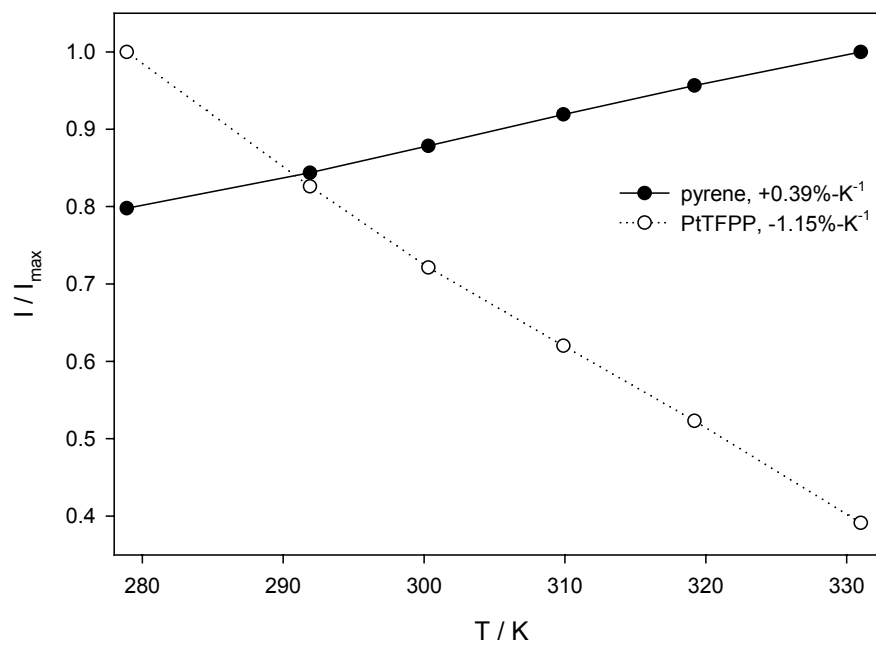


Figure 4-7: Intensity variation plots of PtTFPP and pyrene emissions with temperature at 14.7 psi.

Pyrene excimer emission is not pressure dependent and PtTFPP displays high and linear response to pressure in poly-IBM-co-TFEM (Figure 4-8 and 4-9). The main problem of this coating is low temporal stability of pyrene emission. Pyrene sublimates at a rate of  $\sim 2\% \text{-hr}^{-1}$  at 298 K, and this rate increases up to  $\sim 10\% \text{-hr}^{-1}$  at 331 K. As we suggested in previous section for PtTFPP-DAP3 / poly-t-BS-co-TFEM coating, pyrene can be dispersed in the primer layer or in another layer between primer and active layer, so that the evaporation rate would be diminished enough to utilize the coating in wind tunnel studies.

Chemical attachment of pyrene to polymer backbone might also solve the sublimation problem. Nevertheless, the temperature response might change in this case.

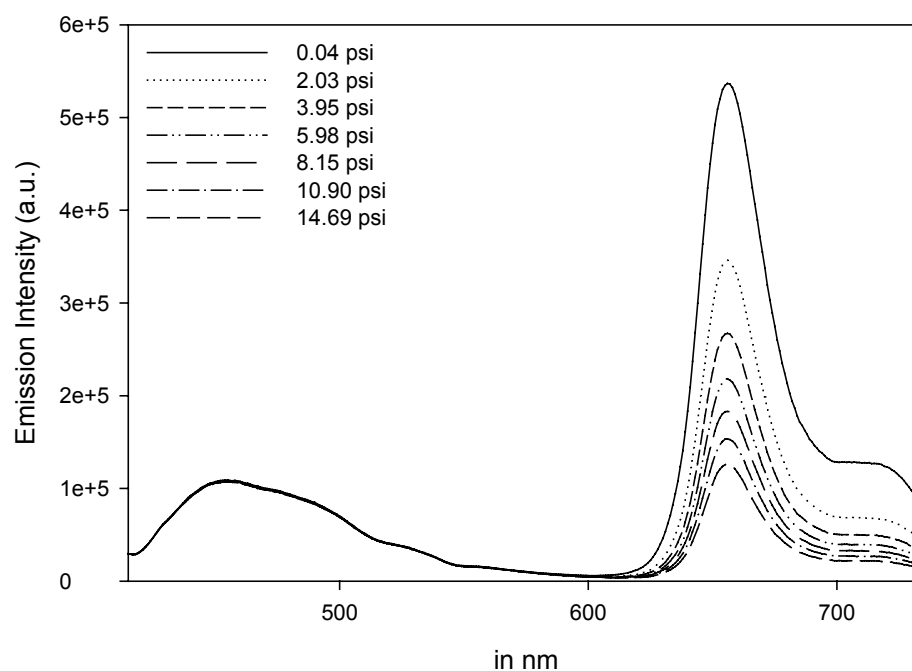


Figure 4-8: Pressure response of PtTFPP-pyrene / poly-IBM-co-TFEM coating at 291.9 K.

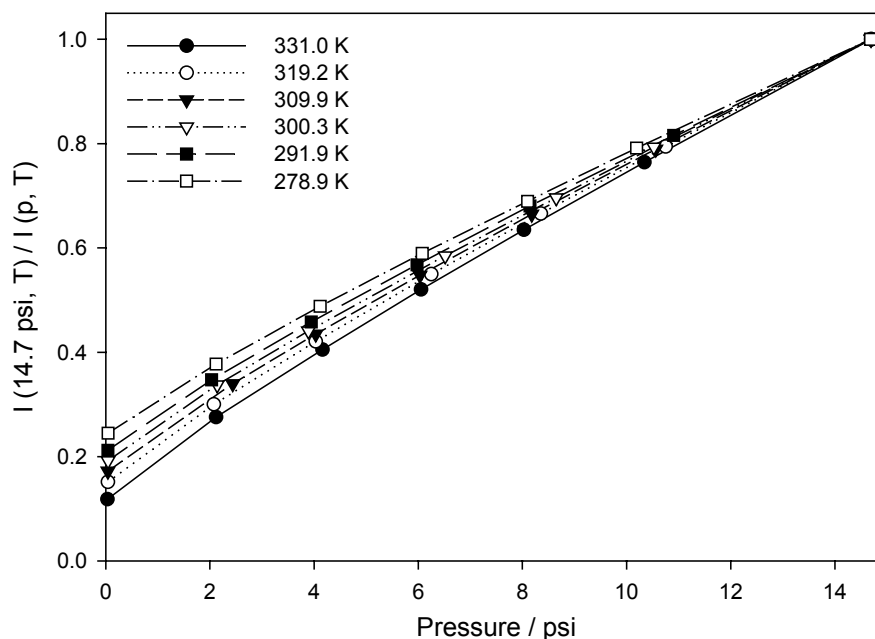


Figure 4-9: Stern-Volmer plots for PtTFPP emission in PtTFPP-pyrene / poly-IBM-co-TFEM coating at various temperatures.

### Temperature Independent PSP

The temperature independent PSP is the ultimate solution to the temperature interference problem seen in wind tunnel applications. We already explained in Chapter 1 the factors that are responsible for temperature dependence of PSPs. The main factor is temperature dependence of oxygen diffusion in the binder, and the second main factor is the variation in the non-radiative decay rate of PSLs with temperature. These factors can be expressed in terms of activation energies which are positive quantities in nature. There is one exception to this rule, the activation energies for permeability of small gases in poly(1-(trimethylsilyl)-1-propyne) (PTMSP) (Figure 4-10) are negative.<sup>87</sup> The activation energy of oxygen permeation in PTMSP is -0.11 kcal/mole. This unusual property of PTMSP is attributed to its large frozen fractional free volume (29%) which is the highest amount reported among the known polymers.<sup>87</sup> Thus, the PtTFPP emission intensity in

PTMSP increases as temperature increases following an opposite trend compared to other polymer binders (Figure 4-11). If we blend PTMSP and another PSP polymer binder (which has a positive activation energy for permeation of oxygen) in correct amounts, the temperature dependence of PtTFPP emission might cancel each other in the blend film since one of the polymers favors an increase in intensity and the other one favors a decrease in intensity.

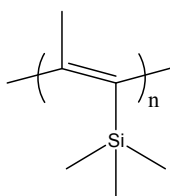


Figure 4-10: Chemical structure of PTMSP.

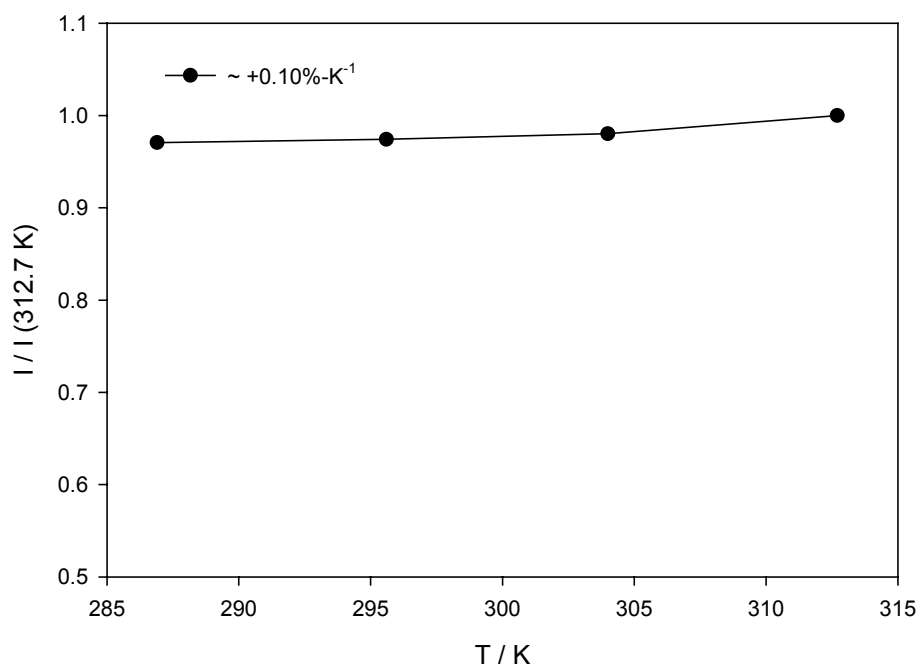


Figure 4-11: The temperature response of PtTFPP in PTMSP binder at 14.7 psi.

To estimate the correct ratio, we also need to consider the magnitude of PtTFPP emission intensities at similar environments. PtTFPP emission decreases by 43-fold between 0.06 psi and 14.7 psi ( $I(0.06 \text{ psi}) / I(14.7 \text{ psi}) = 43$ ) in PtTFPP / PTMSP

coating. The same change is 11-fold for PtTFPP / poly-t-BS-co-TFEM coating. That means, PtTFPP emission is *ca.* 4 times less intense in PTMSP than it is in poly-t-BS-co-TFEM at similar conditions. The temperature dependence of PtTFPP in poly-t-BS-co-TFEM coating is  $-0.53\% \cdot ^\circ\text{C}^{-1}$ , approximately 5 times higher in magnitude than that of PtTFPP / PTMSP coating. Therefore, if PTMSP and poly-t-BS-co-TFEM is blended in 20:1 ratio, then the blend film should show temperature independent pressure response assuming that PtTFPP is partitioned according to polymer ratios in two polymer components in the blend film.

Along with our predictions, PtTFPP / PTMSP – poly-t-BS-co-TFEM (14:1) shows almost no temperature dependence at all (Figure 4-12). The temperature response fluctuates within 1% of total emission intensity over a large temperature range. The Stern-Volmer plot of PtTFPP emission is displayed in Figure 4-13.

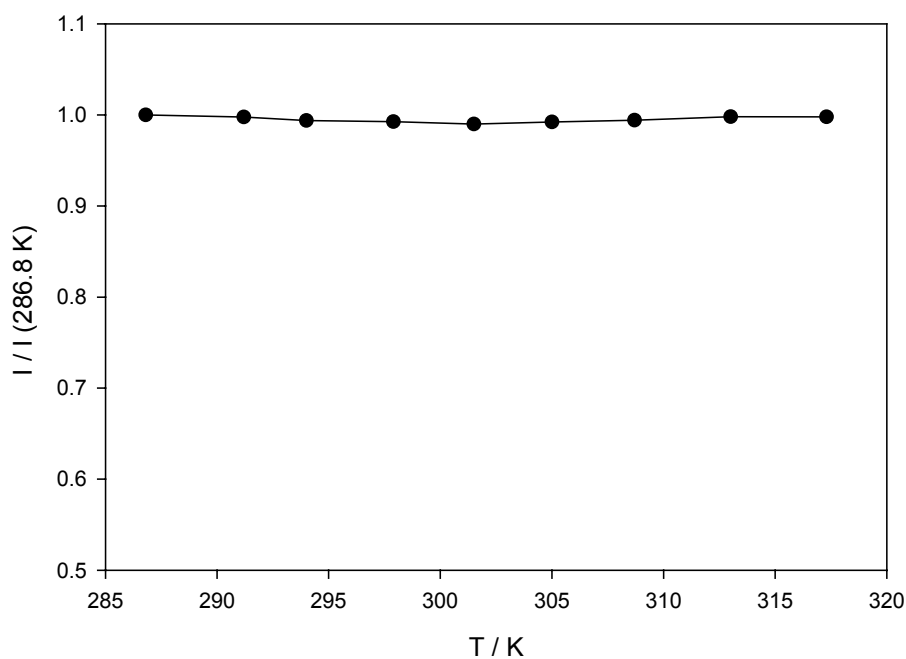


Figure 4-12: PtTFPP emission intensity variation with temperature at constant pressure for PtTFPP / PTMSP - poly-t-BS-co-TFEM coating.

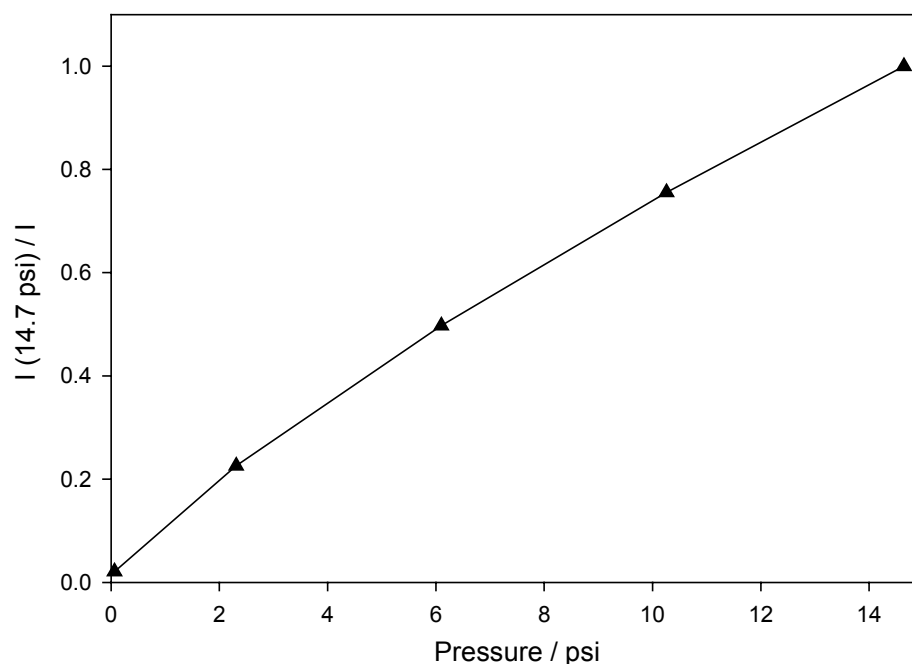


Figure 4-13: Stern-Volmer plot for PtTFPP emission for PtTFPP / PTMSP - poly-t-BS-co-TFEM coating at 307.2 K.

All these results are very promising for achieving a temperature-independent PSP formulation. Nonetheless, there are two drawbacks of this coating. One of them is low luminescence at high pressures which adversely affects SNR. The second drawback is fast-aging of polymer film with a rate at  $3\% \cdot \text{hr}^{-1}$ . The first drawback might be prevented by choosing another luminophore which has a smaller lifetime than PtTFPP ( $60 \mu\text{s}$  in  $\text{CH}_2\text{Cl}_2$ , quantum yield = 0.088), thus this new luminophore would be quenched less, resulting in high intensities at ambient conditions. One candidate in this perspective is PtTF<sub>28</sub>PP (Figure 4-14), which is a porphyrin fluorinated analog of PtTFPP. PtTF<sub>28</sub>PP has a lifetime of  $5.8 \mu\text{s}$  in  $\text{CH}_2\text{Cl}_2$  (quantum yield = 0.043) and it is more photostable than PtTFPP.<sup>45</sup> Fast-aging of PTMSP might also be prevented by choosing  $\text{NbCl}_5$  as the catalyst in the polymerization reaction of TMSP monomer rather than  $\text{TaCl}_5$ . It is known that  $\text{NbCl}_5$  catalyzed PTMSP batches display little aging problems.<sup>87</sup>

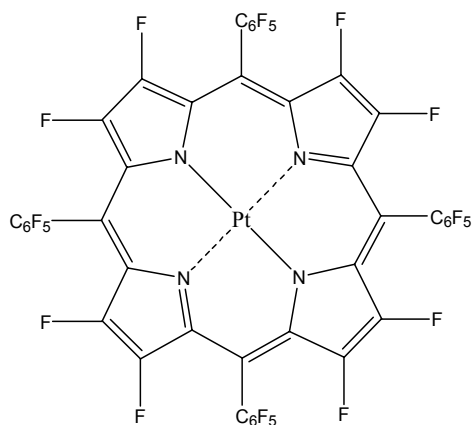


Figure 4-14: Chemical structure of PtTF<sub>28</sub>PP.

If achieved, temperature independent PSP would be a breakthrough in PSP research. The most promising lead seems to be using PTMSP - poly-t-BS-co-TFEM based blend films as binder and PtTF<sub>28</sub>PP as PSL in temperature-independent PSP formulation. Nevertheless, other PSLs might also be used in the blends films of PTMSP and poly-t-BS-co-TFEM. At present, this is the focus of active research in our lab.

APPENDIX A  
MATLAB MACROS

**% ---Program to calculate eigenvalues and eigenvectors with PCA method from  
% spectroscopic data set of PtTFPP- Ruphen/PAN / poly-t-BS-co-TFEM coating---**

**% Loading D matrix**

```
clear
load rPANhomoa.txt;
D=rPANhomoa(3:213,2:41);
Wavelength=rPANhomoa(3:213,1);
[m,n]=size(D);
```

**% Calculating covariance matrix**

```
Lambda1=0;
RR=zeros(n,n);
Z=D'*D;
CC=zeros(m,n); Rc=zeros(m,n); HH=zeros(m,n); e=1; Vec=0;
p=1;
while e > 0
    if p > 1
        Z=RR;
    end
```

**% Calculating eigenvectors and eigenvalues**

```
RR=Z-Lambda1*Vec*Vec';
[Q,Lambda]=eig(RR);
Lambda1=max(max(Lambda));
if p == 1
    maxii=Lambda1;
end

for y=1:n
    for t=1:n
        if Lambda1 == Lambda(t,y);
            x=y;
        end
    end
end
end
Vec=Q(:,x);
```

**% Terminating the loop if the eigenvalue is less than 0.001 of the maximum  
%eigenvalue**

```

if Lambda1 > maxii*0.001
    HH=D*Q;
    Rc(:,p)=HH(:,x);
    CC(p,:)=Vec';
else
    e=0;
end
p=p+1;
end

```

**% Reconstructing the R & C matrices**

```

R=zeros(m,p-2);
C=zeros(p-2,n);
for aa=1:p-2
    R(:,aa)=Rc(:,aa);
    C(aa,:)=CC(aa,:);
end
R;
C;

```

**% Target transformation**

```

R1=R;
C1=C;
for phii=343.8:343.8
    phi=phii*pi/180;
    T=[0.11*cos(phi) -0.12*sin(phi); 0.54*sin(phi) 0.24*cos(phi)];
R=R1*T;
C=inv(T)*C1;

```

**% Displaying figures**

```

figure(1)
plot(Wavelength,D)
title('Raw Data, D')
xlabel('Wavelength (nm)')
ylabel('Emission Intensity (a.u)'); axis([540 750 0 900000])

```

```

figure(2)
clf
plot(Wavelength,R*C)
title('Reconstructed Spectra, D''')
xlabel('Wavelength (nm)')
ylabel('Emission Intensity (a.u)'); axis([540 750 0 900000])

```

```

figure(3)
clf
x1x=[322.6 312.1 302.7 292.9 282.1];
x1xa=[322.6 322.6 322.6 322.6 322.6 322.6 322.6 322.6;
      312.1 312.1 312.1 312.1 312.1 312.1 312.1 312.1;
      302.7 302.7 302.7 302.7 302.7 302.7 302.7 302.7;
      292.9 292.9 292.9 292.9 292.9 292.9 292.9 292.9;
      282.1 282.1 282.1 282.1 282.1 282.1 282.1 282.1];

y1yr=[1.19 2.1 4.24 6.2 8.18 10.25 12.09 14.691;
      0.97 2.22 4.22 6.17 8.39 10.56 12.07 14.686;
      1.22 2.08 4.05 6.33 8.81 10.13 12.4 14.683;
      1.08 2.15 4.14 6.025 8.3 10.08 12.15 14.681;
      1.18 2.02 4.1 6.08 8.59 9.99 12.15 14.679];

for i=1:8
    y1y(1,i)=sum(y1yr(1:5,i))/5;
end

CC=[C(1,1:8); C(1,9:16); C(1,17:24); C(1,25:32); C(1,33:40)];
surf(y1y,x1x,CC)
xlabel('Pressure (psi)');
ylabel('Temperature (K)');
title('Eigenvector 1');

figure(4);
CC=[C(2,1:8); C(2,9:16); C(2,17:24); C(2,25:32); C(2,33:40)];
surf(y1y,x1x,CC)
xlabel('Pressure (psi)');
ylabel('Temperature (K)');
title('Eigenvector 2');

figure(5);
CC1=[C(1,1:8); C(1,9:16); C(1,17:24); C(1,25:32); C(1,33:40)];
CC2=[C(2,1:8); C(2,9:16); C(2,17:24); C(2,25:32); C(2,33:40)];
surf(CC1,CC2,x1xa)
xlabel('Eigenvector 1');
ylabel('Eigenvector 2');
title('Temperature (K)');

figure(6);
CC1=[C(1,1:8); C(1,9:16); C(1,17:24); C(1,25:32); C(1,33:40)];
CC2=[C(2,1:8); C(2,9:16); C(2,17:24); C(2,25:32); C(2,33:40)];
surf(CC1,CC2,y1yr)
xlabel('Eigenvector 1');
ylabel('Eigenvector 2');

```

```

title('Pressure (psi)');

figure(7)
plot(Wavelength,R)
title('Fundamental Spectra')
xlabel('Wavelength (nm)')
ylabel('Emission Intensity (a.u)'); axis([540 750 0 900000])
grid on

figure(8)
plot(Wavelength,R(:,1)*C(1,:))
title('R1*C1')
xlabel('Wavelength (nm)')
ylabel('Emission Intensity (a.u)'); axis([540 750 0 900000])

figure(9)
plot(Wavelength,R(:,2)*C(2,:))
title('R2*C2')
xlabel('Wavelength (nm)')
ylabel('Emission Intensity (a.u)'); axis([540 750 0 900000])

figure(10)
CC=[C(1,1:8); C(1,9:16); C(1,17:24); C(1,25:32); C(1,33:40)];
surf(y1yr,x1x,CC.^-1)
xlabel('Pressure (psi)');
ylabel('Temperature (K)');
title('1/Eigenvector 1');

figure(11)
CC3=[C(1,1:8); C(1,9:16); C(1,17:24); C(1,25:32); C(1,33:40)];
CC4=[C(2,1:8); C(2,9:16); C(2,17:24); C(2,25:32); C(2,33:40)];
surf(CC3.^-1,CC4,y1yr)
xlabel('1/Eigenvector 1');
ylabel('Eigenvector 2');
title('Pressure (psi)');

F=C';

if abs(F(1,1))-abs(F(2,1)) < 0.002
    a=1;
    b=2;
else
    a=2;
    b=1;
end

```

```

for i=0:7
    hk=F(i+1:8:40,b);
    FF(i*5+1:i*5+5)=hk;
end

```

```

figure(12)
plot(FF,'ro-')
grid on

```

```

figure(13)
plot(F(:,a),'ro-')
grid on

```

```

phii;
pause(0.5)
end

```

---

```

% ---Program to calculate pressure and temperature calibration surfaces for
% PtTFPP- Ruphen/PAN / poly-t-BS-co-TFEM coating imaging data with PCA
% method---

```

```

% The macro shown below can be used to calculate the pressure and temperature
% surface of one single condition.

```

```

% Loading raw images for each filter

```

```

clear
F44_1=imread('rPAN/c1rPAN_44_01.tif');
F46_1=imread('rPAN/c1rPAN_46_01.tif');
F48_1=imread('rPAN/c1rPAN_48_01.tif');
F58_1=imread('rPAN/c1rPAN_58_01.tif');
F44dk=imread('rPAN/c1rPAN_44_dark.tif');
F46dk=imread('rPAN/c1rPAN_46_dark.tif');
F48dk=imread('rPAN/c1rPAN_48_dark.tif');
F58dk=imread('rPAN/c1rPAN_58_dark.tif');
F44ref=imread('rPAN/c1rPAN_44_ref.tif');
F46ref=imread('rPAN/c1rPAN_46_ref.tif');
F48ref=imread('rPAN/c1rPAN_48_ref.tif');
F58ref=imread('rPAN/c1rPAN_58_ref.tif');

```

```

% Converting the uint8 array type files to double array format

```

```

a1=30; a2=490; a3=150; a4=420;
F44_1a=double(F44_1(a1:a2,a3:a4));
F46_1a=double(F46_1(a1:a2,a3:a4));
F48_1a=double(F48_1(a1:a2,a3:a4));

```

```

F58_1a=double(F58_1(a1:a2,a3:a4));
F44dka=double(F44dk(17:442,22:252));
F46dka=double(F46dk(17:442,22:252));
F48dka=double(F48dk(17:442,22:252));
F58dka=double(F58dk(17:442,22:252));
F44refa=double(F44ref(a1:a2,a3:a4));
F46refa=double(F46ref(a1:a2,a3:a4));
F48refa=double(F48ref(a1:a2,a3:a4));
F58refa=double(F58ref(a1:a2,a3:a4));
[m,n]=size(F44_1a);

```

**% Image Registration (alternatively, image registration toolbox in Matlab can also be used)**

**% Set image search parameters**

```

ccol = m/2.; % Center col
crow = n/2.; % Center row
maxshift = 5; % User-defined region to shift "search"
rref = F44refa(maxshift+1:m-maxshift,crow); % Reference row
cref = F44refa(ccol,maxshift+1:n-maxshift); % Reference col

```

**% Determine approximate whole pixel shift based on a correlation target function**

**% Whole pixel column shift**

```

r44_1 = F44_1a(:,crow);
stdevmin = 100000.;
corrmin = 0.;
for i = -maxshift:maxshift
    temp = r44_1(maxshift+1+i:m-maxshift+i);
    corr = sum(temp.*rref)/sqrt(sum(temp.*temp)*sum(rref.*rref));
    if corr > corrmin
        cshift44_1 = i;
        corrmin = corr;
    end
end
end

```

**% Whole pixel row shift**

```

c44_1 = F44_1a(ccol+cshift44_1,:);
stdevmin = 100000.;
corrmin = 0.;
for i = -maxshift:maxshift
    temp = c44_1(maxshift+1+i:n-maxshift+i);
    corr = sum(temp.*cref)/sqrt(sum(temp.*temp)*sum(cref.*cref));
    if corr > corrmin
        rshift44_1 = i;
        corrmin = corr;
    end
end

```

```

end
[m,n]=size(F46_1a);

% Set image search parameters
ccol = m/2.;           % Center col
crow = n/2.;          % Center row
maxshift = 5;         % User-defined region to shift "search"
rref = F46refa(maxshift+1:m-maxshift,crow); % Reference row
cref = F46refa(ccol,maxshift+1:n-maxshift); % Reference col

% Determine approximate whole pixel shift based on a correlation target function
% Whole pixel column shift
r46_1 = F46_1a(:,crow);
stdevmin = 100000.;
corrmin = 0.;
for i = -maxshift:maxshift
    temp = r46_1(maxshift+1+i:m-maxshift+i);
    corr = sum(temp.*rref)/sqrt(sum(temp.*temp)*sum(rref.*rref));
    if corr > corrmin
        cshift46_1 = i;
        corrmin = corr;
    end
end
[m,n]=size(F48_1a);

% Whole pixel row shift
c46_1 = F46_1a(ccol+cshift46_1,:);
stdevmin = 100000.;
corrmin = 0.;
for i = -maxshift:maxshift
    temp = c46_1(maxshift+1+i:n-maxshift+i);
    corr = sum(temp.*cref)/sqrt(sum(temp.*temp)*sum(cref.*cref));
    if corr > corrmin
        rshift46_1 = i;
        corrmin = corr;
    end
end

% Set image search parameters
ccol = m/2.;           % Center col
crow = n/2.;          % Center row
maxshift = 5;         % User-defined region to shift "search"
rref = F48refa(maxshift+1:m-maxshift,crow); % Reference row
cref = F48refa(ccol,maxshift+1:n-maxshift); % Reference col

% Determine approximate whole pixel shift based on a correlation target function

```

**% Whole pixel column shift**

```

r48_1 = F48_1a(:,crow);
stdevmin = 100000.;
corrmin = 0.;
for i = -maxshift:maxshift
    temp = r48_1(maxshift+1+i:m-maxshift+i);
    corr = sum(temp.*rref)/sqrt(sum(temp.*temp)*sum(rref.*rref));
    if corr > corrmin
        cshift48_1 = i;
        corrmin = corr;
    end
end
end

```

**% Whole pixel row shift**

```

c48_1 = F48_1a(ccol+cshift48_1,:);
stdevmin = 100000.;
corrmin = 0.;
for i = -maxshift:maxshift
    temp = c48_1(maxshift+1+i:n-maxshift+i);
    corr = sum(temp.*cref)/sqrt(sum(temp.*temp)*sum(cref.*cref));
    if corr > corrmin
        rshift48_1 = i;
        corrmin = corr;
    end
end
end
[m,n]=size(F58_1a);

```

**% Set image search parameters**

```

ccol = m/2.; % Center col
crow = n/2.; % Center row
maxshift = 5; % User-defined region to shift "search"
rref = F58refa(maxshift+1:m-maxshift,crow); % Reference row
cref = F58refa(ccol,maxshift+1:n-maxshift); % Reference col

```

**% Determine approximate whole pixel shift based on a correlation target function****% Whole pixel column shift**

```

r58_1 = F58_1a(:,crow);
stdevmin = 100000.;
corrmin = 0.;
for i = -maxshift:maxshift
    temp = r58_1(maxshift+1+i:m-maxshift+i);
    corr = sum(temp.*rref)/sqrt(sum(temp.*temp)*sum(rref.*rref));
    if corr > corrmin
        cshift58_1 = i;
        corrmin = corr;
    end
end

```

end

**% Whole pixel row shift**

```
c58_1 = F58_1a(ccol+cshift58_1,:);
stdevmin = 100000.;
corrmin = 0.;
for i = -maxshift:maxshift
    temp = c58_1(maxshift+1+i:n-maxshift+i);
    corr = sum(temp.*cref)/sqrt(sum(temp.*temp)*sum(cref.*cref));
    if corr > corrmin
        rshift58_1 = i;
        corrmin = corr;
    end
end
end
```

**% Registering 1 psi filter images with reference image**

```
b1=17; b2=442; b3=22; b4=252;
F44_1b=F44_1a(b1+cshift44_1:b2+cshift44_1,b3+rshift44_1:b4+rshift44_1);
F44_refb=F44refa(b1:b2,b3:b4);
```

```
c1=17; c2=442; c3=23; c4=253;
F46_1b=F46_1a(c1+cshift46_1:c2+cshift46_1,c3+rshift46_1:c4+rshift46_1);
F46_refb=F46refa(c1:c2,c3:c4);
```

```
d1=17; d2=442; d3=24; d4=254;
F48_1b=F48_1a(d1+cshift48_1:d2+cshift48_1,d3+rshift48_1:d4+rshift48_1);
F48_refb=F48refa(d1:d2,d3:d4);
```

```
e1=17; e2=442; e3=22; e4=252;
F58_1b=F58_1a(e1+cshift58_1:e2+cshift58_1,e3+rshift58_1:e4+rshift58_1);
F58_refb=F58refa(e1:e2,e3:e4);
```

**% Finding  $I_{ref}/I$  values for all pressures – subtracting dark image**

```
F44_1c=(F44_refb-F44dka)/(F44_1b-F44dka);
F46_1c=(F46_refb-F46dka)/(F46_1b-F46dka);
F48_1c=(F48_refb-F48dka)/(F48_1b-F48dka);
F58_1c=(F58_refb-F58dka)/(F58_1b-F58dka);
```

**% Image filtering - smoothening surface**

```
h=ones(10,10)/100;
F44_1d=imfilter(F44_1c,h);
F46_1d=imfilter(F46_1c,h);
F48_1d=imfilter(F48_1c,h);
F58_1d=imfilter(F58_1c,h);
```

**% Finding average  $I_{ref}/I$  values at thermocouple locations for calibration data**

```

d=215; e=116;
c1twoup_44=sum((sum(F44_1d(d-184:d-175,e-4:e+5))))/100;
c1twoup_46=sum((sum(F46_1d(d-184:d-175,e-4:e+5))))/100;
c1twoup_48=sum((sum(F48_1d(d-184:d-175,e-4:e+5))))/100;
c1twoup_58=sum((sum(F58_1d(d-184:d-175,e-4:e+5))))/100;
c1oneup_44=sum((sum(F44_1d(d-94:d-85,e-4:e+5))))/100;
c1oneup_46=sum((sum(F46_1d(d-94:d-85,e-4:e+5))))/100;
c1oneup_48=sum((sum(F48_1d(d-94:d-85,e-4:e+5))))/100;
c1oneup_58=sum((sum(F58_1d(d-94:d-85,e-4:e+5))))/100;
c1_44=sum((sum(F44_1d(d-4:d+5,e-4:e+5))))/100;
c1_46=sum((sum(F46_1d(d-4:d+5,e-4:e+5))))/100;
c1_48=sum((sum(F48_1d(d-4:d+5,e-4:e+5))))/100;
c1_58=sum((sum(F58_1d(d-4:d+5,e-4:e+5))))/100;
c1onedown_44=sum((sum(F44_1d(d+86:d+95,e-4:e+5))))/100;
c1onedown_46=sum((sum(F46_1d(d+86:d+95,e-4:e+5))))/100;
c1onedown_48=sum((sum(F48_1d(d+86:d+95,e-4:e+5))))/100;
c1onedown_58=sum((sum(F58_1d(d+86:d+95,e-4:e+5))))/100;
c1twodown_44=sum((sum(F44_1d(d+176:d+185,e-4:e+5))))/100;
c1twodown_46=sum((sum(F46_1d(d+176:d+185,e-4:e+5))))/100;
c1twodown_48=sum((sum(F48_1d(d+176:d+185,e-4:e+5))))/100;
c1twodown_58=sum((sum(F58_1d(d+176:d+185,e-4:e+5))))/100;
[s1,s2]=size(F44_1d);

```

### **% Estimating pressure and temperature profiles of images at 1 psi with PCA**

#### **%method**

```

pressure01r=zeros(s1,s2);
temperature01r=zeros(s1,s2);

```

#### **% Program to Calculate PCA**

```

for i=1:s1
    for j=1:s2
        load rPAN_PCAs.txt;
        load Csource.txt;
        D=rPAN_PCAs(3:6,2:66);
        D(1,65)=F44_1d(i,j);
        D(2,65)=F46_1d(i,j);
        D(3,65)=F48_1d(i,j);
        D(4,65)=F58_1d(i,j);
        Wavelength=rPAN_PCAs(3:6,1);
    end
end

```

```

[m,n]=size(D);
D;

```

#### **% Calculating the covariance matrix**

```

Lambda1=0;
RR=zeros(n,n);

```

```

Z=D'*D;
CC=zeros(m,n); Rc=zeros(m,n); HH=zeros(m,n); e=1; Vec=0;
p=1;
while e > 0
    if p > 1
        Z=RR;
    end
end

```

**% Calculating the eigenvectors and eigenvalues**

```

RR=Z-Lambda1*Vec*Vec';
[Q,Lambda]=eig(RR);
Lambda1=max(max(Lambda));
if p == 1
    maxii=Lambda1;
end
for y=1:n
    for t=1:n
        if Lambda1 == Lambda(t,y);
            x=y;
        end
    end
end
end
Vec=Q(:,x);

```

**% Terminating the loop if the eigenvalue is less than 0.01 of the maximum**

**% eigenvalue**

```

if Lambda1 > maxii*0.01
    HH=D*Q;
    Rc(:,p)=HH(:,x);
    CC(p,:)=Vec';
else
    e=0;
end
p=p+1;
end

```

**% Reconstructing the R & C matrices**

```

R=zeros(m,p-2);
C=zeros(p-2,n);
for aa=1:p-2
    R(:,aa)=Rc(:,aa);
    C(aa,:)=CC(aa,:);
end
R;
C;

```

**% Target Transformation**

```

R1=R;
C1=C;
for phii=10:10
    phi=phii*pi/180;
    T=[0.11*cos(phi) -0.12*sin(phi); 0.54*sin(phi) 0.24*cos(phi)];
    R=R1*T;
    C=inv(T)*C1;

```

```

Cdiff1=mean2(Csource(1,1:64)-C(1,1:64));
C(1,65)=C(1,65)+Cdiff1;
Cdiff2=mean2(Csource(2,1:64)-C(2,1:64));
C(2,65)=C(2,65)+Cdiff2;

```

```

F=C';
if abs(F(1,1))-abs(F(2,1)) < 0.002
    a=1;
    b=2;
else
    a=2;
    b=1;
end
for mm=0:12
    hk=F(mm+1:13:65,b);
    FF(mm*5+1:mm*5+5)=hk;
end
end

```

**% Calculating pressure and temperature at each pixel – coefficient of the following  
 % equations are exported from least squares fit of calibration data in SigmaPlot  
 % software**

```

P01r = -3.098 + 8.792*C(1,65) - 3.04*C(2,65) - 5.782*C(1,65)*C(2,65) -
2.023*C(1,65)^2 + 2.639*C(1,65)^2*C(2,65) + 15.36*C(2,65)^2 -
20.01*C(2,65)^2*C(1,65) + 7.498*C(1,65)^2*C(2,65)^2;
T01r = 237.3 + 107.8*C(1,65) + 14.16*C(2,65) - 13.52*C(1,65)*C(2,65) -
36.59*C(1,65)^2 + 5.046*C(1,65)^2*C(2,65) - 0.2342*C(2,65)^2 +
2.182*C(2,65)^2*C(1,65) - 1.075*C(1,65)^2*C(2,65)^2;

```

```

pressure01r(i,j)=P01r;
temperature01r(i,j)=T01r;
end
end

```

**% Calculating average pressure and standard deviation for a selected area**

```

mu01=mean2(pressure01r(40:380,40:110));
sigma01=std2(pressure01r(40:380,40:110));

```

**% Displaying pressure and temperature surfaces**

```
figure(1)
imshow(real(pressure01r),[0 17]), colormap(hsv), colorbar, axis image;
title('estimated pressure surface at 1 psi')
figure(2)
imshow(real(temperature01r),[273 323]), colormap(hsv), colorbar, axis image;
title('estimated temperature surface at 1 psi')
```

---

**% Estimating pressure and temperature profiles of images at 1 psi with intensity-ratio method**

```
pressure01r=zeros(s1,s2);
temperature01r=zeros(s1,s2);
```

```
for i=1:s1
    for j=1:s2
```

**% Calculating pressure and temperature at each pixel – coefficient of the following equations are exported from least squares fit of calibration data in SigmaPlot software**

```
P01r=-3.842+5.895*F44_14d(i,j)-0.9596*F48_14d(i,j)-1.332*F44_14d(i,j)*F48_14d(i,j)-
2.323*F44_14d(i,j)^2+41.12*F48_14d(i,j)^2-
35.5*F48_14d(i,j)^2*F44_14d(i,j)+1.553*F48_14d(i,j)*F44_14d(i,j)^2+9.034*F44_14d(
i,j)^2*F48_14d(i,j)^2;
T01r=261.3+48.88*F44_14d(i,j)-54.55*F48_14d(i,j)+75.3*F44_14d(i,j)*F48_14d(i,j)-
7.381*F44_14d(i,j)^2+18.56*F48_14d(i,j)^2-30.21*F48_14d(i,j)^2*F44_14d(i,j)-
28.62*F48_14d(i,j)*F44_14d(i,j)^2+11.64*F44_14d(i,j)^2*F48_14d(i,j)^2;
```

```
pressure01r(i,j)=P01r;
temperature01r(i,j)=T01r;
```

```
end
end
```

**% Calculating average pressure and standard deviation for a selected area**

```
mu1=mean2(pressure01r(50:385,50:188));
sigma1=std2(pressure01r(50:385,50:188));
```

**% Displaying pressure and temperature surfaces**

```
figure(1)
imshow(real(pressure01r),[0 17]), colormap(hsv), colorbar, axis image;
title('estimated pressure at 1 psi')
```

```
figure(2)
imshow(real(temperature01r),[273 323]), colormap(hsv), colorbar, axis image;
title('estimated temperature at 1 psi')
```

APPENDIX B  
APPLICATION OF PCA TO A SAMPLE DATA SET

This appendix shows a simple tutorial regarding the application of principal component analysis to a small hypothetical data set. The mathematical steps shown below are aimed to demonstrate how PCA works in a general sense.

1) Construct a hypothetical data set based on two factors.

$$d_{ik} = x_{i1}y_{1k} + x_{i2}y_{2k}$$

$$\begin{bmatrix} 0 & 4 \\ 1 & -1 \\ 2 & 0 \\ 3 & 0 \\ 4 & 3 \\ 5 & -4 \\ 6 & 5 \\ 7 & 8 \\ 8 & -2 \\ 9 & -5 \end{bmatrix} \times \begin{bmatrix} 2 & 5 & 2 \\ 1 & 10 & -5 \end{bmatrix} = \begin{bmatrix} 4 & 40 & -20 \\ 1 & -5 & 7 \\ 4 & 10 & 4 \\ 6 & 15 & 6 \\ 11 & 50 & -7 \\ 6 & -15 & 30 \\ 17 & 80 & -13 \\ 22 & 115 & -26 \\ 14 & 20 & 26 \\ 13 & -5 & 43 \end{bmatrix}$$

**X**

**Y**

**D**

Row Matrix

Column Matrix

Data Matrix

We will deconvolute **D** matrix with PCA and try to find **X** and **Y** matrices.

2) Find the covariance matrix:

$$Z = D'D = \begin{bmatrix} 1364 & 4850 & 212 \\ 4850 & 24725 & -5230 \\ 212 & -5230 & 4820 \end{bmatrix}$$

Covariance matrix has a size 3 X 3, that means it should give 3 eigenvalues and 3 corresponding eigenvectors.

3) Calculate the first eigenvalue and the eigenvector by iteration:

$$ZC_1 = \lambda_1 C_1$$

Choose an arbitrary eigenvector for  $C_1$ .

$$C_1' = [0.57735 \quad 0.57735 \quad 0.57735]$$

$$\begin{bmatrix} 1364 & 4850 & 212 \\ 4850 & 24725 & -5230 \\ 212 & -5230 & 4820 \end{bmatrix} \begin{bmatrix} 0.57735 \\ 0.57735 \\ 0.57735 \end{bmatrix} = \begin{bmatrix} 3710.0 \\ 14055.6 \\ -114.3 \end{bmatrix} = 14537.4 \begin{bmatrix} 0.25520 \\ 0.96686 \\ -0.00786 \end{bmatrix}$$

When  $\begin{bmatrix} 3710.0 \\ 14055.6 \\ -114.3 \end{bmatrix}$  is normalized, we get  $14537.4 \begin{bmatrix} 0.25520 \\ 0.96686 \\ -0.00786 \end{bmatrix}$ . If we continue in this

fashion for the rest of the iteration steps, we can find the eigenvalue and the eigenvector when the  $ZC_1 = \lambda_1 C_1$  condition is satisfied.

$$\begin{bmatrix} 1364 & 4850 & 212 \\ 4850 & 24725 & -5230 \\ 212 & -5230 & 4820 \end{bmatrix} \begin{bmatrix} 0.25520 \\ 0.96686 \\ -0.00786 \end{bmatrix} = \begin{bmatrix} 5035.7 \\ 25184.4 \\ -5040.5 \end{bmatrix} = 26172.9 \begin{bmatrix} 0.19240 \\ 0.96223 \\ -0.19258 \end{bmatrix}$$

$$\begin{bmatrix} 1364 & 4850 & 212 \\ 4850 & 24725 & -5230 \\ 212 & -5230 & 4820 \end{bmatrix} \begin{bmatrix} 0.19240 \\ 0.96223 \\ -0.19258 \end{bmatrix} = \begin{bmatrix} 4888.4 \\ 25731.5 \\ -5919.9 \end{bmatrix} = 26852.4 \begin{bmatrix} 0.18204 \\ 0.95825 \\ -0.22046 \end{bmatrix}$$

$$\begin{bmatrix} 1364 & 4850 & 212 \\ 4850 & 24725 & -5230 \\ 212 & -5230 & 4820 \end{bmatrix} \begin{bmatrix} 0.18204 \\ 0.95825 \\ -0.22046 \end{bmatrix} = \begin{bmatrix} 4849.1 \\ 25728.6 \\ -6035.7 \end{bmatrix} = 26868.2 \begin{bmatrix} 0.18047 \\ 0.95758 \\ -0.22464 \end{bmatrix}$$

$$\begin{bmatrix} 1364 & 4850 & 212 \\ 4850 & 24725 & -5230 \\ 212 & -5230 & 4820 \end{bmatrix} \begin{bmatrix} 0.18047 \\ 0.95758 \\ -0.22464 \end{bmatrix} = \begin{bmatrix} 4842.8 \\ 25726.3 \\ -6052.6 \end{bmatrix} = 26868.7 \begin{bmatrix} 0.18024 \\ 0.95748 \\ -0.22526 \end{bmatrix}$$

$$\begin{bmatrix} 1364 & 4850 & 212 \\ 4850 & 24725 & -5230 \\ 212 & -5230 & 4820 \end{bmatrix} \begin{bmatrix} 0.18024 \\ 0.95748 \\ -0.22526 \end{bmatrix} = \begin{bmatrix} 4841.9 \\ 25726.0 \\ -6055.2 \end{bmatrix} = 26868.9 \begin{bmatrix} 0.18020 \\ 0.95746 \\ -0.22536 \end{bmatrix}$$

$$\begin{bmatrix} 1364 & 4850 & 212 \\ 4850 & 24725 & -5230 \\ 212 & -5230 & 4820 \end{bmatrix} \begin{bmatrix} 0.18020 \\ 0.95746 \\ -0.22536 \end{bmatrix} = \begin{bmatrix} 4841.9 \\ 25726.0 \\ -6055.2 \end{bmatrix} = 26868.9 \begin{bmatrix} 0.18020 \\ 0.95746 \\ -0.22536 \end{bmatrix}$$

$ZC_1 = \lambda_1 C_1$  condition is met. Therefore, the first eigenvalue and eigenvector is:

$$\lambda_1 = 26868.9$$

$$C_1' = [0.18020 \quad 0.95746 \quad -0.22536]$$

4) Subtract the contribution of first factor from covariance matrix. Calculate the second eigenvalue and the eigenvector by using iteration again:

$$\mathfrak{R}_1 = Z - \lambda_1 C_1 C_1'$$

$$\mathfrak{R}_1 = \begin{bmatrix} 1364 & 4850 & 212 \\ 4850 & 24725 & -5230 \\ 212 & -5230 & 4820 \end{bmatrix} - 26868.9 \begin{bmatrix} 0.18020 \\ 0.95746 \\ -0.22536 \end{bmatrix} [0.18020 \quad 0.95746 \quad -0.22536]$$

$$\mathfrak{R}_1 = \begin{bmatrix} 1364 & 4850 & 212 \\ 4850 & 24725 & -5230 \\ 212 & -5230 & 4820 \end{bmatrix} - \begin{bmatrix} 872.49 & 4635.82 & -1091.21 \\ 4635.82 & 24631.67 & -5797.91 \\ -1091.21 & -5797.91 & 1364.74 \end{bmatrix} = \begin{bmatrix} 491.51 & 214.18 & 1303.21 \\ 214.18 & 93.33 & 567.91 \\ 1303.21 & 567.91 & 3455.26 \end{bmatrix}$$

$$\mathfrak{R}_1 C_2 = \lambda_2 C_2$$

After iteration we get:

$$\lambda_2 = 4040.2$$

$$C_2' = [0.34878 \quad 0.15200 \quad 0.92479]$$

5) Subtract contribution of second factor from  $\mathfrak{R}_1$ . Then, calculate the third eigenvalue and the eigenvector by using  $\mathfrak{R}_2$ .

$$\mathfrak{R}_2 = \mathfrak{R}_1 - \lambda_2 C_2 C_2'$$

$$\mathfrak{R}_2 = \begin{bmatrix} 0.0 & 0.0 & 0.1 \\ 0.0 & 0.0 & 0.0 \\ 0.1 & 0.0 & 0.0 \end{bmatrix}$$

The residual,  $\mathfrak{R}_2$  is essentially zero. There is no need to carry out calculations for another factor. Therefore, we can conclude that there are only two factors for this data set.

6) Then abstract column matrix is:

$$C_{abstract} = \begin{bmatrix} C_1' \\ C_2' \end{bmatrix} = \begin{bmatrix} 0.18020 & 0.95746 & -0.22536 \\ 0.34878 & 0.15200 & 0.92479 \end{bmatrix}$$

Eigenvectors are orthogonal. One can multiply them with each other for testing purposes.

$$C_1' C_2 = 0.18020 \times 0.34878 + 0.95746 \times 0.15200 - 0.22536 \times 0.92479 = -0.0000348$$

7) Abstract row matrix is:

$$R_{abstract} = DC' = [r_1 \quad r_2] = \begin{bmatrix} 4 & 40 & -20 \\ 1 & -5 & 7 \\ 4 & 10 & 4 \\ 6 & 15 & 6 \\ 11 & 50 & -7 \\ 6 & -15 & 30 \\ 17 & 80 & -13 \\ 22 & 115 & -26 \\ 14 & 20 & 26 \\ 13 & -5 & 43 \end{bmatrix} \times \begin{bmatrix} 0.18020 & 0.34878 \\ 0.95746 & 0.15200 \\ -0.22536 & 0.92479 \end{bmatrix} = \begin{bmatrix} 43.5267 & -11.0207 \\ -6.1847 & 6.0624 \\ 9.3939 & 6.6143 \\ 14.0909 & 9.9214 \\ 51.4330 & 4.9630 \\ -20.0419 & 27.5564 \\ 82.5903 & 6.0669 \\ 119.9323 & 1.1084 \\ 15.8124 & 31.9674 \\ -12.1357 & 43.5401 \end{bmatrix}$$

We can reproduce the **D** matrix by using  $R_{abstract}$  and  $C_{abstract}$ . For instance;  $d_{72} = 80$  can be calculated as shown below:

$$82.5903 \times 0.95746 + 6.0669 \times 0.15200 = 79.9990$$

**8)** Now we can find **X** and **Y** matrices by choosing a proper target transformation matrix. Since we do not have any prior knowledge about **X** and **Y**, it is hard to determine the true transformation matrix. We can use the following transformation matrix (which is the true transformation matrix):

$$T = \begin{bmatrix} 0.0563012 & 0.0675947 \\ 0.2223760 & -0.0960138 \end{bmatrix}$$

$$T^{-1} = \begin{bmatrix} 4.6980 & 3.3075 \\ 10.8810 & -2.7545 \end{bmatrix}$$

$$D' = XY = RTT^{-1}C$$

$$X = RT$$

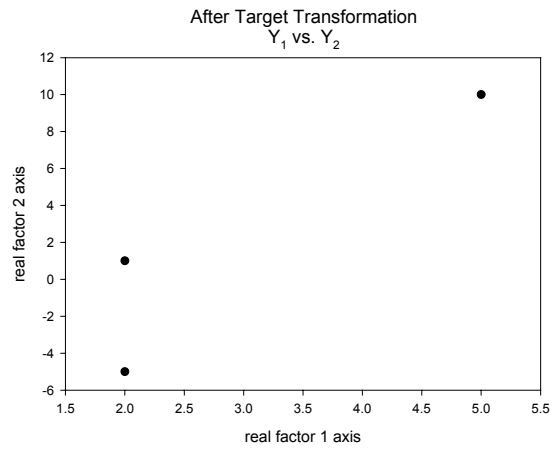
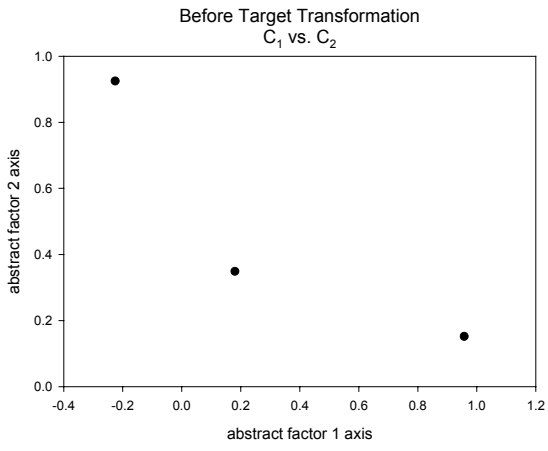
$$Y = T^{-1}C$$

Calculate **X** and **Y**.

$$X = RT = \begin{bmatrix} 43.5267 & -11.0207 \\ -6.1847 & 6.0624 \\ 9.3939 & 6.6143 \\ 14.0909 & 9.9214 \\ 51.4330 & 4.9630 \\ -20.0419 & 27.5564 \\ 82.5903 & 6.0669 \\ 119.9323 & 1.1084 \\ 15.8124 & 31.9674 \\ -12.1357 & 43.5401 \end{bmatrix} \times \begin{bmatrix} 0.0563012 & 0.0675947 \\ 0.2223760 & -0.0960138 \end{bmatrix} = \begin{bmatrix} 0.0 & 4.0 \\ 1.0 & -1.0 \\ 2.0 & 0 \\ 3.0 & 0 \\ 4.0 & 3.0 \\ 5.0 & -4.0 \\ 6.0 & 5.0 \\ 7.0 & 8.0 \\ 8.0 & -2.0 \\ 9.0 & -5.0 \end{bmatrix}$$

$$Y = T^{-1}C = \begin{bmatrix} 4.6980 & 3.3075 \\ 10.8810 & -2.7545 \end{bmatrix} \begin{bmatrix} 0.18020 & 0.95746 & -0.22536 \\ 0.34878 & 0.15200 & 0.92479 \end{bmatrix} = \begin{bmatrix} 2.0002 & 5.0009 & 1.9999 \\ 1.0000 & 9.9995 & -4.9996 \end{bmatrix}$$

**9)** Graphical presentation of eigenvector rotation in factor space.



## LIST OF REFERENCES

- (1) Kavandi, J.; Callis, J.; Gouterman, M.; Khalil, G.; Wright, D.; Green, E.; Burns, D.; McLachlan, B. Luminescent barometry in wind tunnels. *Review of Scientific Instruments* **1990**, *61*, 3340-3347.
- (2) Fujii, K.; Tsuboi, N.; Fujimatsu, N. Visualization of jet flows over a plate by pressure-sensitive paint experiments and comparison with CFD. *Annals of the New York Academy of Sciences* **2002**, *972*, 265-270.
- (3) Bell, J. H.; Schairer, E. T.; Hand, L. A.; Mehta, R. D. Surface pressure measurements using luminescent coatings. *Annual Review of Fluid Mechanics* **2001**, *33*, 155-206.
- (4) Liu, T.; Campbell, B. T.; Burns, S. P.; Sullivan, J. P. Temperature- and pressure-sensitive luminescent paints in aerodynamics. *Applied Mechanics Review* **1997**, *50*, 227-246.
- (5) Sellers, M. Pressure sensitive paint development at Arnold Engineering Development Center. *Sixth Annual Pressure Sensitive Paint Workshop*: Seattle, Washington, 1998.
- (6) Gouterman, M. Oxygen quenching of luminescence of pressure sensitive paint for wind tunnel research. *Journal of Chemical Education* **1997**, *74*, 697-702.
- (7) Peterson, J. I.; Fitzgerald, R. V. New technique of surface flow visualization based on oxygen quenching of fluorescence. *Review of Scientific Instruments* **1980**, *51*, 670-671.
- (8) Kelley-Wickemeyer, R. Pressure paint keynote. *Sixth Annual Pressure Sensitive Paint Workshop*: Seattle, Washington, 1998.
- (9) Morris, M. J.; Donovan, J. F.; Kegelman, J. T.; Schwab, S. D.; Levy, R. L.; Crites, R. C. Aerodynamic applications of pressure sensitive paint. *AIAA Journal* **1993**, *31*, 419-425.
- (10) Brown, O. -Low speed- pressure sensitive paint research. *Sixth Annual Pressure Sensitive Paint Workshop*: Seattle, Washington, 1998.
- (11) Schanze, K. S.; Carroll, B. F.; Korotkevitch, S.; Morris, M. J. Temperature dependence of pressure sensitive paints. *AIAA Journal* **1997**, *35*, 306-310.

- (12) Puklin, E.; Carlson, B.; Gouin, S.; Costin, C.; Green, E.; Ponomarev, S.; Tanji, H.; Gouterman, M. Ideality of pressure-sensitive paint. I. Platinum tetra(pentafluorophenyl)porphine in fluoroacrylic polymer. *Journal of Applied Polymer Science* **2000**, *77*, 2795-2804.
- (13) Lakowicz, J. R. *Principles of Fluorescence Spectroscopy*; 2nd ed.; Kluwer Academic/Plenum Publishers: New York, 1999.
- (14) Gouin, S.; Gouterman, M. Ideality of pressure-sensitive paint. IV. Improvement of luminescence behavior by addition of pigment. *Journal of Applied Polymer Science* **2000**, *77*, 2824-2831.
- (15) Gouin, S.; Gouterman, M. Ideality of pressure-sensitive paint. II. Effect of annealing on the temperature dependence of the luminescence. *Journal of Applied Polymer Science* **2000**, *77*, 2805-2814.
- (16) Lu, X.; Han, B.-H.; Winnik, M. A. Characterizing the quenching process for phosphorescent dyes in poly[(n-butylamino)thionyl]phosphazene] films. *Journal of Physical Chemistry B* **2003**, *107*, 13349-13356.
- (17) Bowyer, W. J.; Xu, W.; Demas, J. N. Determining oxygen diffusion coefficients in polymer films by lifetimes of luminescent complexes measured in the frequency domain. *Analytical Chemistry* **2004**, *76*, 4374-4378.
- (18) Kneas, K. A.; Demas, J. N.; Nguyen, B.; Lockhart, A.; Xu, W.; DeGraff, B. A. Method for measuring oxygen diffusion coefficients of polymer films by luminescence quenching. *Analytical Chemistry* **2002**, *74*, 1111-1118.
- (19) Gouin, S.; Gouterman, M. Ideality of pressure-sensitive paint. III. Effect of the base-coat permeability on the luminescence behavior of the sensing layer. *Journal of Applied Polymer Science* **2000**, *77*, 2815-2823.
- (20) Bedlek-Anslow, J. M.; Hubner, J. P.; Carroll, B. F.; Schanze, K. S. Micro-heterogeneous oxygen response in luminescence sensor films. *Langmuir* **2000**, *16*, 9137-9141.
- (21) Xu, W.; McDonough, R. C., III; Langsdorf, B.; Demas, J. N.; DeGraff, B. A. Oxygen sensors based on luminescence quenching: Interactions of metal complexes with the polymer supports. *Analytical Chemistry* **1994**, *66*, 4133-4141.
- (22) Carraway, E. R.; Demas, J. N.; DeGraff, B. A. Luminescence quenching mechanism for microheterogeneous systems. *Analytical Chemistry* **1991**, *63*, 332-336.

- (23) Amao, Y.; Asai, K.; Okura, I. Oxygen sensing based on lifetime of photoexcited triplet state of platinum porphyrin-polystyrene film using time-resolved spectroscopy. *Journal of Porphyrins and Phthalocyanines* **2000**, *4*, 292-299.
- (24) Carraway, E. R.; Demas, J. N.; DeGraff, B. A.; Bacon, J. R. Photophysics and photochemistry of oxygen sensors based on luminescent transition-metal complexes. *Analytical Chemistry* **1991**, *63*, 337-342.
- (25) Mills, A. Controlling the sensitivity of optical oxygen sensors. *Sensors and Actuators, B: Chemical* **1998**, *B51*, 60-68.
- (26) Kneas, K. A.; Xu, W.; Demas, J. N.; DeGraff, B. A. Oxygen sensors based on luminescence quenching: interactions of tris(4,7-diphenyl-1,10-phenanthroline)ruthenium(II) chloride and pyrene with polymer supports. *Applied Spectroscopy* **1997**, *51*, 1346-1351.
- (27) Ruyten, W. Oxygen quenching of PtTFPP in FIB polymer: a sequential process? *Chemical Physics Letters* **2004**, *394*, 101-104.
- (28) Mills, A. Response characteristics of optical sensors for oxygen: a model based on a distribution in  $t_0$  and  $k_q$ . *Analyst (Cambridge, United Kingdom)* **1999**, *124*, 1309-1314.
- (29) Hubner, J. P.; Carroll, B. F. Application of dual sorption theory to pressure-sensitive paints. *AIAA Journal* **1997**, *35*, 1790-1792.
- (30) Demas, J. N.; DeGraff, B. A.; Xu, W. Modeling of luminescence quenching-based sensors: Comparison of multisite and nonlinear gas solubility models. *Analytical Chemistry* **1995**, *67*, 1377-1380.
- (31) Rharbi, Y.; Yekta, A.; Winnik, M. A. A method for measuring oxygen diffusion and oxygen permeation in polymer films based on fluorescence quenching. *Analytical Chemistry* **1999**, *71*, 5045-5053.
- (32) Schappacher, G.; Hartmann, P. Partial analytical solution of a model used for measuring oxygen diffusion coefficients of polymer films by luminescence quenching. *Analytical Chemistry* **2003**, *75*, 4319-4324.
- (33) Jiang, F. Z.; Xu, R.; Wang, D. Y.; Dong, X. D.; Li, G. C. Preparation and properties of novel aerodynamic pressure-sensitive paint via the sol-gel method. *Journal of Materials Research* **2002**, *17*, 1312-1319.
- (34) Bedlek-Anslow, J. M. Development and characterization of luminescent oxygen sensing coatings. In *Department of Chemistry*; University of Florida: Gainesville, 2000.

- (35) Schanze, K. S.; Shen, Y. Luminophores for temperature sensitive coatings. *Sixth Annual Pressure Sensitive Paint Workshop*: Seattle, Washington, 1998.
- (36) Turro, N. J. *Modern Molecular Photochemistry*; University Science Books: Mill Valley, 1991.
- (37) Khalil, G.; Gouterman, M.; Ching, S.; Costin, C.; Coyle, L.; Gouin, S.; Green, E.; Sadilek, M.; Wan, R.; Yearyeen, J.; Zelelow, B. Synthesis and spectroscopic characterization of Ni, Zn, Pd and Pt tetra(pentafluorophenyl)porpholactone with comparisons to Mg, Zn, Y, Pd and Pt metal complexes of tetra(pentafluorophenyl)porphine. *Journal of Porphyrins and Phthalocyanines* **2002**, *6*, 135-145.
- (38) Zelelow, B.; Khalil, G. E.; Phelan, G.; Carlson, B.; Gouterman, M.; Callis, J. B.; Dalton, L. R. Dual luminophor pressure sensitive paint II. Lifetime based measurement of pressure and temperature. *Sensors and Actuators, B: Chemical* **2003**, *B96*, 304-314.
- (39) Mills, A.; Lepre, A. Controlling the response characteristics of luminescent porphyrin plastic film sensors for oxygen. *Analytical Chemistry* **1997**, *69*, 4653-4659.
- (40) Kalyanasundaram, K.; Thomas, J. K. Environmental effects on vibronic band intensities in pyrene monomer fluorescence and their application in studies of micellar systems. *Journal of the American Chemical Society* **1977**, *99*, 2039-2044.
- (41) Ji, H.-F.; Shen, Y.; Hubner, J. P.; Carroll, B. F.; Schmehl, R. H.; Simon, J. A.; Schanze, K. S. Temperature-independent pressure-sensitive paint based on a bichromophoric luminophor. *Applied Spectroscopy* **2000**, *54*, 856-863.
- (42) Lam, S. K.; Chan, M. A.; Lo, D. Characterization of phosphorescence oxygen sensor based on erythrosin B in sol-gel silica in wide pressure and temperature ranges. *Sensors and Actuators, B: Chemical* **2001**, *B73*, 135-141.
- (43) King, K. A.; Spellane, P. J.; Watts, R. J. Excited-state properties of a triply ortho-metalated iridium(III) complex. *Journal of the American Chemical Society* **1985**, *107*, 1431-1432.
- (44) Mills, A. Optical oxygen sensors. Utilizing the luminescence of platinum metals complexes. *Platinum Metals Review* **1997**, *41*, 115-127.
- (45) Lai, S.-W.; Hou, Y.-J.; Che, C.-M.; Pang, H.-L.; Wong, K.-Y.; Chang, C. K.; Zhu, N. Electronic spectroscopy, photophysical properties, and emission quenching studies of an oxidatively robust perfluorinated platinum porphyrin. *Inorganic Chemistry* **2004**, *43*, 3724-3732.

- (46) Gallery, J.; Gouterman, M.; Callis, J.; Khalil, G.; McLachlan, B.; Bell, J. Luminescent thermometry for aerodynamic measurements. *Review of Scientific Instruments* **1994**, *65*, 712-720.
- (47) Liebsch, G.; Klimant, I.; Wolfbeis, O. S. Luminescence lifetime temperature sensing based on sol-gels and poly(acrylonitrile)s dyed with ruthenium metal-ligand complexes. *Advanced Materials (Weinheim, Germany)* **1999**, *11*, 1296-1299.
- (48) Feist, J. P.; Heyes, A. L.; Seefeldt, S. Oxygen quenching of phosphorescence from thermographic phosphors. *Measurement Science and Technology* **2003**, *14*, N17-N20.
- (49) Coyle, L. M.; Gouterman, M. Correcting lifetime measurements for temperature. *Sensors and Actuators, B: Chemical* **1999**, *B61*, 92-99.
- (50) Hradil, J.; Davis, C.; Mongey, K.; McDonagh, C.; MacCraith, B. D. Temperature-corrected pressure-sensitive paint measurements using a single camera and a dual-lifetime approach. *Measurement Science and Technology* **2002**, *13*, 1552-1557.
- (51) Kubin, R. F.; Fletcher, A. N. Fluorescence quantum yields of some rhodamine dyes. *Journal of Luminescence* **1983**, *27*, 455-462.
- (52) Bur, A. J.; Vangel, M. G.; Roth, S. Temperature dependence of fluorescent probes for applications to polymer materials processing. *Applied Spectroscopy* **2002**, *56*, 174-181.
- (53) Berlman, I. B. *Handbook of Fluorescence Spectra of Aromatic Molecules*; Academic Press: New York, 1971.
- (54) Mitsuishi, M.; Kikuchi, S.; Miyashita, T.; Amao, Y. Characterization of an ultrathin polymer optode and its application to temperature sensors based on luminescent europium complexes. *Journal of Materials Chemistry* **2003**, *13*, 2875-2879.
- (55) Levitus, M.; Negri, R. M.; Aramendia, P. F. Rotational relaxation of carbocyanines. Comparative study with the isomerization dynamics. *Journal of Physical Chemistry* **1995**, *99*, 14231-14239.
- (56) Khalil, G. E.; Costin, C.; Crafton, J.; Jones, G.; Grenoble, S.; Gouterman, M.; Callis, J. B.; Dalton, L. R. Dual-luminophor pressure-sensitive paint I. Ratio of reference to sensor giving a small temperature dependency. *Sensors and Actuators, B: Chemical* **2004**, *B97*, 13-21.

- (57) Chan, C.-M.; Chan, M.-Y.; Zhang, M.; Lo, W.; Wong, K.-Y. The performance of oxygen sensing films with ruthenium-adsorbed fumed silica dispersed in silicone rubber. *Analyst (Cambridge, United Kingdom)* **1999**, *124*, 691-694.
- (58) Chu, D. Y.; Thomas, J. K.; Kuczynski, J. Photophysical studies of molecular mobility in polymer films. 1. Oxygen mobility in polymer films monitored by quenching of the triplet-triplet absorption of bromopyrene. *Macromolecules* **1988**, *21*, 2094-2100.
- (59) Morin, A. M.; Xu, W.; Demas, J. N.; DeGraff, B. A. Oxygen sensors based on quenching of tris-(4,7-diphenyl-1,10-phenanthroline)ruthenium(II) in fluorinated polymers. *Journal of Fluorescence* **2000**, *10*, 7-12.
- (60) Amao, Y.; Miyashita, T.; Okura, I. Optical oxygen detection based on luminescence change of metalloporphyrins immobilized in poly(isobutylmethacrylate-co-trifluoroethylmethacrylate) film. *Analytica Chimica Acta* **2000**, *421*, 167-174.
- (61) Amao, Y.; Asai, K.; Miyashita, T.; Okura, I. Photophysical and photochemical properties of optical oxygen pressure sensor of platinum porphyrin-isobutylmethacrylate-trifluoroethylmethacrylate copolymer film. *Polymer Journal (Tokyo)* **1999**, *31*, 1267-1269.
- (62) Amao, Y.; Asai, K.; Miyashita, T.; Okura, I. Novel optical oxygen sensing material: platinum porphyrin-styrene-pentafluorostyrene copolymer film. *Analytical Communications* **1999**, *36*, 367-369.
- (63) Amao, Y.; Asai, K.; Miyashita, T.; Okura, I. Novel optical oxygen pressure sensing materials: platinum porphyrin-styrene-trifluoroethyl methacrylate copolymer film. *Chemistry Letters* **1999**, 1031-1032.
- (64) DiMarco, G.; Lanza, M. Optical solid-state oxygen sensors using metalloporphyrin complexes immobilized in suitable polymeric matrices. *Sensors and Actuators, B: Chemical* **2000**, *B63*, 42-48.
- (65) Ruffolo, R.; Evans, C. E. B.; Liu, X.-H.; Ni, Y.; Pang, Z.; Park, P.; McWilliams, A. R.; Gu, X.; Lu, X.; Yekta, A.; Winnik, M. A.; Manners, I. Phosphorescent oxygen sensors utilizing sulfur-nitrogen-phosphorus polymer matrixes: Synthesis, characterization, and evaluation of poly(thionylphosphazene)-b-poly(tetrahydrofuran) block copolymers. *Analytical Chemistry* **2000**, *72*, 1894-1904.
- (66) Xu, H.; Aylott, J. W.; Kopelman, R.; Miller, T. J.; Philbert, M. A. A real-time ratiometric method for the determination of molecular oxygen inside living cells using sol-gel-based spherical optical nanosensors with applications to rat C6 glioma. *Analytical Chemistry* **2001**, *73*, 4124-4133.

- (67) Zhang, P.; Guo, J.; Wang, Y.; Pang, W. Incorporation of luminescent tris(bipyridine)ruthenium(II) complex in mesoporous silica spheres and their spectroscopic and oxygen-sensing properties. *Materials Letters* **2002**, *53*, 400-405.
- (68) McDonagh, C.; MacCraith, B. D.; McEvoy, A. K. Tailoring of sol-gel films for optical sensing of oxygen in gas and aqueous phase. *Analytical Chemistry* **1998**, *70*, 45-50.
- (69) McDonagh, C.; Kolle, C.; McEvoy, A. K.; Dowling, D. L.; Cafolla, A. A.; Cullen, S. J.; MacCraith, B. D. Phase fluorometric dissolved oxygen sensor. *Sensors and Actuators, B: Chemical* **2001**, *B74*, 124-130.
- (70) Ertekin, K.; Kocak, S.; Sabih Ozer, M.; Aycan, S.; Cetinkaya, B. Enhanced optical oxygen sensing using a newly synthesized ruthenium complex together with oxygen carriers. *Talanta* **2003**, *61*, 573-579.
- (71) Lu, X.; Manners, I.; Winnik, M. A. Polymer/silica composite films as luminescent oxygen sensors. *Macromolecules* **2001**, *34*, 1917-1927.
- (72) Lu, X.; Winnik, M. A. Luminescence quenching in polymer/filler nanocomposite films used in oxygen sensors. *Chemistry of Materials* **2001**, *13*, 3449-3463.
- (73) DeRosa, M. C.; Mosher, P. J.; Evans, C. E. B.; Crutchley, R. J. Iridium(III) complexes as polymer bound oxygen sensors. *Macromolecular Symposia* **2003**, *196*, 235-248.
- (74) DeRosa, M. C.; Mosher, P. J.; Yap, G. P. A.; Focsaneanu, K. S.; Crutchley, R. J.; Evans, C. E. B. Synthesis, characterization, and evaluation of [Ir(ppy)<sub>2</sub>(vpy)Cl] as a polymer-bound oxygen sensor. *Inorganic Chemistry* **2003**, *42*, 4864-4872.
- (75) Hah, H.; Sakai, T.; Asai, K.; Nishide, H. Synthesis of poly(ethynylplatinumporphyrin) and its application as an oxygen pressure-sensitive paint. *Macromolecular Symposia* **2003**, *204*, 27-35.
- (76) Sakamura, Y.; Suzuki, T.; Matsumoto, M.; Masuya, G.; Ikeda, Y. Optical measurements of high-frequency pressure fluctuations using a pressure-sensitive paint and Cassegrain optics. *Measurement Science and Technology* **2002**, *13*, 1591-1598.
- (77) Liu, T.; Teduka, N.; Kameda, M.; Asai, K. Diffusion timescale of porous pressure-sensitive paint. *AIAA Journal* **2001**, *39*, 2400-2402.
- (78) Sakaue, H.; Gregory, J. W.; Sullivan, J. P.; Raghu, S. Porous pressure-sensitive paint for characterizing unsteady flowfields. *AIAA Journal* **2002**, *40*, 1094-1098.

- (79) Merienne, M.-C.; Le Sant, Y.; Ancelle, J.; Soulevant, D. Unsteady pressure measurement instrumentation using anodized-aluminium PSP applied in a transonic wind tunnel. *Measurement Science and Technology* **2004**, *15*, 2349-2360.
- (80) Baron, A. E.; Danielson, J. D. S.; Gouterman, M.; Wan, J. R.; Callis, J. B. Submillisecond response times of oxygen-quenched luminescent coatings. *Review of Scientific Instruments* **1993**, *64*, 3394-3402.
- (81) Sakaue, H.; Sullivan, J. P. Time response of anodized aluminum pressure-sensitive paint. *AIAA Journal* **2001**, *39*, 1944-1949.
- (82) Hubner, J. P.; Carroll, B. F.; Schanze, K. S.; Ji, H.-F.; Holden, M. Temperature- and pressure-sensitive paint measurements in short-duration hypersonic flow. *AIAA Journal* **2001**, *39*, 654.
- (83) Basu, B. J.; Anandan, C.; Rajam, K. S. Study of the mechanism of degradation of pyrene-based pressure sensitive paints. *Sensors and Actuators, B: Chemical* **2003**, *B94*, 257-266.
- (84) Engler, R. H.; Merienne, M.-C.; Klein, C.; Sant, Y. L. Application of PSP in low speed flows. *Aerospace Science and Technology* **2002**, *6*, 313-322.
- (85) Basu, B. J.; Rajam, K. S. Comparison of the oxygen sensor performance of some pyrene derivatives in silicone polymer matrix. *Sensors and Actuators, B: Chemical* **2004**, *B99*, 459-467.
- (86) Basu, B. J.; Thirumurugan, A.; Dinesh, A. R.; Anandan, C.; Rajam, K. S. Optical oxygen sensor coating based on the fluorescence quenching of a new pyrene derivative. *Sensors and Actuators, B: Chemical* **2005**, *B104*, 15-22.
- (87) Nagai, K.; Masuda, T.; Nakagawa, T.; Freeman, B. D.; Pinnau, I. Poly[1-(trimethylsilyl)-1-propyne] and related polymers: synthesis, properties and functions. *Progress in Polymer Science* **2001**, *26*, 721-798.
- (88) Gouterman, M.; Callis, J.; Dalton, L.; Khalil, G.; Mebarki, Y.; Cooper, K. R.; Grenier, M. Dual luminophor pressure-sensitive paint: III. Application to automotive model testing. *Measurement Science and Technology* **2004**, *15*, 1986-1994.
- (89) Woodmansee, M. A.; Dutton, J. C. Treating temperature-sensitivity effects of pressure sensitive paint measurements. *Experiments in Fluids* **1998**, *24*, 163-174.

- (90) Mitsuo, K.; Asai, K.; Hayasaka, M.; Kameda, M. Temperature correction of PSP measurement using dual-luminophor coating. *Journal of Visualization* **2003**, *6*, 213-223.
- (91) Coyle, L. M.; Chapman, D.; Khalil, G.; Schibli, E.; Gouterman, M. Non-monotonic temperature dependence in molecular referenced pressure-sensitive paint (MR-PSP). *Journal of Luminescence* **1999**, *82*, 33-39.
- (92) Harris, J.; Gouterman, M. Thickness effects in referenced pressure sensitive paint. *Sixth Annual Pressure Sensitive Paint Workshop*: Seattle, Washington, 1998.
- (93) McLean, D. Referenced pressure paint and the ratio of ratios. *Sixth Annual Pressure Sensitive Paint Workshop*: Seattle, Washington, 1998.
- (94) Clinehens, G. A.; Dale, G. A. Ultrastable blue-LED illumination sources for PSP applications. *Sixth Annual Pressure Sensitive Paint Workshop*: Seattle, Washington, 1998.
- (95) Schairer, E. T.; Mehta, R. D.; Olsen, M. E. Effects of pressure-sensitive paint on experimentally measured wing forces and pressures. *AIAA Journal* **2002**, *40*, 1830-1838.
- (96) Engler, R. H.; Klein, C.; Trinks, O. Pressure sensitive paint systems for pressure distribution measurements in wind tunnels and turbomachines. *Measurement Science and Technology* **2000**, *11*, 1077-1085.
- (97) Drouillard, T. F.; Linne, M. A.; Goss, L. P.; Gord, J. R.; Fiechtner, G. J. Lifetime measurement and calibration from pressure-sensitive paint luminescence images. *Review of Scientific Instruments* **2003**, *74*, 276-278.
- (98) Abe, S.; Okamoto, K.; Madarame, H. The development of PIV-PSP hybrid system using pressure sensitive particles. *Measurement Science and Technology* **2004**, *15*, 1153-1157.
- (99) Kostov, Y.; Harms, P.; Rao, G.; Pilato, R. S. Ratiometric oxygen sensing: detection of dual-emission ratio through a single emission filter. *Analyst (Cambridge, United Kingdom)* **2000**, *125*, 1175-1178.
- (100) O'Keeffe, G.; MacCraith, B. D.; McEvoy, A. K.; McDonagh, C. M.; McGilp, J. F. Development of a LED-based phase fluorimetric oxygen sensor using evanescent wave excitation of a sol-gel immobilized dye. *Sensors and Actuators, B: Chemical* **1995**, *B29*, 226-230.
- (101) Lachendro, N.; Crafton, J.; Guille, M.; Sullivan, J.; Carney, T.; Stirn, B. Flight test of pressure sensitive/temperature sensitive paint laser scanning system. *Sixth Annual Pressure Sensitive Paint Workshop*: Seattle, Washington, 1998.

- (102) Liu, T.; Radeztsky, R.; Garg, S.; Cattafesta, L. A photogrammetric model deformation system and its integration with pressure paint. *Sixth Annual Pressure Sensitive Paint Workshop*: Seattle, Washington, 1998.
- (103) Weaver, W. L.; Jordan, J. D.; Dale, G. A.; Navarra, K. R. PSP data analysis: From calibration to visualization. *Sixth Annual Pressure Sensitive Paint Workshop*: Seattle, Washington, 1998.
- (104) Liu, T.; Sullivan, J. P. In situ calibration uncertainty of pressure-sensitive paint. *AIAA* **2003**, *41*, 2300-2302.
- (105) Liu, T.; Cattafesta III, L. N.; Radeztsky, R. H.; Burner, A. W. Photogrammetry applied to wind-tunnel testing. *AIAA* **2000**, *38*, 964-971.
- (106) Klein, C. Application of pressure sensitive paint (PSP) for the determination of the instantaneous pressure field of models in a wind tunnel. *Aerospace Science and Technology* **2000**, *4*, 103-109.
- (107) Ruyten, W. M. Self-illumination calibration technique for luminescent paint measurements. *Review of Scientific Instruments* **1997**, *68*, 3452-3457.
- (108) Schairer, E.; Hand, L.; Bell, J.; Mehta, R. Application of pressure-sensitive paint to helicopter rotors. *Sixth Annual Pressure Sensitive Paint Workshop*: Seattle, Washington, 1998.
- (109) Bencic, T.; Khalil, G.; Gouterman, M.; Youngberg, D.; Costin, C. Development of a pressure sensitive paint for use in an icing wind tunnel. *Sixth Annual Pressure Sensitive Paint Workshop*: Seattle, Washington, 1998.
- (110) McGraw, C. M.; Shroff, H.; Khalil, G.; Callis, J. B. The phosphorescence microphone: a device for testing oxygen sensors and films. *Review of Scientific Instruments* **2003**, *74*, 5260-5266.
- (111) Khotimskii, V. S.; Filippova, V. G.; Bryantseva, I. S.; Bondar, V. I.; Shantarovich, V. P.; Yampolskii, Y. P. Synthesis, transport, and sorption properties and free volume of polystyrene derivatives containing Si and F. *Journal of Applied Polymer Science* **2000**, *78*, 1612-1620.
- (112) Kurner, J. M.; Klimant, I.; Krause, C.; Preu, H.; Kunz, W.; Wolfbeis, O. S. Inert phosphorescent nanospheres as markers for optical assays. *Bioconjugate chemistry FIELD Publication Date: 2001 Nov-Dec* **2001**, *12*, 883-889.
- (113) Schanze, K. S.; Carroll, B. F.; Korotkevitch, S.; Morris, M. J. Concerning the temperature dependence of pressure sensitive paints. *AIAA Journal* **1997**, *35*, 306-310.

- (114) Gomez Martin, J. C.; Spietz, P.; Orphal, J.; Burrows, J. P. Principal and independent components analysis of overlapping spectra in the context of multichannel time-resolved absorption spectroscopy. *Spectrochimica Acta, Part A: Molecular and Biomolecular Spectroscopy* **2004**, *60A*, 2673-2693.
- (115) Hasegawa, T. Chemometrics for spectroscopic analysis. *Analytical and Bioanalytical Chemistry* **2003**, *375*, 18-19.
- (116) He, H.; Xu, G.; Ye, X.; Wang, P. A novel chemical image sensor consisting of integrated microsensor array chips and pattern recognition. *Measurement Science and Technology* **2003**, *14*, 1040-1046.
- (117) Malecha, M.; Bessant, C.; Saini, S. Principal components analysis for the visualization of multidimensional chemical data acquired by scanning Raman microspectroscopy. *Analyst (Cambridge, United Kingdom)* **2002**, *127*, 1261-1266.
- (118) Nelson, M. P.; Aust, J. F.; Dobrowolski, J. A.; Verly, P. G.; Myrick, M. L. Multivariate optical computation for predictive spectroscopy. *Analytical Chemistry* **1998**, *70*, 73-82.
- (119) Sasic, S.; Clark, D. A.; Mitchell, J. C.; Snowden, M. J. A comparison of Raman chemical images produced by univariate and multivariate data processing—a simulation with an example from pharmaceutical practice. *Analyst (Cambridge, United Kingdom)* **2004**, *129*, 1001-1007.
- (120) Turek, A. M.; Krishnamoorthy, G.; Phipps, K.; Saltiel, J. Resolution of benzophenone delayed fluorescence and phosphorescence with compensation for thermal broadening. *Journal of Physical Chemistry A* **2002**, *106*, 6044-6052.
- (121) Turek, A. M.; Krishnamoorthy, G.; Sears, D. F., Jr.; Garcia, I.; Dmitrenko, O.; Saltiel, J. Resolution of three fluorescence components in the spectra of all-trans-1,6-diphenyl-1,3,5-hexatriene under isopolarizability conditions. *Journal of Physical Chemistry A* **2005**, *109*, 293-303.
- (122) Zhang, F.; Brueschweiler, R. Spectral deconvolution of chemical mixtures by covariance NMR. *ChemPhysChem* **2004**, *5*, 794-796.
- (123) Zhou, J.; Varazo, K.; Reddic, J. E.; Myrick, M. L.; Chen, D. A. Decomposition of dimethyl methylphosphonate on TiO<sub>2</sub>(1 1 0): principal component analysis applied to X-ray photoelectron spectroscopy. *Analytica Chimica Acta* **2003**, *496*, 289-300.
- (124) Carroll, B. F.; Hubner, J. P.; Schanze, K. S.; Bedlek-Anslow, J. M. Principal component analysis of dual-luminophore pressure / temperature sensitive paints. *Journal of Visualization* **2001**, *40*, 4053-4062.

- (125) Carroll, B. F.; Omar, A.; Hubner, J. P.; Schanze, K. S. Principal component analysis technique for multi-luminophor luminescent sensor coatings. *The 10th International Symposium on Flow Visualization*: Kyoto, Japan, 2002.
- (126) Malinowski, E. R. *Factor Analysis in Chemistry*; 3rd ed.; John Wiley and Sons, Inc.: New York, 2002; 414.

## BIOGRAPHICAL SKETCH

Muhammet Erkan Kose was born on July 24th, 1977, in Erzurum, Turkey. He spent a cheerful childhood with his grandparents, parents, brother and two sisters. Since his childhood, he loved to play soccer. Erkan started his chemistry education at Bilkent University, Ankara in 1995. He specialized in physical chemistry and received his master's degree under the supervision of Dr. Ulrike Salzner after completing undergraduate work. Erkan was accepted to graduate school in the Chemistry Department of the University of Florida in 2001. He started his graduate studies under the guidance of Prof. Kirk S. Schanze. Erkan plans to continue to postdoctoral studies.